PULSED LASER ABLATION OF SILICON: THE INFLUENCE OF BEAM PARAMETERS ON ABLATED CRATER MORPHOLOGY

By Stefano Buratin

A thesis submitted to The University of Birmingham
for the degree of DOCTOR OF PHILOSOPHY

School of Engineering
Department of Mechanical Engineering
University of Birmingham
October 2017

ABSTRACT

Laser micromachining of silicon is one of the principal fields where the capability of the laser to change the material morphology is frequently applied. The photovoltaic and microelectronics industries use it for several purposes, such as material removal, soldering and micro-drilling. Silicon is still the most used semiconductor despite the recent studies on new materials (e.g. graphene) or thin film. Thus, improvements in silicon technologies by laser micromachining are still crucial. Moreover, a better understanding of the limits and capabilities of silicon technologies remains necessary.

In laser micromachining, significant effort is still underway to predict the morphology resulting from pulsed laser material ablation. Although various models reported in the literature describe the laser material interaction, the relationship between the ablated crater morphology and the laser beam parameters remains unclear, with current methods and equations not readily applicable in the engineering environment. The model can be based on a physics or an engineering approach. On the one hand the physics approach which gives accurate solutions and predictions (starting from the molecular bonds, for example) because it considers several laser beam parameters, but the model solving is very time-consuming and cannot be applied to 3D complex structures. On the other hand, the engineering approach does not consider all the parameters included in the physics approach, and it gives some solutions that cannot be generally extended (for different kinds of lasers or materials) or is valid only under certain conditions and boundaries. However, thanks to the low computational resources required, it can be extended to 3D complex geometries.

The aim of this research is to reduce the knowledge gap in the understanding of laser parameters influence on the ablated crater morphology. In particular, starting from a physics approach, this thesis provides functions and relations for the laser beam parameters that play a secondary role or are not considered in the engineering approach, but can be implemented without increasing the computational resources required. This work is based on the investigation of three laser parameters (i.e. laser pulse duration, laser energy beam distribution, and laser polarisation) that can strongly influence the ablated crater morphology, but which have not been totally implemented in the engineering approach. In addition to a systematic study on the effects of laser pulse

duration, from femtosecond to microsecond scale, the influence of two non-standard energy beam distributions were studied in the thermal regime and the laser polarisation effects in the non-linear laser ablation regime were explored. The crater morphology was analysed with several techniques from the optical to the electron microscopy depending on crater and structure size.

The key findings show the following: ***1)*** 3D crater shape can be approximated using two different developed functions starting from two different physics model approaches (i.e. thermal-based and non-thermal based laser ablation mechanisms). The study also reveals the fundamental role of the laser pulse duration on the 3D crater shape generation. Moreover, a secondary but still important role is played by the laser fluence that can emphasise or reduce the effect of the laser pulse duration on the crater shape. ***2)*** Starting from the approach used in the previous point with a Gaussian energy beam distribution, the study is extended to a round flat-top and a square flat-top energy beam distribution, revealing the importance of the energy beam distribution on driving the final crater shape and interacting with debris and re-deposited material. ***3)*** Evaluating the effects of polarisation in the ultrafast ablation regime, where the linear absorption relations are not valid, a relation between crater depth and polarisation is identified. The dependency of the crater depth on the polarisation is attributed to the laser induced periodic surface structures (LIPSS), In fact, different thresholds of LIPSS amount between linear and circular polarisation, explains the difference in crater depth caused by multiple-scattering. Moreover, the LIPSS study indicates a relation between the LIPSS periodicity and the laser polarisation.

To summarise, this research demonstrates the influence of three laser parameters (pulse duration, pulse energy distribution, and polarisation) on the crater shape and defines novel relations and functions suitable for the engineering environment, reducing the knowledge gap between the laser beam parameters and the ablated crater morphology.

ACKNOWLEDGEMENTS

I would like to express my sincere gratitude to my supervisor, Dr. Carol M.C. Kong, for making me part of the Synergetic Training network on Energy Beam Processing (STEEP) project and for her invaluable guidance and supervision throughout this research. The entire experience will be invaluable and rewarding in my future career development.

Also, I would like to thank my second supervisor, Prof. Stefan S. Dimov, for his support over the past three years.

My deep appreciation goes to Prof. Dragos Axinte for his leadership and support throughout the research as network coordinator of the STEEP projects.

I am grateful to the Marie Sklodowska-Curie Actions (EU FP7-ITN Grant no. 316560) for providing me with the opportunity and financial support to stay at the University of Birmingham and pursue my network in Europe.

A special thank goes to two STEEP project partners: Dr. Iban Quintana and Dr. Johann Michler (EMPA) for their support during my secondments at IK4 – TEKNIKER (Eibar, Spain) and EMPA (Thun, Switzerland) respectively.

I would also like to thank my STEEP project colleague, Miss Simina Rebegea, for the encouragement and motivational talk as well as for the knowledgeable discussion on material analysis.

On a more personal note, my deepest gratitude goes to my family: to my father Mario, my mother Annamaria, and my wife Liana for their constant support, encouragement, and love.

CONTENTS

TABLES

FIGURES

List of Abbreviations and Acronyms

AFM	Atomic Force microscope
2D	Two dimensions
2DFFT	Two Discrete Fast Fourier Transform
3D	Three dimensions
CW	Continuous wave
CPPS	Critical point phase separation
EB	Energy beams
DM	Deformable mirror
EDX	Energy-dispersive X-ray spectroscopy
DFT	Discrete Fourier Transform
DOE	Diffractive optical elements
FFT	Fast Fourier transform
HAZ	Heat affected zone
HSFL	High Spatial Frequency LIPSS
MD	Molecular dynamics
LIPSS	Laser induced periodic surface structures
ODE	Ordinary differential equation
OM	Optical microscope
PD	Percentage difference
PDE	Partial differential equation
PSD	Power spectral density
Q-CW	Quasi continuous wave
RSS	Residual sum of squares
SEM	Scanning electron microscope
SPP	Surface Plasmon Polaritons
SLM	Spatial light modulator
STEEP	Synergetic Training network on Energy Beam Processing
TEM	Transmission electron microscope
WLI	White light interferometer

NOMENCLATURE

A	**Complex envelope**
a	Amplitude
c_e	Electron specific heat
c_i	Lattice specific heat
c_p	Specific heat
c_s	Crater spacing
D	Wave period
d	Thermal diffusivity
d_c	Distance between craters
F	Pulse fluence
E_p	Energy per pulse
ε	Electric field
ε'	Material dielectric constant
G	Temporal coherence function
G_c	Electron-phonon coupling factor
g_v	Galvo speed
k	Electromagnetic penetration coefficient
k_w	Wavenumber
I	Intensity
Λ	LIPSS periodicity
λ	Laser wavelength
λ_t	Thermal conductivity
m_s	Marking speed
m_e	Electron mass
n_0	Valence band electron density
ν_c	Collision frequency
n_e	Electron number density

ω	Angular frequency
ρ	Density
p	SEM profile
P	Power
φ	Phase
r	Point defined by x, y and z coordinates
Rr	Repetition rate
S	Source
Θ_d	Divergence
τ	Real time constant
$\boldsymbol{\tau}_{FWHM}$	Pulse duration measure at full width half maximum
t	Time
T	Temperature
T_e	Electron temperature
T_i	Lattice temperature
w	Laser frequency
u	Real wavefunction
U	Imaginary wavefunction
V	General solution of thermal model
υ	Frequency

PUBLICATIONS

1. S. Buratin, K. Bashtova, and M. C. Kong *Thermal effects on 3D crater shape during IR laser ablation of monocrystalline silicon: From femtoseconds to microseconds*, Journal of Applied Physics 122, (2017)
2. S. Buratin , C. Kong *Craters shape dependence on pulse duration in crystalline silicon generated using an IR Gaussian laser beam: from femtosecond to microsecond regime*, Proceeding in Lasers in Manufacturing Conference (2015)
3. S. Buratin, M. C. Kong *Laser polarization influence on the periodicity of Laser Induced Periodic Surface Structure on Silicon.* Under Submission.

1 INTRODUCTION

1.1 Motivations

In recent years, technologies based on laser devices have been widely applied in three main fields: metrology (e.g. microscopy and spectroscopy), manufacturing (e.g. photolithography and 3D additive manufacturing), and telecommunication (e.g. signal generation fibre and in free space) [1]. However, the manufacturing field and its applications such as annealing, welding, cutting, and scribing are still the primary and most common use of lasers in industry.

The laser has been a processing technology used more frequently in the silicon industry because this material is a fundamental element for the microelectronic industry [2]. Although recently some novel and promising materials (e.g. graphene) are arising as potential silicon (Si) competitors, Si still plays a central role in semiconductor applications and remains the best material to date for the semiconductor technologies [3]. Silicon has been the most popular material for producing integrated circuits and solar cells [4], for this reason, silicon continues to be attractive and interesting for research.

The laser has been widely applied in electronic as well as solar cell manufacturing, but to address the more demanding requirements while remaining competitive with other technologies, an in-depth understanding of the laser ablation mechanisms is essential. A fine tuning of the laser parameters is fundamental to better control the phenomena involved and to extend the results achieved in the research area to the industry [5]. Indeed, laser parameters such as fluence, laser pulse duration, laser energy beam

distribution, and polarisation are the most relevant parameters in the laser material ablation process.

Laser pulse duration is the key parameter, and together with fluence, it enables identification of the mechanisms involved in laser material ablation. The mechanisms involved drive the generation of structures on the material surface, and they contribute to the final material morphology. Debris, redeposited molten material, and droplet generation are the most relevant morphology characteristics of ultrafast laser pulse durations compared to longer pulse durations[6]. Controlling the energy laser pulse distribution allows the single pulse crater characteristic produced on the target to be changed. Controlling the single pulse effect on the surface is the initial step for improving the multi-pulse process (e.g. direct laser ablation of metal film on the glass substrate, drilling in a silicon wafer, and scribing of thin-film solar cells) [7]. The effects of laser polarisation on the laser-material absorption are described by Fresnel's laws, but Fresnel's laws can be directly applied only on linear absorption. Indeed, effects of laser polarisation during ultrafast ablation are generated by nonlinear absorption, and they have not been completely described yet. In particular, for ultrafast pulses, polarisation plays a primary role in laser induced periodic surface structure (LIPSS) generation and orientation. LIPSS are periodic structure, with a size close to the laser wavelength, generated by the interaction of the laser beam and a plasmonic wave. Recently, using a q-plate (QP), which is a device that can generate and manipulate light beams carrying orbital angular momentum, non-standard LIPSS novel orientations were obtained [8]. In addition, crystalline orientation effect on conical structure formation by irradiation of a femtosecond laser was highlighted [9].

The laser parameters above cannot be directly associated with parameters such as etching rate or dwell time that are involved in other machining techniques (e.g. milling, welding, drilling). For this reason, despite the fundamental contribution of laser parameters on material processing, it is difficult to introduce them in an engineering approach. In one aspect, the physics approach considers all the laser parameters involved in laser material interaction, but the engineering approach does it only partially, making the physics approach the most accurate. In another consideration, because of the number of parameters applied to the physics approach (e.g. photon-phonon coupling time or atom potential energy), it cannot be directly compared with the engineering approach. Thus, to correlate the laser beam parameters to the ablated crater morphology in a suitable way for the engineering environment, the development of new

relationship and understanding is required. New relations between the laser beam parameters and the ablated crater morphology more suitable for the engineering filed could allow the simultaneous implementation of a common platform which includes additional energy beam other than lasers.

It is in this context that the STEEP (Synergetic Training network on Energy Beam Processing) project takes place. STEEP is a Marie Curie Initial Training Network established to develop researchers in the field of energy beam processing (pulsed laser ablation, abrasive waterjet, and focussed ion beam) [10]. The aim of the project is to study three different types of energy beams (waterjet, laser, and focused ion beam), to model the material removal process, and to build a common platform that can predict a generic 3D footprint generated using one of the EB operations. The project was divided into two main stages: the first includes the modelling, material analysis, and math and computer science support; the second stage involves the model validation and platform integration.

The overall STEEP project required some common approaches between the three different energy beams. This research work provides equations and relations related to laser material ablation, and these are the main objectives of this thesis. The work developed in this thesis is primarily related to the modelling; thus, it takes part in the first stage of the project. In particular, this work provides some relation between three laser parameters (pulse duration, energy beam distribution, and polarisation) and the crater shape generated by a single laser pulse. The outcome provided could be implemented on the common platform during the second stage of the project.

1.2 Aims and objectives

The principal aim of this study is to bridge the gap between the laser beam parameters and ablated crater morphology providing in order to create application in an engineering environment. Starting from the physics approach (that considers a big number of laser beam parameters requiring high computational resources), the effects of laser parameters on the ablated crater morphology were studied in depth. Relations, functions, and methods were introduced to study laser beam parameters not usually considered in the engineering approach. The functions and the relations can be integrated in the final platform to give a fundamental contribution to the STEEP project. To achieve this aim, three laser parameters were studied: pulse duration, energy beam distribution, and polarisation. The specific objectives are as follows:

1) To identify two different equations depending on the different domain pulse duration (one in the thermal regime and another one in the non-thermal regime) capable of approximating the crater shape obtained by single pulse ablation. From the engineering approach point of view, the capability to associate two different functions to two different crater shapes depending on the pulse duration will permit selection of the most suitable function to reproduce the single crater. The capability to associate a single function that describes the crater shape considering the pulse duration, allows consideration of the pulse duration effects on the crater morphology without increasing the computational resources needed. In addition, from the material analysis aspect, the two equations will provide a quantitative method to measure the amount of the thermal effects induced by laser material ablation.
2) To apply the study defined for a Gaussian energy beam shape in point 1) to a non-standard energy beam distribution (e.g. the top flat square or a top round energy beam distribution). It will relate the thermal effects on the final crater shape to the energy beam distribution, enhancing the effects of thermal diffusion when using non-conventional energy beam distribution.
3) To study the effect of polarisation orientation in the ultrafast regime where Fresnel's laws are not valid because of nonlinear absorption. This will give additional information on the crater morphology (such as depth and diameter) when affected by non–classical ablation effects such as laser induced periodic surface structures (LIPSS). In particular, it will highlight the influence of three

polarisations (circular, horizontal, and linear) on the crater depth, LIPSS amount, and LIPSS spacing.

1.3 Thesis structure

The thesis is divided into seven chapters; the structure is described in Figure 1-1. Chapter 1 is the basis of the thesis, defining the motivations, aims, and objectives. Chapters 4, 5, and 6 develop the functions and the relations based on the study of pulse duration, energy beam distribution, and polarisation, respectively. Chapter 7 summarises the main contributions and presents ideas for further work. Chapters 2 and 3 provide the literature review and the materials and methods needed to investigate the concepts, ideas, and information that are discussed in the thesis.

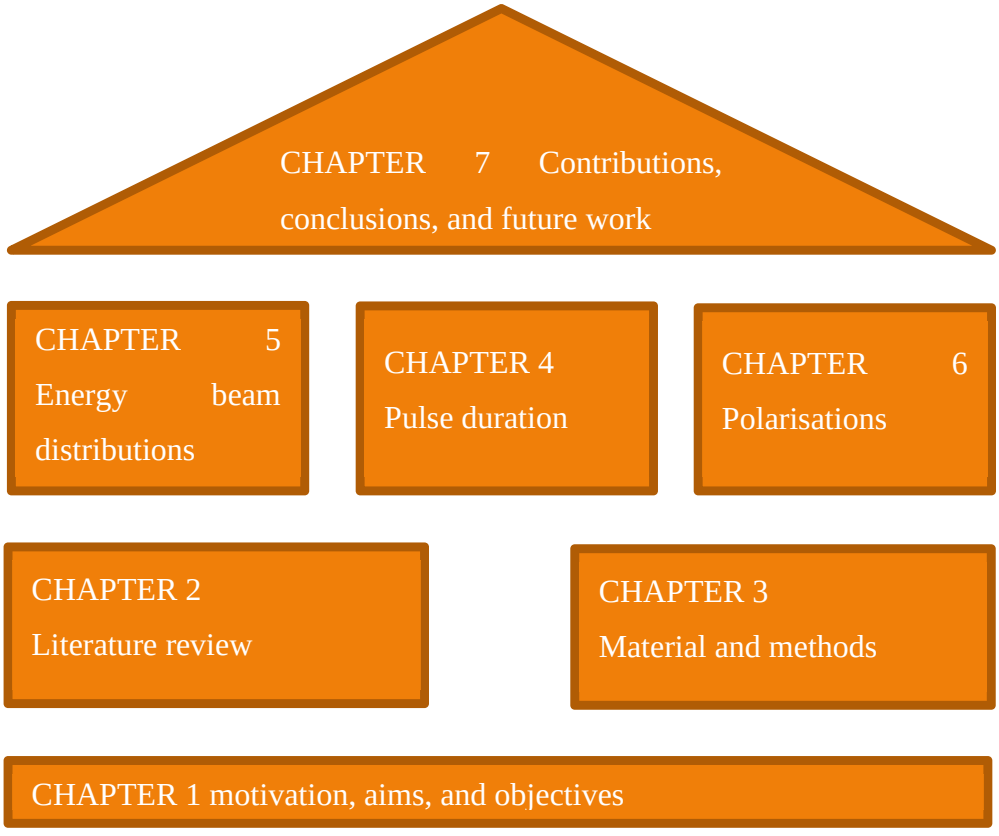

Figure 1-1 Thesis structure

Chapter 1 gives a brief introduction to the laser material ablation problem, highlighting the motivations behind this study and focusing on the material investigated and the laser parameters considered. Moreover, the aims and objectives are summarised in this chapter.

Chapter 2 introduces the most important concepts and mathematics related to lasers and gives the fundamental instruments to the reader for a proper understanding of the following chapters. A literature review on models and experimental results is reported. This chapter highlights the relation between the laser parameters involved in the study (pulse duration, energy shape distribution, and polarisation) and the final crater shape.

Chapter 3 provides a detailed description of the equipment used. It is divided into two main parts: the first part relates on the laser facilities involved in micromachining, and the second part addresses the facilities involved in the material characterisation. The common methodology for data acquisition is reported in the chapter. However, the methodology used for each laser parameter is explained in each chapter that relates to the appropriate parameter (chapters 4, 5, and 6). The description of additional optics added to the laser facilities is included in this chapter.

Chapter 4 investigates the effect of laser pulse duration on the crater shape. First, a method to evaluate the thermal effects of the laser pulse duration on the crater shape is presented. Then a systematic study that covers the pulse duration from the femtosecond to the microsecond regime, is examined. Finally, the effects of laser pulse duration, together with the influence of laser fluence, are discussed based on the method developed and a complementary SEM-based study.

Chapter 5 extends the study presented in chapter 4 for two non-standard laser energy beam distributions. Using 220 ns, the thermal effects discussed in the previous chapter are replicated using a beam with a round flat-top and a square flat-top energy beam distribution. The difference in the thermal effects of using a Gaussian or a non-Gaussian energy beam distribution is exploited.

Chapter 6 is dedicated to the effect of laser polarisation on the crater shape. Three polarisations (horizontal, vertical and circular) are investigated in the ultrafast ablation regime where the linear polarisation and absorption laws are not valid. The polarisation effect is investigated in the situation of multi pulse ablation. To evaluate the LIPSS threshold formation, a method based on the power spectral density (PSD) analysis is developed. A new relation between the LIPSS spacing and the laser polarisation is identified by applying the developed method.

Finally, chapter 7 summarises the findings presented in the previous chapters. It highlights, chapter by chapter and then parameter by parameter, the novel contributions given in this thesis. Moreover, suggestions for further work are proposed based on the

new issues discovered regarding laser pulse duration, energy beam shape, and polarisation.

2 LITERATURE REVIEW

Chapter 2 contains the literature review needed to understand the motivation behind this work.

In the first section, a general overview of the laser material interaction mechanism is reported. Moreover, before the laser parameters under study (i.e. laser pulse duration, energy beam shape and laser polarisation) are introduced, a description of the primary laser properties and the main mathematical relations is provided.

The second section is dedicated to the laser pulse duration: first, the mathematical definition of laser pulse duration is reported. Then, the techniques to change the pulse duration are highlighted, in particular the ones applied in this work. The effects of pulse duration on laser material ablation together with two different modelling approaches are discussed. An overview of the analysis techniques of laser ablation effects on crater morphology closes the pulse duration section.

The third section shows the effects of the energy beam shape on laser material interaction. First, the energy beam distribution is discussed from a mathematical point of view. Then, nonclassical (not Gaussian) energy beam distributions are introduced and described. Finally, the effects of a flat-top, super Gaussian, and square energy beam distribution on laser micromachining are discussed.

The fourth section is related to the laser polarisation. As with the previous sections, it starts from the mathematical background of the section parameter, focusing on linear and circular polarisation. Then, the devices available to change the polarisation are described and the effects on laser ablation are introduced, first in a linear laser

absorption regime and then in a nonlinear laser ablation regime, with an emphasis on the LIPSS phenomenon. Finally, the open research issues covered in this thesis are highlighted.

2.1 Introduction to laser-semiconductor interaction mechanism and laser properties

From the beginning, when ruby lasers were first presented to the world [11], it has been clear that the interaction between the laser light and the material can lead to morphology changes in the material treated by lasers [12]. Consequently, the understanding of the laser material interaction mechanisms and the modelling has gained great importance as a research topic to better control and improve laser material processing.

When light strikes the surface of a material, part of it can be reflected and part can be transmitted into the material. This is due to the interface discontinuity, and is a function of the real part of the refraction index of the interfaces. Using classical optics theory, the amount of light that can be absorbed, transmitted, or reflected can be described by the Fresnel Law [13]. The processes driven by the laser hitting a surface are dependent on the amount of the energy deposited on the surface itself, thus, the absorption. This amount of energy can be modulated by modifying the spatial and temporal distribution of the laser beam [14].

When the energy given to the target by the photon absorption is enough to excite electrons from their equilibrium state, the material state can change based on the energy received. The typical absorption in semiconductors is the single photon absorption; in this kind of absorption, electrons can be excited from the valence band to the conduction band by single promotion [15]. However, by modifying the amount of energy delivered to the target and consequently the number of photons, a multi-photon excitation can be induced. The multi-photon excitation can be generated by the two-photon ionisation, which can induce avalanche ionisation. Consequently, several nonlinear processes can take part in the laser material interaction. Thus, temporal and spatial pulse distributions play fundamental roles in laser material ablation because they can change the density of photons delivered to the semiconductor target, and as a result

they can induce linear or multi-photon absorption. The phenomena involved during the process, because of their dependence on energy, are strongly related to temporal and spatial energy pulse laser distributions. Temporal and spatial energy beam distributions are typically dependent on the laser nature, but they can be modified eventually by introducing an optoelectronic element. Before the laser parameters treated in this thesis are introduced, and their roles in material ablation are discussed, it is fundamental to introduce the laser properties from which the laser parameters follow.

Four laser properties are most relevant: (1) monochromaticity, (2) coherence (spatial and temporal), (3) directionality, and (4) brightness [16]. Knowing the meaning of these properties and their mathematical representation is crucial for an in-depth understanding of the laser parameters and how they drive the laser material processing.

Laser emission light can be ideally represented by a monochromatic wave that is mathematically described by a wavefunction *u(r,t)* with harmonic time dependence:

$$\boldsymbol{u(r,t) = a(r)cos[2\pi\nu t + \varphi(r)]} \qquad \textit{(2.1)}$$

where r is the position in the space *r=(x,y,z)*, *a(r)* is the amplitude, *υ* is the frequency, *t* is the time, and *φ(r)* is the phase. The amplitude and the phase are generally position dependent, but the wavefunction is a harmonic function of time with frequency υ at all positions [17]. The frequency represents the energy of the photon emitted from the laser, and because different photon energy corresponds to a different laser wavelength, the frequency defines the beam "colour". Consequently, if the laser beam can be represented by a wave with a constant frequency, and thus a constant colour, it can be considered monochromatic. The laser frequency is also called wavelength and is defined by *λ*:

$$\boldsymbol{\lambda = \frac{c_0}{n\nu}} \qquad \textit{(2.2)}$$

where c_0 is the speed of light in the media and *n* is the refraction index in the media. Considering that *u(r,t)* describes the real part of a monochromatic wavefunction, it is possible to define the generic imaginary wave function as

$$\boldsymbol{U(r,t) = u(r,t)e^{j\omega t}} \qquad \textit{(2.3)}$$

where *ω* is the angular frequency. Before discussing spatial coherence, temporal coherence will be introduced. The temporal coherence function is defined with the autocorrelation of its complex function:

$$\boldsymbol{G(\tau) = \lim_{P\to\infty} \frac{1}{2D} \int_{-D}^{+D} U^*(t)U(t+\tau)dt} \qquad \textit{(2.4)}$$

where *D* is the wave period and τ an arbitrary time. Similarly, it is possible to define the mutual coherence function [18]:

$$G(r_1, r_2, \tau) = \lim_{P\to\infty} \frac{1}{2D} \int_{-D}^{+D} U^*(r_1, t) U(r_2, t+\tau) dt \qquad (2.5)$$

The coherence and its function describe how close a laser beam is to a perfect sinusoidal wave, or in other words, they quantify how close the real wave is to Eq. 2.1. For example, in the case of a perfectly coherent light source, the beam can be split and even superimposed, and after a very long distance it can creates the same interference pattern that it would create after a short distance. (In reality, the laser beam always has small amplitude and phase fluctuations.) [19]

The directionality of a laser defines how much the light is spread in the propagation axis of the laser beam. It can be quantified using a parameter called divergence, which represents the angle at a long distance. It is defined by [20]

$$\theta_d = W/z \qquad (2.6)$$

where *W* is the beam radius at the distance *z*.

Finally, the last laser property is the brightness, which is defined as the power emitted per unit surface area per unit solid angle. Considering *dS*, the elemental surface area at point *O*, and *dP*, the power emitted by *dS* into *dΩ*, a solid angle around the direction *OO'* can written as [21]

$$dP = B \cos\theta \, dS \, d\Omega \qquad (2.7)$$

where *B* is the brightness. The brightness is generally considered one of the most important properties for laser micromachining because it enables high energy to be achieved in a small confined space. Thus, it is possible obtain all the mechanisms that are required to address the material removal.

2.2 Laser pulse duration

From the temporal point of view, a laser can irradiate on CW (continuous wave) mode or on a pulsed mode to define the way the energy is delivered to the sample. The laser pulse duration is the most relevant laser parameter because it affects several types of phenomena (which will be explained in detail in Section 2.2.3) that occur during the ablation process, and therefore it results in different varieties of surface morphology. Moreover, laser pulse duration has a dominant role compared to other laser parameters

because it is related to the nature of the laser itself. Indeed, it has a strong relation to the laser optical spectrum. Because the minimum pulse duration is limited by the laser spectrum, operations using external optoelectronics elements cannot reduce the pulse duration below a certain threshold.

2.2.1 Mathematical definition of laser pulse duration

The minimum laser pulse duration that a laser can reach is defined by the transform limit, which is essentially equivalent to the condition of a frequency-independent spectral phase. The relation between the spectral *v(υ)* and the temporal description is simply defined from the Fourier transform [17]:

$$\boldsymbol{v(\upsilon) = \int_{-\infty}^{+\infty} u(t) e^{-j2\pi\upsilon t} dt} \qquad \textit{(2.8)}$$

To define the laser pulse duration, the optical intensity must be defined first. The optical intensity defines the optical power per unit area [17]:

$$\boldsymbol{I(r,t) = 2\langle u^2(r,t)\rangle} \qquad \textit{(2.9)}$$

where the operation $\langle\cdot\rangle$ is the averaging over a time interval much longer than the time of an optical cycle but much shorter than the duration of the laser pulse. Moreover, Eq. 2.3 can be rewritten as

$$\boldsymbol{U(r,t) = A(r,t) e^{j\omega_0 t}} \qquad \textit{(2.10)}$$

where *A(r,t)* is the complex envelope of the complex wave function. The complex envelope is characterised by its magnitude *|A(t)|*. Thus, the optical intensity described in Eq. 2.9 [22] can be related to:

$$\boldsymbol{I(r,t) = |U(r,t)|^2 = |A(r,t)|^2} \qquad \textit{(2.11)}$$

In other words, the intensity represents the complex envelope of the complex wave function. The classical representation for a generic pulse (focusing only on the temporal aspect) is the Gaussian form:

$$\boldsymbol{A(t) = A_0 e^{-\frac{t^2}{\tau^2}}} \qquad \textit{(2.12)}$$

where τ is a real time constant. Eq. 2.11 also shows that the intensity is a Gaussian function as well, with peak value $I_0 = |A_0|^2$. To define the pulse duration time, it is possible to use the following quantities:

$$\boldsymbol{\tau_{\frac{1}{e}FW} = \sqrt{2}\tau} \qquad \textit{(2.13)}$$

$$\tau_{FWHM} = \sqrt{2ln2}\tau = 1.18\tau \qquad \textit{(2.14)}$$

where $\tau_{\frac{1}{e}FWHM}$ is the duration measure at 1/e full width, and τ_{FWHM} is the full width half maximum. Using Eq. 2.8, it is easy to identify the FWHM of the spectral density for a Gaussian pulse that is equivalent to $\Delta\upsilon = 0.44/\tau_{FWHM}$ and that defines the transform limited pulse [22].

To complete the laser description in relation to the time and space dependence, the optical intensity can be integrated over the area to define the optical power as follows [17]:

$$\boldsymbol{P(t) = \int_A I(r,t)dA} \qquad \textit{(2.15)}$$

where P(t) is the optical power, and A is an area normal to the propagation direction.

In the same way, we can define the laser fluence, *F* by integrating the intensity over a certain time bigger than the pulse duration:

$$\boldsymbol{F(r) = \int_T I(r,t)dT} \qquad \textit{(2.16)}$$

where T is a time slot greater than the pulse duration. Integrating the intensity over time and area, it is obtained the energy per pulse as follows:

$$\boldsymbol{E_p = \int_T \int_A I(r,t)dTdA} \qquad \textit{(2.17)}$$

2.2.2 Techniques to change the laser pulse duration

As mathematically described in the previous section, the laser pulse duration depends upon the nature of the laser itself. The minimum pulse duration is a function of the laser bandwidth (the reason for using several laser facilities is clarified in section 3.2). However, this fact does not mean that the laser pulse duration cannot be controlled or modulated using optoelectronic devices. This section gives a brief overview of the more common ways to change the pulse duration. It is possible to distinguish two primary methods for changing the laser pulse duration: acting on the electronic signal or modifying the laser optics, depending on the laser gain media.

For example, in semiconductors, the atoms have such strong interatomic interactions that it is not possible to treat them as individual entities. The collection of atoms of periodic potential can be revised by way of energy band. Each one contains densely packed discrete energy levels that can be approximated as a continuum. Figure 2-1 shows the two bands and the energy band gap (E_g) between the valence band and the conduction band. When an electric field is applied, electrons can move from the valence

band (that is full of electrons) to the conduction band that has several unoccupied spots, leaving a hole in the valence band. This process is called electron-hole generation. The process when an electron decays from the conduction band to the valence band to fill an empty hole, as the thermal equilibrium requires, is called electron-hole recombination. During the electron-hole recombination, the same energy can be released by emitting a photon, which generates a radiative recombination [23].

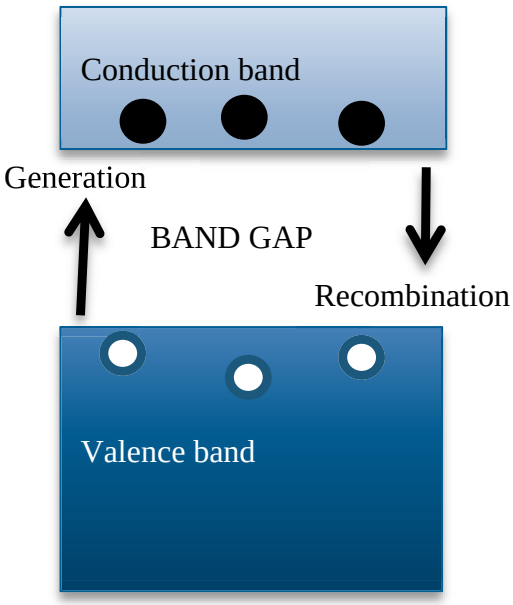

Figure 2-1 Representation of the conduction and the valence band, the generation and the recombination process

The pumping of the electrons from the valence band to the conduction band is typically achieved by injecting a current density [24]. Thus, for a diode laser, it is possible to change the pulse duration by the modulation of the current used to pump. This means that the optical pulse time evolution is strictly correlated with the time evolution of the electronic signal used to pump. However, the optical pulse is not a perfect replica of the electronic signal because some constraints will limit the temporal pulse shape. For instance, the depletion time of the laser diode is a constraint for the optical signal falling time; the time needed to promote enough electrons in the conduction band able to produce the required radiation is a constraint for the optical signal rising time. The technique that uses the driving current to modulate the duration of the laser pulse is called gain switching because the current involved in the pumping is the one that determines the laser gain.

The capability to drive the optical signal acting on the electronic signal used to inject the current on the laser diode can also be extended to the fibre laser that uses a laser

diode as seed generator. Indeed, on the fibre laser, the doped fibre is used to amplify the seed that travels along the fibre, increasing its power, but with minor changes to the temporal shape. Consequently, all the technologies based on diode seed generation and fibre amplification can drive the pulse duration only by acting on the electronics that generate the seed. Typically, these devices can generate pulses with duration from few nanoseconds to the quasi continuous wave (QCW), thus in the millisecond regime, and which can also be used in CW mode.

For the solid-state laser, for instances that are not driven by electrical current, optical techniques can be applied to change the pulse duration. The most common methods are Q-switching, cavity dumping, and mode locking [25].

The Q-switching technique simply turns off the laser output, increasing the resonator losses. It typically employs an absorber positioned on one side of the laser cavity that can be modulated by an electric signal. The absorber is positioned in front of the exit mirror; during the off-time (the time when the laser is not emitting), it is in the active mode, creating a big difference in electron population because of the continuous pumping of the gain medium. When the absorber is deactivated, the emission starts. Because of the larger amount of electron population, the generated pulse is shorter compared to that of a non Q-switching mode.

Cavity dumping is another method to change the pulse duration acting on the resonator cavity. It is similar to the Q-switching mode but instead of creating a population difference, it stores a large number of photons in the cavity. This is possible using an electro-optic device that can change the partial reflecting mirror transmittance. During the off-time, the part of the mirror in the normal resonator that is partially reflecting is kept at 0% transmittance. In this case, the beam cannot exit from the cavity. The mirror transmittance is rapidly changed from 0% to 100%. Because of the sudden movement of photons from the resonator, the high loss arrests the oscillation, creating a high energy pulse.

Mode locking is the technique used to produce ultrafast laser pulses. Compared to the other techniques described previously, it is based on a different operating principle. The other techniques are based on the transient dynamic of a laser medium, while the mode locking method is based on a steady-state process. The short pulse duration is obtained by coupling together the modes of a laser and locking their phases to each other [25]. Locking the phase and coupling the modes is possible to obtain a pulse duration close to the transform limited one described in Eq. 2.8.

2.2.3 Role of pulse duration on phenomena of laser ablation

Section 2.1 featured an overview of the laser material interaction mechanisms. This section presents a discussion of the mechanisms involved in laser material interaction, considering their dependence on laser pulse duration and the laser fluence and intensity.

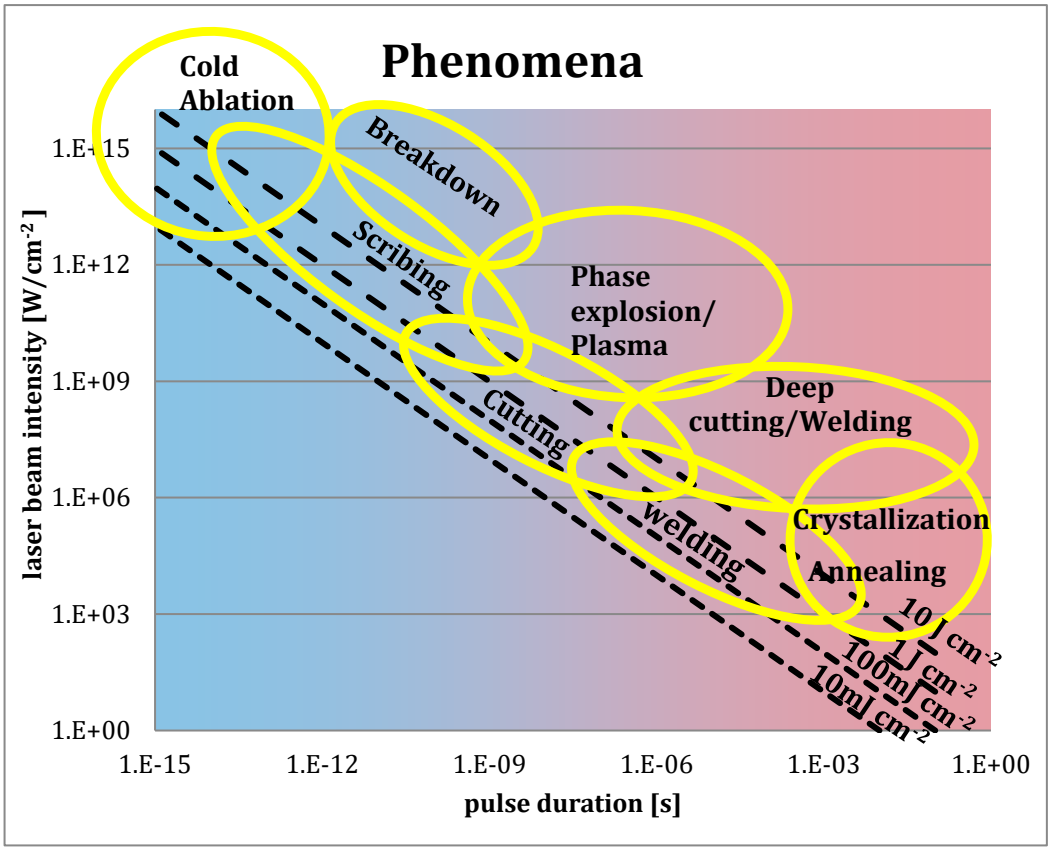

Figure 2-2 Role of pulse duration and energy beam intensity on the phenomena involved in laser material interaction

Figure 2-2 shows the phenomena involved in laser silicon machining and the applications where the laser is used. On the x-axis is reported the pulse duration, going from the ultrafast regime to the continuous regime; on the y axis is reported the laser beam intensity. Both are represented in logarithmic scale because of the wide range covered. The dotted lines are four different levels of fluence around the most common laser fluence available in industrial laser facilities. The yellow circles represent the most common mechanisms which take part in the laser material processing and the most common applications in the laser industry.

In CW mode, the annealing of silicon via laser has been demonstrated [26]. For pulses in Q-CW (in millisecond regime), it is possible to induce crystallisation in silicon [27] above the temperature investigated by conventional annealing. In the annealing case, the morphology is not affected because the process are not sufficiently strong to induce a

change of phase in the material; however, the stress induced can change the mechanical properties [28].

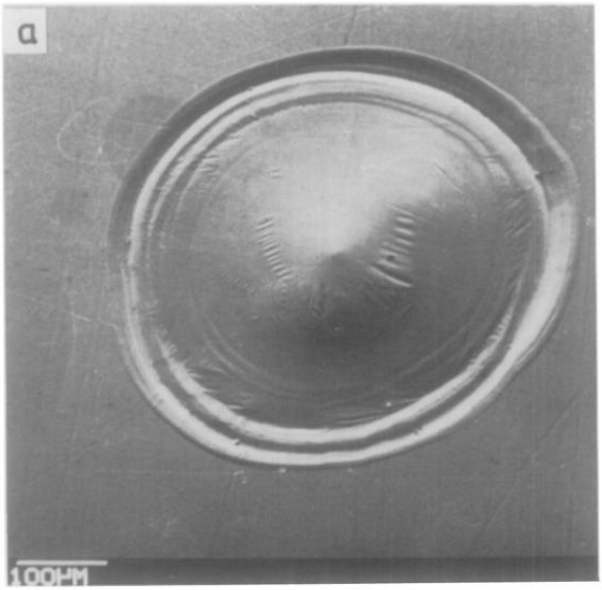

Figure 2-3 Scanning electron micrograph of the laser crater obtained with 50 μs laser pulse on bismuth[32]

In the microsecond regime, the most relevant phenomenon induced is melting, and consequently, the most common applications are those such as glass-to-silicon bonding, which are related to laser soldering [29]. However, actually laser soldering is most commonly employed in the metal and alloy field (e.g. magnesium alloys [30] or titanium alloys [31]) due to their heavy use in the automotive, aerospace, and medical industries. Figure 2-3 shows the classical effect of the single pulse crater generated using the microsecond pulse duration. A visible hump is in the centre of the crater, and a depression is along the edge. This effect can be explained by considering the movement of the solidification of the laser-melted pool. Because of the difference in volume between the solid and the liquid phase, a depressed pool is created during the laser pulse. When the pulse ends, the material starts to re-solidify, and the growth from the side and the cumulative expansion induces a hydrostatic pressure, causing the liquid to rise in the centre and creating the hump [32].

The nanosecond regime is one of the most used regimes in the industry for two main reasons:

- It is possible for nanosecond laser to induce ablation for all non-transparent material using many of the available wavelengths.
- Laser technology developed to date allows easy integration of the laser source with the industrial machine using a fibre delivering system to reach the sample.

Although nanosecond is the most common pulse duration used in laser processing, it is not the simplest regime of pulse duration to model and describe. Indeed, several mechanisms contribute to the processes involved in the laser material processing at this pulse duration regime. For instance, the superheated layer created by the laser pulse causes the pressure to increase quickly, and consequently, an explosive boiling occurs within this layer, leading to particulate ejection from the sample. This action is commonly identified as phase explosion [33][34]. Figure 2-4 shows the effect of phase explosion on a silicon sample. Figure 2-4a shows the cross-section of a trench generated with a 50 ns pulse width. The high amount of debris around the trench is quite visible [35]. Figure 2-4b shows a detail on the crater: the particles ejected during the explosive boiling phase can affect the crater surface. The surface is not smooth but has visible cracks, cavities left empty from the ejected material, and trapped bubbles beneath the re-solidified material [34].

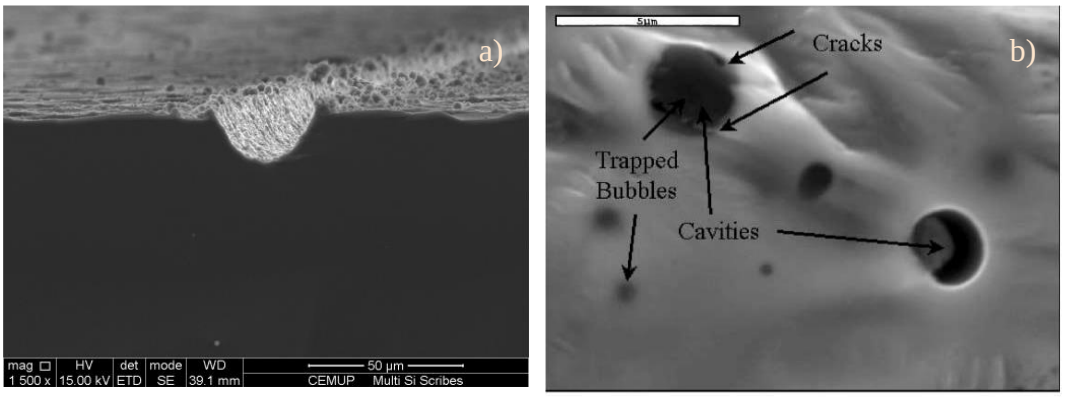

Figure 2-4 Effects of nanosecond laser ablation of silicon: a) cross-section of a trench made at 50 ns that highlights the amount of particle ejected [35]; b) a detail of crater surface with the cavities created from the explosive boiling [34].

Mechanisms involved in nanosecond laser ablation are more complex compared to those of longer pulses because of the high intensity reached by the laser beam at this pulse duration, which allows energetic electrons to escape from the target. Consequently, the electric field created by the charge separation between the escaping electrons and parent ions can pull ions out of the target [36]. The ion gas formed under these circumstances leads to a phenomenon known as plasma absorption: the laser beam is partially absorbed by the plasma created by the pulse itself before reaching the target [37], reducing the laser effects on the sample.

The picosecond is generally accepted as the pulse duration cut off between thermal and non-thermal mechanisms because the photon-phonon relaxation time is in the picosecond region. When an electron absorbs the energy from one or more photons, it is excited to a higher energy state, and the time it takes for this energy to be transferred to the lattice is a few picoseconds [38], [39]. The ionisation involves several processes such as multiphoton absorption and inverse bremsstrahlung or cascade collisional ionisation, in competition with deionisation by diffusion, recombination, and radiative energy losses [40]. All together they drive an electrical breakdown in silicon [41], which means that the material becomes electrically conductive and thus similar to metals, at least in a region very close to the surface. The processes involved on this regime are not thermal based, thus the thermal laser ablation effects are strongly reduced by using pulses of shorter duration than the photon-phonon relaxation time, compared to using pulses longer than the photon-phonon coupling time [6]. For this reason, it is common to refer to the ablation obtained with a fs pulse duration and to all the pulses that have a time duration shorter than the photon-phonon relaxation time, as ultrafast pulse duration, or as "cold ablation" [42]. In the past ten years, the ultrafast laser ablation process has moved rapidly from the research lab to the industry for two primary reasons:

- Ti:Sapphire based technology has been replaced with other technology that is more reliable, such as solid state or fibre doped; both are Ytterbium based, capable of generating pulses around a few hundred fs.
- The ability to interact with a very thin layer of material has opened to the laser several new applications that benefit from the high laser repetition rate to obtain a high process speed.

For the above reasons, ultrafast lasers have been applied in fields that require a large, shallow surface patterning, as in thin film technology [43] or micromachining of small features, such as the nanostructuring of silicon [44].

Figure 2-5a and Figure 2-5b show the crater generated on copper by a single laser pulse, with 40 [45] and 120 fs [46], respectively. On both craters, no debris is present around the crater, and the rim around the edge is comparatively smaller.

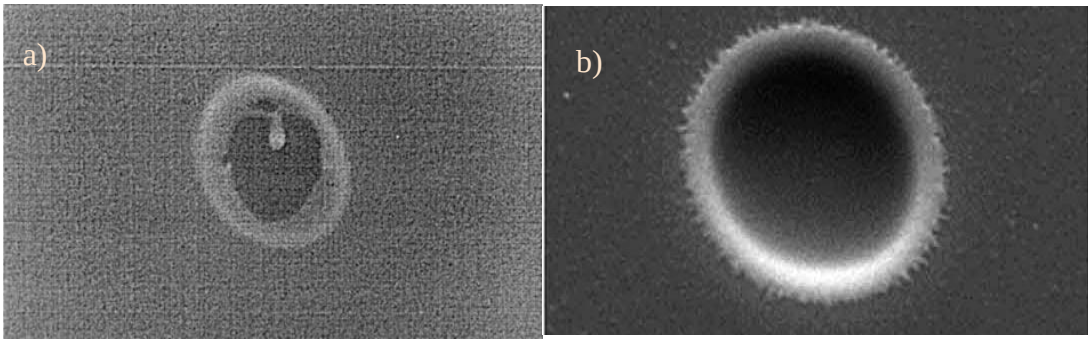

Figure 2-5 On the left is a SEM image of a crater obtained at 40 ps [45]. On the right is a SEM image of a crater obtained with a 120 fs pulse width[46]

The comparison between the two regimes, thermal and non-thermal, has been covered by several groups focusing on different aspects. However, most of the work has focused on the fact that using an ultrafast laser source, the material characteristics are not altered as much as they are using longer laser pulses because of the absence of the thermal mechanisms with the former. Stern et al. [47], found that ultra-short-pulsed lasers at visible and near-infrared wavelengths might have advantages over conventional ophthalmic neodymium-YAG lasers for some intraocular applications, and they are a possible alternative to excimer lasers for corneal surgery. A comparison between femto, pico, and nanosecond pulses shown by Chichkov et al. [6], showed that the ultrafast pulses achieve a sharper and better defined pattern than the nanosecond pulses. Zeng et al. [48], carried out a comparative study between the plasma induced with femtosecond and nanosecond pulses, respectively, demonstrated that the ablation efficiency was enhanced for femtosecond laser pulses. This is because the plasma plume for the ultrafast femtosecond pulse typically forms after the ending of the pulse; in contrast, for the nanosecond pulse, the plasma plume acts during the pulse and absorbs part of the energy of the pulse, reducing the energy delivered to the target. While the impact of the pulse duration seems to be relevant on the crater morphology, other material characteristics such as stress, composition, and crystallinity do not seem to be affected from the pulse duration. The results obtained from Zorba et al. [49], indicated that the morphology, size, and aspect ratio of the fabricated microcones are strongly dependent on pulse duration, while the composition and crystallinity are not affected. Indeed, for these characteristics, similar trends are present for each time duration. Amer et al. [50],compared the stresses and structural changes induced in silicon wafers by femtosecond with the ones by nanosecond pulses ; the femtosecond laser was found to

induce significant stress and amorphisation in single crystal silicon despite the low thermal impact and the reduced heat affected zone (HAZ).

2.2.4 Effect of pulse duration on material ablation laser modelling approaches

As shown in the previous section, many phenomena are involved in the process of laser material interaction. Because of the high number of phenomena, several approaches have been applied to model the mechanisms that drive the material ablation.

Many of the models for laser material interaction only consider the thermal processes [51]. They use a microscopic scale to describe the process, based on the heating of the solid, followed by melting and evaporation. Based on the evaporation temperature, these models identify the amount of material that can be ablated by the double change of phase, from solid to liquid and finally to vapour. As a typical classical thermal problem, it is based on the Fourier equation [52]:

$$\boldsymbol{\nabla \cdot \lambda_T \nabla T + S = \rho C_p \frac{\partial T}{\partial t}} \qquad \textbf{(2.18)}$$

where λ_T is the thermal conductivity, S is the source (the laser energy beam), ρ is the density, C_p is the specific heat, and T is the temperature.

Several conditions can be applied to this classical approach, and additional elements can be introduced in the models to bring them closer to the real conditions that the models intend to replicate. For instance, a 1D thermal model of the gas dynamic flow of the vapour was added to Eq. *2.18* to include the variation of the threshold laser fluence for target evaporation with respect to target surface reflectivity [53]. To simulate the silicon explosive boiling, the critical radius for self-growing bubbles was estimated, considering the surface tension, pressure of the superheated liquid, and saturation pressure [54]. Buratin et al. [55], evaluated the stress and strain caused by the thermal expansion of the laser irradiation on thin film ; the goal was to identify the detaching threshold of the thin film from the bulk. The mechanism that is commonly added to the classical thermal model is the plasma plume formation because, as explained in section 2.2.2, it can absorb part of the laser beam and reduce the ablation effects. Balazs et al. [56] evaluated the plasma ignition threshold accurately, where the reflectivity dependence on temperature was considered. The primary cause of ion generation was attributed to the thermionic emission from the heated surface, generally described by the Langmuir-Saha equation [57]. To better investigate the laser-solid-plasma interaction, Amoruso reports a comparison between low laser intensity and high laser intensity [58].

Two different models were developed for nanosecond pulse duration to incorporate the plasma contribution: one for high and another for low intensities. For low intensities, the vapour produced is treated like an optically thin medium, and the laser light passes nearly unattenuated. For high intensities, the vapour is ionised sufficiently to become absorbing, at least for part of the incident laser beam, and leads to breakdown and plasma formation.

The model approach used for ultrashort pulses (ps and fs regimes), which corresponds to non-thermal ablation, is known as the two-temperature model [59]. Because of the short time pulse duration, the transfer of the laser energy from the electrons to the lattice may not be considered simultaneous. Thus, the electrons and the lattice may not be in the thermal equilibrium, and the models need to consider the following two thermal equations, for the electrons and the lattice, respectively [60]:

$$\frac{\partial}{\partial t}(C_e T_e) = \nabla(k_e \nabla T_e) - G_c(T_e - T_i) + S \qquad (2.19)$$

$$C_i \frac{\partial T_i}{\partial t} = G_c(T_e - T_i) \qquad (2.20)$$

where T_e, T_i, C_e, and C_i are the temperature and the heat capacity of electrons and lattice, respectively, $K_{e\ is}$ the electron thermal conductivity, and G_C represents the electron-phonon coupling factor. The two-temperature model has been primarily used for metals because of the high presence of free electrons which can induce ionisation. However, during interaction of ultra-short laser pulses with semiconductors (and dielectrics), free electrons may be generated by photo-ionisation and avalanche ionisation [61]. Thus, considering the two photon ionisation and the absorption via inverse Bremstralung, the two-temperature model can be applied to a wide range of materials [62]. Differently from the thermal model, the ablation of the material was not identified by the vaporisation temperature but was defined by the critical point phase separation (CPPS) [63]. The high temperature increases above the critical temperature, directly from the solid phase, together with the expansion leading to the thermodynamically unstable region, causing the material decomposition. As for the thermal regime, as well as the non-thermal region, additional phenomena can be included to better describe the process. For example, the hydrodynamic approach can be added to the two-temperature model: the influence of the early heat transfer by

electronic thermal conduction on hydrodynamic material expansion and mechanical behaviour was investigated [64].

To solve the problem related to ultrafast ablation prediction, the approach of molecular dynamics (MD) was also employed. The molecular dynamics model, in contrast with the models described above, do not treat the target as a bulk but as a molecular group. This means that the energy delivered by the laser to the target is compared and related to the interactions between atoms and their potential energies, and consequently to the energies of the atomic forces and bonds. Imamova et al. [65], starting with the model using MD approach used to investigate the properties of a solid in different phases, developed a model of the ablation of metal to evaluate the ejection dynamics, lattice temperature, pressure distribution and ablation rate. Evaluating the ablation evolution, examining the pressure and temperature distribution inside the material revealed the spallation: a thermo-mechanical mechanism [66] occurring for fluence values too low to generate the phase explosion. Similarly, the phase explosion was not observed for picosecond pulses [67]; the only relevant ablation mechanism observed was the fragmentation of hot metallic material.

In contrast to the models introduced above, another group of models have been defined as analytical or semi-analytical. In these models, the physical relations describing the mechanisms behind the laser ablation are reduced to the minimum or are completely absent. Despite the lower prediction accuracy of these models, they are an essential resource in the field that requires very low computation time and can predict a high volume/area. A semi-analytical model was developed by Arnold et al. [68] where the nonlinear heat equations were reduced to ordinary differential equations, and a method of non-stationary averaging to study the influence of several factors onto ablation curves was applied. A complete numerical model was presented by Lunney et al. [69] to estimate the laser ablation effect on metals in the vicinity of the ablation threshold. The model showed that by increasing the energy, the vapour plume absorption of the energy beam was much stronger than the amount indicated by the inverse bremsstrahlung relation.

2.2.5 Analysis techniques of laser ablation effects on crater morphology

In section 2.2.4, several models were described to predict the laser material interaction; two main approaches were used: thermal and non-thermal. To verify the morphology predicted by the models, the resulting craters or pattern can be analysed in two ways.

The first method is microscopic: this analysis examines features around the micrometre size (such as the crater diameter and the depth). It is usually conducted via 3D microscopy using a contact or contactless instrument. It provides a quantitative analysis because the data collected is given by 3D data matrix coordinates. Wang et al. [70] used a quantitative measurement to evaluate the laser silicon ablation in three different temporal regimes: millisecond, nanosecond and picosecond. In particular, the crater diameter was measured to evaluate the ablation threshold. Again, a comparison between the silicon ablation in air and in water was conducted; in this case, optical microscopy (OM) was used to analyse the surface morphology. Moreover, an analysis with an optical profilometre was performed to obtain a 3D map of the craters [71].

The second method is based on nano scale features (such as debris, redeposited material, or splashes) and is typically done using electron microscopy. It cannot provide a quantitative 3D analysis, but it is based on a 2D quantitative analysis that is supported by a qualitative analysis provided by complementary devices such as EDX (energy-dispersive X-ray spectroscopy) or Raman spectrometry. Ionin et al [72] conducted a SEM analysis to evaluate the thermal melting and ablation by femtosecond laser ablation, highlighting a smooth amorphisation and nano-roughness ablation region separated by nano features on the edge of the crater. For instance, a study on the structural details and the level of damage to a silicon sample irradiated by a single femtosecond pulse was carried out using transmission and scanning electron microscopy [73]. Again another work also in the silicon ablation [74] compared the ablation in air and water: the ablation rates and the cross-section profiles were achieved by transmission electron microscope (TEM).

Atomic force microscopy (AFM) is a technique that allows 3D mapping of the crater with nanometre accuracy; it is usually combined with electron microscopy analysis. Ionin et al. used [72] a complementary technique to the SEM analysis to investigate the crater depth and shape. However, electron microscopy was not the only complementary method. The AFM was used in combination with SAEM and Raman spectroscopy to study the modification of single crystalline silicon after the femtosecond laser irradiation [75]. The three techniques (AFM, SEM and Raman), in combination, gave fundamental information about the formation of the thin amorphous region as well as recrystallised zones and topological surface structure formation as rims and protrusions.

Each of the techniques requires different data acquisition time. Considering a crater with a hypothetical diameter of 30 μm, it will be discussed the data acquisition time for

the devices above. The optical microscopes are the fastest, and the data can be acquired in a few seconds. It is possible to estimate approximately 30 s per crater as the acquisition time for an optical system or similar contactless analysis systems. A slightly longer time can be necessary to make an analysis with a contact profilometre, but it can still be considered in the same group. For the devices based on electron microscopy the data acquisition time is longer because they operate in vacuum, so depending on the pump and the vacuum chamber size, a longer time may be required to reach the desired pressure. Moreover, the electron irradiation and electron detection process can be a longer process, adding more time to the total analysis time. The time required for crater data acquisition can be estimated at approximately 3 minutes. The final step is the AFM analysis: the data acquisition time can be estimated at approximately 30 minutes. Even though the AFM gives the 3D mapping with the best accuracy, it is a time-consuming analysis method that cannot be used on a parametric study such as the one carried out in this thesis.

2.3 Laser energy beam distribution

The second laser beam parameter discussed in this thesis is the laser energy beam distribution. A beam coming out from a laser resonator typically has a Gaussian energy distribution. This is true for most laser beams, but there are some exceptions: for example, the laser diode that presents a high astigmatic beam due to the resonator geometry. However, the energy beam distribution can be changed by introducing additional optical elements, and it is possible to obtain several types of energy beam distributions. The most common types are the flat-top and the super Gaussian. These energy distributions can be very useful from an industrial point of view because the energy is almost constantly distributed over a certain area, which enables them to achieve a better accuracy on certain types of machining. However, the technology required to change the energy beam shape is not yet ready for full industrial use because it has limits on features such as short Rayleigh length or high accuracy that is required for alignment.

2.3.1 Mathematical definition of energy beam distribution

The energy beam distribution is a more generic way to refer to the optical intensity distribution on the x-y plane z=0. As seen in Section 2.2.1 the optical power varies in time and space: this is highlighted by Eq. 2.9. and the pulse is temporally described by a

Gaussian function (Eq. 2.12). Indeed, it is possible to mathematically develop the part of the complex amplitude related to the spatial distribution (Eq. 2.11). Furthermore, as accomplished for the temporal shape, it is possible to identify a relation for the spatial shape.

The electromagnetic wave is considered a paraxial wave travelling along the z axis. The relation of the complex amplitude envelope along the z axis can be described by

$$\boldsymbol{U(r) = A(r)e^{-jk_w z}} \qquad \textbf{(2.21)}$$

where k_w is the wavenumber $k_w=2\pi/\lambda$.

To ensure that the *U(r)* satisfies the Helmholtz equation, *A(r)* has to satisfy the paraxial Helmholtz equation:

$$\boldsymbol{\nabla_T^2 - 2jk_w \frac{\partial A}{\partial z} = 0} \qquad \textbf{(2.22)}$$

where $\nabla_T^2 = \frac{\partial^2}{\partial x^2} + \frac{\partial^2}{\partial y^2}$ is the transverse Laplacian operator. A simple solution is

$$\boldsymbol{A(r) = \frac{A_1}{z} e^{-jk\frac{x^2+y^2}{2z}}} \qquad \textbf{(2.23)}$$

The corresponding Gaussian solution (by a simple transformation) is

$$\boldsymbol{A(r) = \frac{A_1}{q(z)} e^{-jk\frac{x^2+y^2}{2q(z)}}} \qquad \textbf{(2.24)}$$

where $q(z)=z+jz_0$ and z_0 is a parameter called Rayleigh range. It proceeds that the complex amplitude of the Gaussian beam is

$$\boldsymbol{U(r) = \frac{A_1}{jz_0}\frac{W_0}{W(z)} e^{-\frac{x^2+y^2}{W^2(z)} - jkz - jk\frac{x^2+y^2}{2R(z)} + j\zeta(z)}} \qquad \textbf{(2.25)}$$

where

$$W(z) = W_0\sqrt{1+\left(\frac{z}{z_0}\right)^2}$$

$$R(z) = z\left[1+\left(\frac{z_0}{z}\right)^2\right]$$

$$\zeta(z) = tan^{-1}\frac{z}{z_0}$$

$$W_0 = \sqrt{\frac{\lambda z_0}{z}}$$

As stated at the beginning of this section, the optical intensity is the second power of the modulus of the complex amplitude; the modulus of the Gaussian beam is described by the following equation [76]:

$$\boldsymbol{I(x,y,z) = I_0\left[\frac{W_0}{W(z)}\right]^2 e^{\left[-2\frac{x^2+y^2}{W^2(z)}\right]}} \qquad \textbf{(2.26)}$$

where $I_0=|A_0|^2$. Then, the optical intensity for z=0 is

$$\boldsymbol{E_d = I_0 e^{\left[-2\frac{x^2+y^2}{W_0}\right]}} \qquad \textbf{(2.27)}$$

Eq. 2.27 is the energy distribution of a Gaussian beam in the plane z=0.

2.3.2 Generation of non-Gaussian energy beam distributions

As stated in Section 2.3.1, the energy beam distribution coming from a paraxial wave typically can be described as a Gaussian distribution. The method to move from a Gaussian distribution to a non-Gaussian distribution generally can be divided in two groups:

- Passive optics: In this case, an optic system, usually a diffractive optics element (DOE), can produce a single energy beam distribution
- Active optics: This is a system that produces more than one energy beam distribution and with an additional feedback system (e.g. wavefront sensor) can correct some aberration of the beam, such as spherical and chromatic aberration, astigmatism, or coma.

The passive optics in this thesis are based on DOE. Typically, the DOEs are applied to generate a diffraction pattern because of the requirement to generate a multi-spot pattern to increase the number of spots and, consequently, the process speed. However, the generation of a diffraction figure in the far field can be used to obtain a non-Gaussian energy distribution in the near field. A method is given for how a simple device can be used to generate a flat-top intensity starting from a Gaussian energy beam distribution [77]. A classical simplified example describing how a DOE works is shown in Figure 2-6. The DOE element is positioned in the collimated beam, which generates a certain diffraction figure that is then focused. At a certain distance from the focusing element, the non-standard energy beam distribution is achieved. It is interesting to note that the position where the desired energy beam distribution is obtained does not correspond with the focal length of the focusing lens. As a matter of fact, the working distance for the non-Gaussian shape is usually shorter than lens focal length.

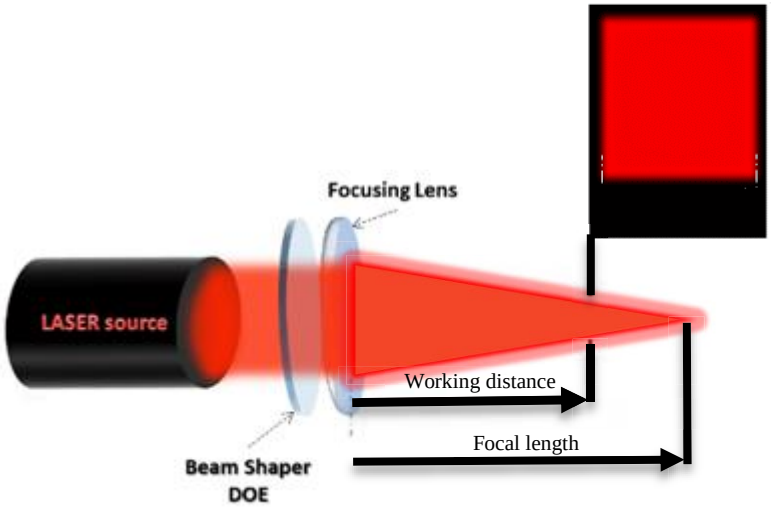

Figure 2-6 Description of the setup to generate a square flat-top beam [78]

In this work, only passive optics will be used, but to give complete overview, a short description of active optics is reported here. The active optics can be divided into two types: spatial light modulators (SLM) that operate by transmitting the laser beam and deformable mirrors (DM) that operate by reflecting the laser beam. Although the two technologies are different, they are based on the same concept. First, the Gaussian beam interacts with a device capable of modifying the phase of the optical field. Then, by phase modification on the far field, it is possible to modify the intensity distribution on the focal plane. Figure 2-7 shows an example using SLM: the SLM modifies the laser beam phase on the x-y plane and, by focusing the collimated beam, a new energy shape is obtained in the x'-y' plane. The pixels on the new plane are related to the old ones by the Fourier transform **[79]**. The DM works on the same principle, with the difference that the beam is reflected in place and then transmitted by the active device. Both DM and SLM need to have feedback after the device to modify the phase in the proper way. For this reason, the beam between the device and the focusing optics is checked by a wavefront sensor. Modifying the SLM (or the DM), the desired energy beam shape can be achieved at the working distance. If from one side the active systems offer the opportunity to obtain several energy beam shapes in the focal plane, on the other side a feedback system limits the integration of an active system in an industrial micromachining laser system. Indeed it is used in a very limited range of applications that are not in the micromachining filed, such as on manipulation of biological systems by optical tweezers [80], laser shaping for inertial confinement fusion experiments [81], or atomic traps [82] where a frequent modulation of the spot is required and it cannot be achieved by passive optics.

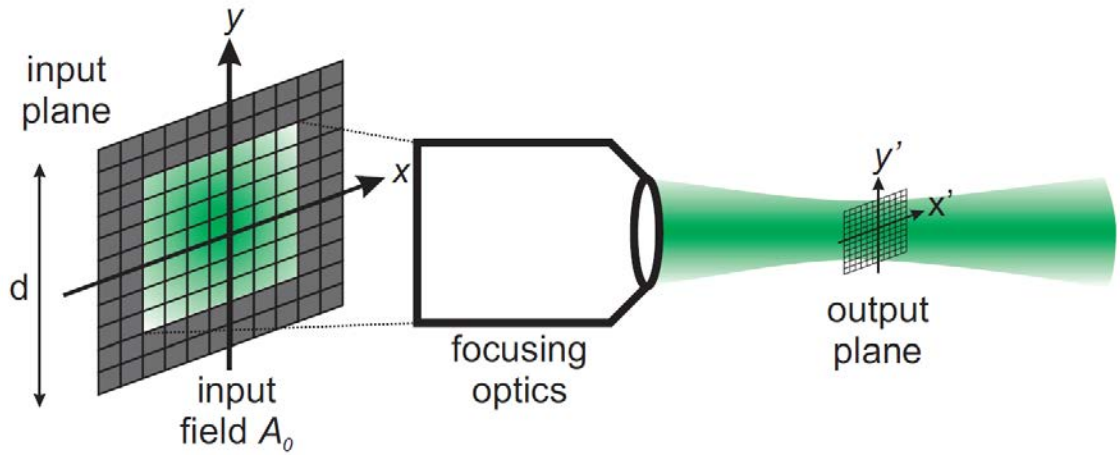

Figure 2-7 Schematic geometry of an IFTA. The field is discretised on x and y and the SLM is modified to obtain the desired Fourier transform in x',y' [79]

2.3.3 Non-Gaussian energy beam distribution on laser micromachining

The changing of the energy beam shape in the focal plane should correspond to a change in the crater shape. However, as described previously, the beam shaping is obtained by a diffraction system or a change in the phase, and the uniformity of a flat-top is strongly related to the quality of these transformations. Sanner et al. [83] discussed the energy beam distribution and the corresponding crater shape for several beam shapes. The Gaussian energy beam shape of a femtosecond laser source was modified by an active and programmable focal-spot shaping method capable of modulating the spatial beam phase and then changing the energy beam distribution in the focal plane. Four different energy beam shapes were applied to a stainless-steel sample (Figure 2-8): a circular top hat, a doughnut, a square top hat, and a triangle top hat. Good agreement was reached between the shape of the machined structures and the beam shape. Neither an undesirable amount of the debris nor molten material around the crater was visible. The low quality of the edges of the square hat top led to an ablated square crater without straight edge, and the intensity defect near the left superior edge of the triangle shape (Figure 2-8a) led to a small mark on the corresponding region on the steel sample. Moreover, looking closer at the triangle and the square shape on the sample, it can be seen that the bottom surface achieved a roughness approximately corresponding to the energy beam distribution.

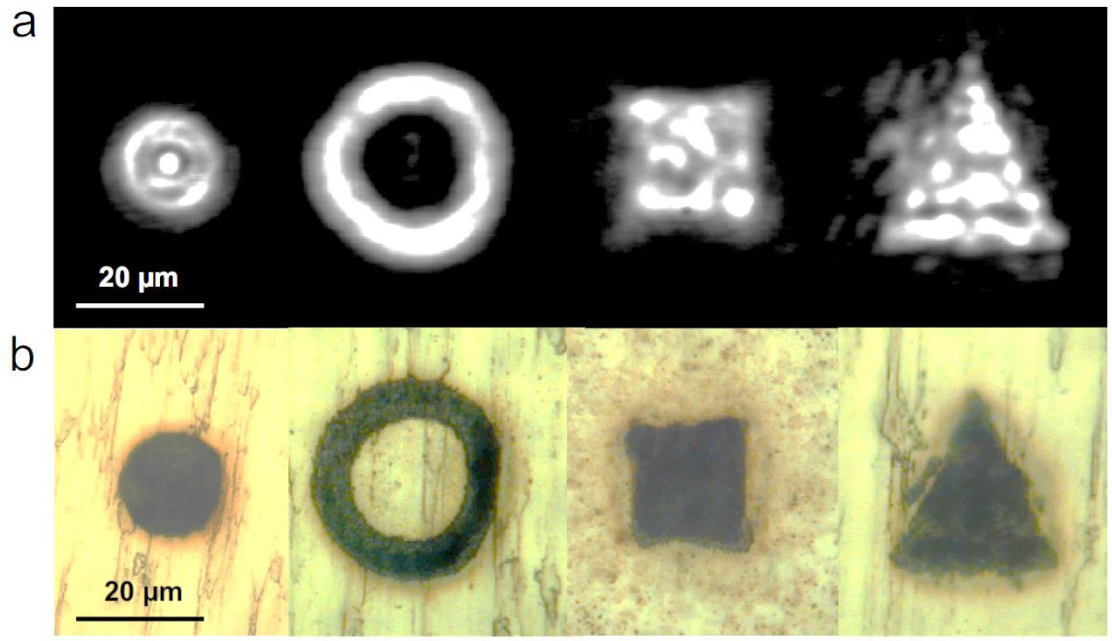

Figure 2-8 Energy beam shape distributions in the focal plane (a) and resulting affected material after 50000 pulses (b) [83].

As mentioned previously above, the active beam shapers are used infrequently in the machining and industrial fields because they need a feedback system. Indeed, most studies on laser micromachining with non-standard energy beam distribution report the integration of a passive device in the laser facility. Kim and Cho [84] used a quasi-flat-top beam instead of a Gaussian beam to investigate the indium tin oxide (ITO) ablation. By using the flat-top shape, it was possible to pattern the ITO surface, using a single process without any patterning mask to control the forming depth, and achieve well-defined morphology. As shown in Figure 2-9, the shape obtained was almost a square shape, but because of the real energy distribution and the difficulties to obtain a flat top, the bottom of the crater was not very flat. As seen, in Figure 2-9d and Figure 2-9e, the colour on the bottom of the crater was not uniformly distributed, meaning that the bottom of the crater was not flat as expected. Despite this result, the quasi-flat-top energy beam shaper improved the performance of morphology and allowed ablation depth control.

A similar approach was used where a beam with a Gaussian energy beam distribution was compared with a flat-top beam on the local contact opening in SiN_x layers that passivate the front side of solar cells [85]. In addition to the classical morphological analysis conducted by SEM and TEM, the quality of the laser machining was evaluated based on the dark J-V characteristic. The results show that the dark current of the

alkaline textured diodes treated with flat-top energy beam distribution is higher than the one treated with the classic Gaussian energy distribution. Thus, despite the more homogeneous energy distribution of the former, the flat-top does not improve the general device characteristics, and the Gaussian beam profiles seem to produce results as suitable as those of the flat-top profiles.

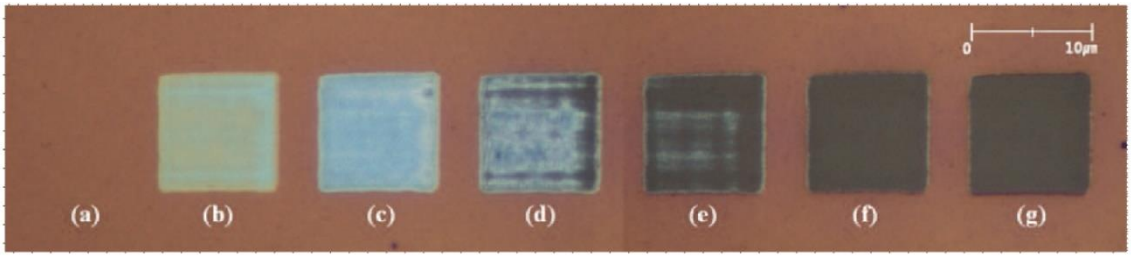

Figure 2-9 Optical microscope picture of ITO pattern with different number of pulses: (a) 0, (b) 1, (c) 2, (d) 3, (e) 4, (f) 5, (g) 6 [85].

2.4 Laser polarisation

The third, but no less important, laser parameter, which was studied in this thesis, is laser polarisation. As shown in section 2.1, the laser emission can be described by an electromagnetic wave function. The wave is approximately transverse electromagnetic; the polarisation state identifies by convention how the electric field oscillates in a certain direction with respect to the propagation direction of the laser beam. The polarisation can assume several states. The most common states are linear (parallel and perpendicular) and circular. However recently, with the introduction of the optical vortex via q-plates, other types of polarisation states (e.g. azimuthal and radial state) have aroused interest, but they are still in an early stage in the laser manufacturing field.

2.4.1 Mathematical definition of laser polarisation: linear and circular polarisation state

Considering the electromagnetic wave described in section 2.1 using Eq. 2.1 and starting from that equation, the electric field can be generally described by $\boldsymbol{\varepsilon(z,t)}$ in the x-y plane as propagating in the z direction:

$$\boldsymbol{\varepsilon(z,t) = Re\left(Ae^{j\omega(t-\frac{z}{c})}\right)} \qquad (2.28)$$

where $\boldsymbol{A}$ is the complex envelope defined as $A = A_x\hat{\boldsymbol{x}} + A_y\hat{\boldsymbol{y}}$. Using the two components to describe the wave vector in the x-y plane, it is possible to describe the polarisation state. Indeed, it is possible to express A_x and A_y in terms of their magnitudes (a_x and a_y) and phases (φ_x and φ_y) as follows:

$$A_x = a_x e^{j\varphi_x}$$
$$A_y = a_y e^{j\varphi_y} \qquad (2.29)$$

Then, substituting Eq. (2.29 in Eq. *2.28*, it is possible to express the electric field in the x and y components [86]:

$$\varepsilon_x = a_x cos\left((\omega\left(t - \frac{z}{c}\right) + \varphi_x\right)$$
$$\varepsilon_y = a_y cos\left((\omega\left(t - \frac{z}{c}\right) + \varphi_y\right) \qquad (2.30)$$

The polarisation can be expressed by the two equations above on the x-y plane. Based on these two equations, it is possible to describe the polarisation states that will be used in the next sections.

2.4.1.1 Linear and circular polarisation

When one of the components (a_y or a_x) vanishes, the beam is considered to be linear polarised (parallel "p" or perpendicular "s"). Figure 2-10a shows an example of linear polarisation (parallel). The only component present is the one on the x axis; meanwhile, the component on the y axis is not present. The polarisation is still considered linear when the difference in phase of the two components is 0 or π. In this case, the resulting vector is not aligned with the x or y axis, but is based on the amplitude of the two components. The resulting trajectory of the end point of the electric-field vector is tilted at a certain amount between 0° and 180°.

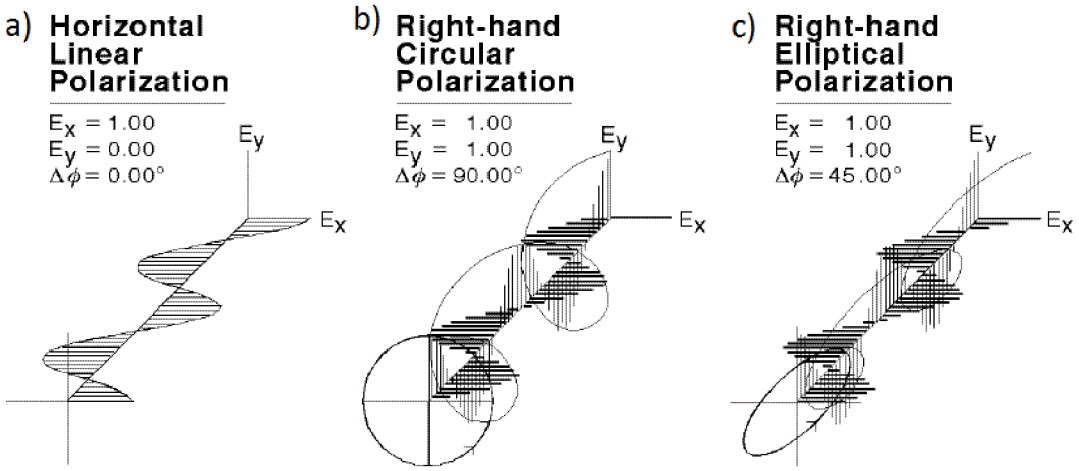

Figure 2-10 Polarisation state based on the electric field components: a)parallel polarisation, b) circular polarisation, c) elliptical polarisation [156]

When the difference in phase of the two components is ±π/2, the polarisation is called circular. In this case, the resulting vector is not only oscillating in a straight line on the x-y plane as for linear polarisation, but it rotates around the propagation axis (Figure

2-10b). When the difference in phase is π/2 and the electric field at a fixed position z is rotating in the clockwise direction, the beam is considered a right circularly polarised beam. In contrast, when the difference in phase is -π/2, the vector is considered to rotate in a counter-clockwise direction, and the beam is identified as a left circularly polarised beam. In both cases, the resulting trajectory of the end point of the electric-field vector defines a circle on the x-y plane.

When both components are present, and the difference of phase is not a case seen before, the polarisation state is considered elliptic because the end point of electric field vector defines an ellipse in the x-y plane. Figure 2-10c shows a case of elliptical polarisation where the modulus of the two electric fields are equal to 1 and the difference in phase is π/4. The direction and the size of the two ellipse axes are defined by the difference in phase and the modulus value of the two electric field components. As for the circular polarisation, it is possible to identify the rotation direction (clockwise or counter-clockwise).

2.4.2 Devices to change laser polarisation

Several devices based on different techniques can be used to change or modify the polarisation state of a laser beam. The devices used in the research work will be described in detail in Section 3.2.4. Here is presented a general overview.

The first devices are the polarisers: their peculiarity is to have a transmission axis. They have the capability to transmit the component of the electric field that travels on their transmission axis while they block the component orthogonal to the transmission axis. There are three types of polariser depending on which method is used to block the orthogonal component: absorption, reflection or refraction.

The polarisers, based on the absorption of one component of the electric field, are made by a material that has an anisotropic molecular structure whose response is sensitive to the applied electric field. For a laser beam with the emission wavelength in the infrared, the most common technology used is the wire grid polariser. It is composed of closely spaced fine wires stretched in a single direction that absorb the components that are parallel to the wires and transmit the components that are orthogonal.

The reflection-based polariser can select one of the electric field components; they work on the principle that the reflectance of two dielectric materials depends on the polarisation. A classic example is the Brewster plate [87], which employs the Brewster angle principle. At the Brewster angle of incidence, the parallel component is

completely transmitted; meanwhile, the perpendicular component is partially transmitted and partially reflected. This means that the reflected beams will have a single component, the one in the y axis, thus resulting in perpendicular polarisation.

The refraction-based polarisers are primarily used to produce the polarising beam splitter. The beam splitters are composed of two cemented prisms comprising anisotropic materials. When light enters into the anisotropic material, the two components refract it at different angles, and the beams propagate to different directions. Combining it with the Brewster angle, it is possible to obtain two beams separated by a high angle. Each one of the two beams is made of a single component of the electric field, so the device provides one exit with a beam polarised in a parallel manner and an exit with a beam perpendicularly polarised, as shown in Figure 2-11.

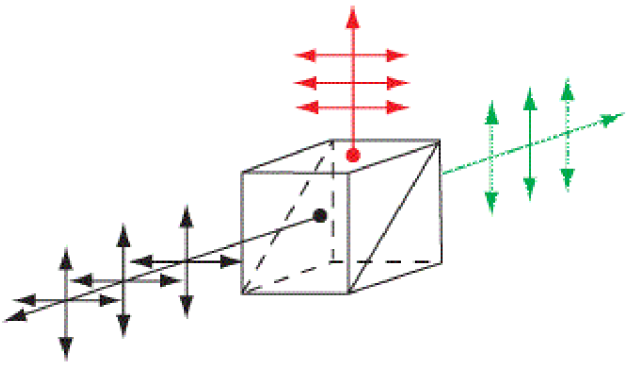

Figure 2-11 Polarising beam splitter principle [88]. Both components (black) enter in the cube: the parallel component is reflected (red) and the perpendicular component is transmitted (green)

Another device used to modify the polarisation are wave retarders. They have the capability to change the polarisation state from one to another by retarding one of the electric field components. The wave retarders are also known as waveplates. They are made of a birefringence material that has a slow axis and a fast axis, both on the x-y plane. The phase velocity of light is slightly higher on the fast axis than on the slow axis. In this way, it is possible to introduce a retarding action between the two components, which means to change the phase difference of the two components. As seen in Section 2.4.1.1, a difference in phase corresponds to different polarisation states; thus, it is possible to change from one polarisation state to another. Moreover, considering the thickness of the element, it is possible to introduce a retarding action that is directly proportional to the thickness of the element and inversely proportional to the wavelength. Obviously, the designed value of optical retardance is limited to a range of wavelength and incidence angle [89].

2.4.3 Laser polarisation on linear absorption: Fresnel laws

In Section 2.4.2, the comment was made that the polarisation state has some effects on the amount of reflected and transmitted light. Figure 2-12 shows the effect of an incident electromagnetic wave which hits an interface between two materials. The incident wave that travels through material 1 has a refractive index n_1. When the wave hits the interface between material 1 and material 2, it can be partially reflected and/or refracted (i.e. transmitted). If the incident wave hits the interface with an angle θ_1, it is reflected by an angle θ_3, where $\theta_1 = \theta_3$. The incidence angle is then equal to the reflected angle, while the angle of the transmitted wave is described by Snell's law:

$$\boldsymbol{n_1\, sin(\vartheta_1) = n_2 sin(\vartheta_2)} \qquad (2.31)$$

where n_2 is the refractive index of material 2.

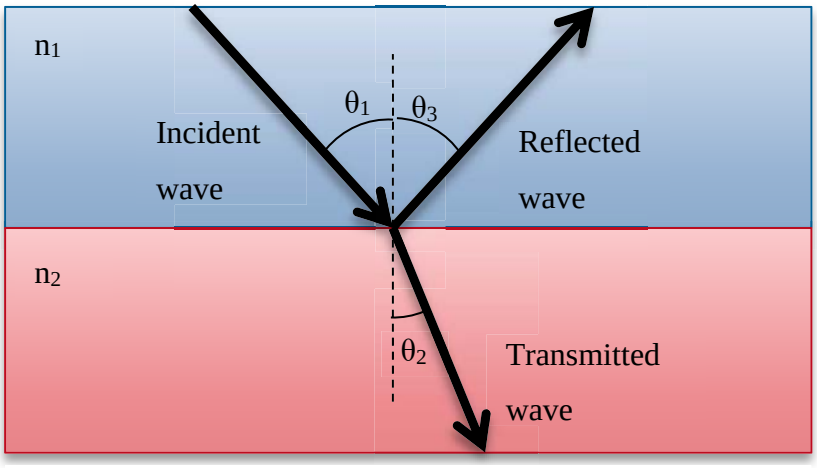

Figure 2-12 Reflection and refraction of an electromagnetic wave incident on a surface

If Snell's law describes the relation between the incidence angle and the refractive angle for a generic wave, the Fresnel equations described the amount of reflected (and then transmitted) wave, taking into account the polarisation state [86]:

$$\boldsymbol{r_x = \frac{n_1 cos\theta_1 - n_2 cos\theta_2}{n_1 cos\theta_1 + n_2 cos\theta_2}, \quad t_x = 1 + r_x}$$
$$\boldsymbol{r_y = \frac{n_1 sin\theta_1 - n_2 sin\theta_2}{n_1 sin\theta_1 + n_2 sin\theta_2}, \quad t_y = (1 + r_y)\frac{cos\theta_1}{cos\theta_2}} \qquad (2.32)$$

where r_x and r_y are the reflection coefficients and t_x and t_y are the transmission coefficients for parallel and perpendicular (x and y) components of the electric field, respectively.

It is evident how the polarisation can influence the reflection and the transmission of the laser beam inside a material. However, it comes directly from Eq. *2.32* that for normal incidence (θ_1=0) of the laser beam on interface, the reflection coefficients for linear and perpendicular component are equal. This means that the polarisation affects the transmission (and then the absorption) only when the laser incidence is not equal to 0º.
For the reason just given, the effect of polarisation seems to affect only the processing of complex 3D structures when the laser beam does not hit the surface at normal incidence. The effect of polarisation when the incidence is not normal is well defined by Eq. *2.32*. From Eq. 2.32 the only material parameter related to polarisation during linear absorption is the refraction index. Only for the birefringent material the refraction index can be related to the crystal orientation, while for all the other materials it is constant on all direction and does not depends on crystal orientation. For this reason, crystal orientation of the material it is not considered for linear ablation of isotropic material. However, this polarisation effect is valid only for linear interaction between the laser and material. Indeed, as described in Section 2.2.2 and Section 2.2.4, for ultrashort pulses the laser material interaction includes several nonlinear phenomena. These nonlinear phenomena can change the effects of polarisation on material processing, and they will be discussed in the next section.

2.4.4 Polarisation in nonlinear laser ablation

As described in Section 2.2.4, the pulse duration influences the approach to laser material ablation modelling for ultrafast laser pulse duration because the photon-phonon coupling time is shorter than the pulse duration. This concept can be extended to the polarisation introducing nonlinear effects. The studies that highlight nonlinear effects based on the polarisation state will be discussed in the following.
One study by Ji et al. [90] reported the effect of laser polarisation on the crater shape using an 800 nm 50 fs laser with a repetition of 1 kHz. In this work, a silicon sample was patterned using three different polarisation directions: 0º, 45º and 90º. The crater shape obtained by single pulse was evaluated, and asymmetry along one axis was identified. Indeed, the crater obtained shown an elongation along the axis parallel to the polarisation even though the energy beam distribution did not show any degree of asymmetry because of the change of polarisation. This effect is explained by the increased absorption along the laser polarisation defined by the Fresnel coefficients as well as by the electric field redistribution induced by the surface structure. However,

this effect was present only by pulse with fluence just above the ablation threshold; while increasing the pulse fluence, the crater shape became round in accordance with the laser beam energy shape (Figure 2-13) [90].

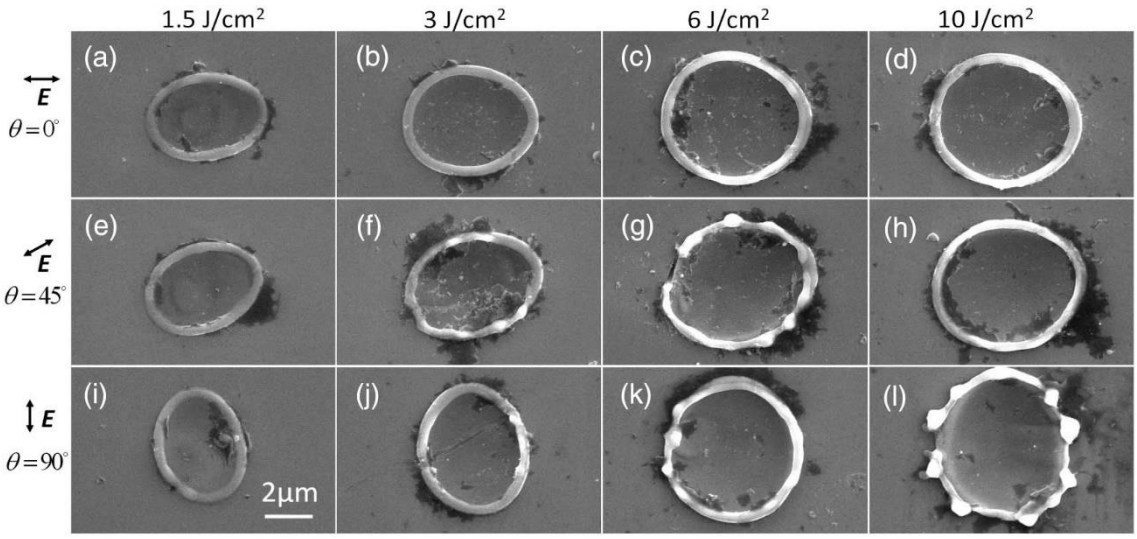

Figure 2-13 Crater morphologies of silicon irradiated by a femtosecond laser with a single shot by increasing fluence and rotating the polarisation direction [90]

The polarisation influence on the crater shape for the single-pulse ablation mode is not as interesting as it is for the multiple pulse mode that drives LIPSS. LIPSS describes the periodic structure created on the patterned material surface, which is typically smaller than the laser beam spot size used for the material ablation.

2.4.4.1 LIPSS formation theories

LIPSS were first noticed with a ruby laser during the ablation of a germanium (111) wafer [91]. Since that discovery, several theories have been postulated to try to explain and understand the effect. In this first paper by Birnbaum [91], LIPSS were attributed to the diffraction effect caused at focus on a lens. It was thought that diffraction generated by the lens aperture was the reason for LIPSS formation because by changing the focal length of the lens there was a slight changing of the periodicity of the structures. Although during the following years this explanation was modified, it was clear from the beginning that LIPSS were caused by electromagnetic interference.

The following theory tried to explain LIPSS formation by frozen surface acoustic waves [92]. During irradiation of a GaAS sample using a pulsed ruby laser, it was noticed that several patterns observed were not consistent with the interference effect at optical frequencies. It was supposed that LIPSS were arising from another process that did not

correlate with optical interference. To explain this behaviour, it was suggested that during the ablation, the melted and re-grown material was redistributed along nodal lines of a standing acoustic wave pattern that corresponded with the axial mode beat frequencies.

Later, LIPSS were explained by supposing that plasma oscillations could be involved in their formation [93]. In the published work, a CO_2 laser was used to pattern a Ni_xP_{1-x} surface. By the results analysis, it was expected that the laser electric field would excite some oscillation parallel to the surface. If the surface had irregularities, the laser light that scattered at a tangent to the surface could produce a standing wave pattern. Incident, reflected, and diffracted waves could induce an electric field that would drive localised plasma oscillation. These plasma oscillations could produce enough heating to be able to ablate the sample and then form LIPSS.

After almost a decade of LIPSS discovery, it has become clear that LIPSS can be considered a universal phenomenon [94]. At that time, it was already reported that LIPSS were identified on a wide variety of materials, polaritons active and polaritons inactive, with different surface micro roughness, and over a broad range of wavelengths. Despite some controversy, the more accepted theory to explain LIPSS was that the patterns were resulting from inhomogeneous energy deposition associated with the interference of the incident beam with a surface scattered field. Moreover, the role of several laser parameters on LIPSS formation began to be evaluated. In particular, for the concerns regarding polarisation, it was reported that LIPSS were obtained for circularly and linearly polarised beams, contrary to earlier suggestions.

The first complete theory to explain LIPSS was presented by Sipe, et al. [95], and it was followed by their experimental study [96]. Researchers developed a theory (also known as Sipe's theory from the name of one of the authors) that associated the Fourier components of LIPSS to the corresponding components of the inhomogeneous energy deposited on the sample. It was assumed that the inhomogeneous energy deposition was caused by the surface roughness. Starting from the above assumption, strong peaks in deposition in Fourier space were found. These peaks were leading to the prediction of induced fringe patterns that revealed that the LIPSS spacing was dependent on the angle of incidence and that the orientation was dependent on the polarisation of the laser beam. However, this model showed incongruence between parallel and perpendicular polarisation: in the first case, the results were dependent on surface shape and fill factor; in the second, they were not. This left some open issues about the nature and modelling

of LIPSS. The following experimental work was conducted on silicon germanium and aluminium samples, focusing on the effects of polarisation and angle of incidence. The results showed that in the area affected by the laser ablation, more intricate, detailed structures were generated than what was previously seen. However, large areas showed periodic ripple patterns that were oriented perpendicular to the polarisation state. Moreover, observing the LIPSS evolution, shot by shot, the fact was highlighted that both the initial and laser-induced surface roughness played important roles in the evolution of the damage, suggesting a self-formation contribution by the structures themselves.

Starting from all the theories described previously, Sipe's theory was the most generally accepted because it was capable of explaining LIPSS formation by the surface plasmon polaritons (SPP) coupled with the laser pulse electromagnetic field [97]. The model coming from the theory, which combines the formation of SPP with Drude's model for the transportation of electrons in the materials, was able to explain some effects, such as the variation of the LIPSS periodicity observed in previous work. In addition to the SPP formation, due to the high amount of electrons excited from the material by the laser beam, the model considers the nonlinear effects coming from this high electron density. The high amount of electrons caused several nonlinear effects; the key effect is the change in the dielectric constant.

As shown in the next paragraph, the SPP concepts as well the concepts introduced by the Drude's model can explain most of the LIPSS behaviours. However, some open points remain for clarification.

2.4.4.2 Influence of laser parameters on LIPSS formation

Together with a theory capable of explaining the mechanism and nature of LIPSS, the impact of the laser parameters on LIPSS characteristics was investigated. Laser wavelength, angle of incidence, energy deposited, and polarisation were the more relevant laser parameters on the LIPSS formation, while the more attractive LIPSS characteristics were the periodicity and orientation.

LIPSS periodicity, which indicates the period between one structure and the closest other structure, typically has been measured as equal to or lower than the wavelength. Borowiec et al.[98], studied the formation of LIPSS for InAs, InP, GaP, and Si at three different wavelengths (800, 1300, and 2100 nm). For all materials, LIPSS periodicity was lower than the wavelength. Using a wavelength of 800 nm, the periodicity range was between 650 and 730 nm; with a wavelength of 1300 nm, the periodicity varied

between 1050 and 1150 nm and using a wavelength of 2100, the periodicity was between 1600 and 1900 nm (Figure 2-14). In addition to the effect of the wavelength, it was identified that LIPSS periodicity depends also on the number of pulses. Indeed, in the same study, it was reported that increasing the number of pulses resulted in decrease of the periodicity. For a high number of pulses using an 800 nm wavelength, the periodicity was from 170 to 260 nm; for a 1300 nm wavelength it was from 300 to 310 nm; and for a 2100 nm wavelength it was from 430 to 470 nm. These structures with a shorter periodicity are typically identified with the term high spatial frequency LIPSS (HSFL). Furthermore, the structures with periodicity close to the wavelength are identified by low spatial frequency LIPSS (LSFL). The orientation of HSFL is not yet completely defined. In some works, the HSFL are oriented perpendicular to the polarisation state as LSFL are; however, other papers found that HSFL are parallel to the polarisation state and perpendicular to LSFL. A review on HSFL [99] was reported: almost half of the papers indicated that HSFL were perpendicular while the other half indicated that HSFL were parallel to the polarisation. In the same work, HSFL were successfully generated on titanium surfaces using a simple one-step processing approach. However, in semiconductors and in dielectrics, the process to generate HSFL was not as direct and the cause was identified on the intrapulse transient changes of the optical properties. The physics reason behind the HSFL formation is still controversial. Some papers agree on the fact that they are caused by the generation of a second harmonic. For example, Harzic et al.[100] carried out a study of HSFL on silicon using a megahertz laser repetition and reported a LIPSS periodicity (Λ) of $\Lambda = \frac{\lambda}{2}\eta_{\lambda}$. Then, because of LIPSS periodicity close to $\frac{\lambda}{2}$, second harmonic generation was expected to occur in the region close to the surface to drive the mechanism of HSFL formation. By the consideration made above, the relation between the refractive index and LIPSS formation was highlighted, focusing on the nonlinear interactions.

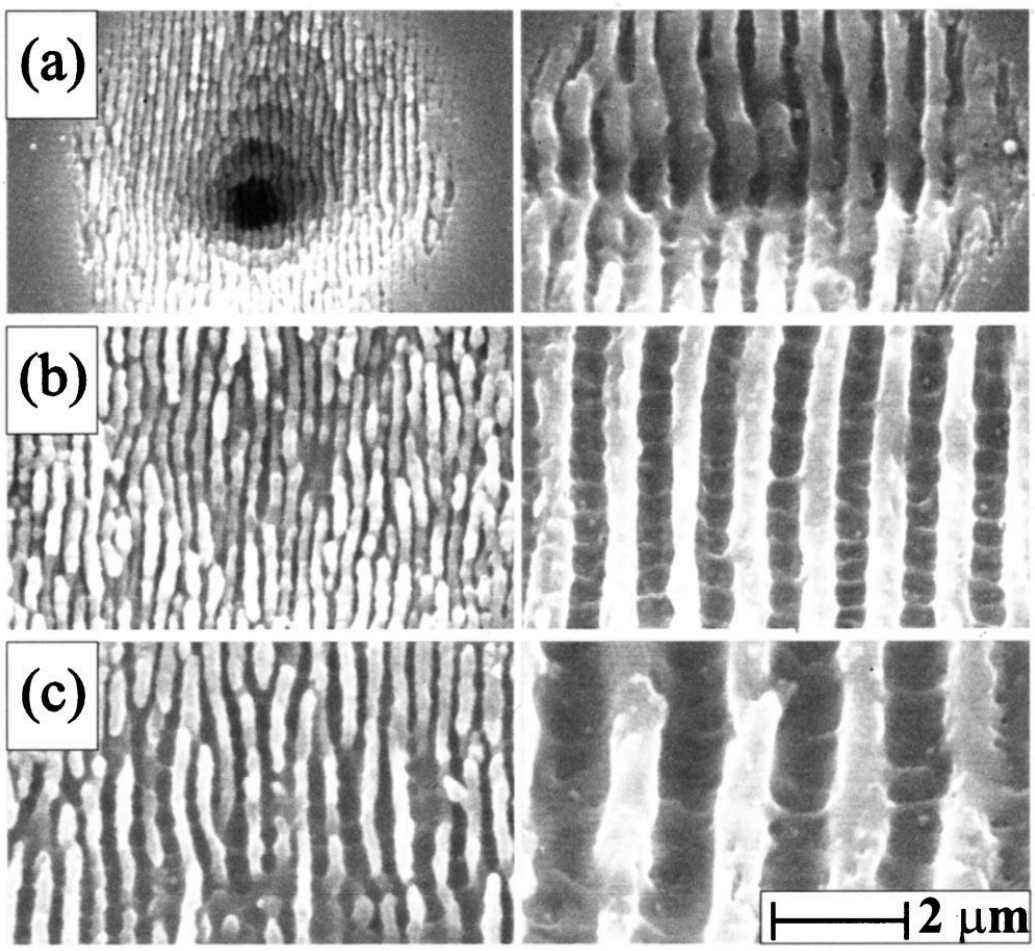

Figure 2-14 HSFL(left) and LSFL (right) formed on the surface of GaP irradiated by (a) 800 nm, (b) 1300 nm, and (c) 2100 nm pulses [98].

Another dependence highlighted was the one related to the angle of incidence. When an electromagnetic wave hits a surface at an angle different from 0º, the period of the wavelength by itself can be considered larger from the point of view of the hit surface. Consequently, the interference between the electromagnetic wave and the surface electromagnetic field becomes different as well. The effects of angular incidence of the laser beam on a nanostructure-covered metal were studied [101]. LIPSS periodicity increased by increasing the angle of incidence. Figure 2-15, from the top to the bottom, shows the LIPSS periodicity evolution from 0º to 75º.

The variation of LIPSS periodicity (Λ) due to the different angles of incidence (θ) is simply described by the relation

$$\Lambda = \frac{\lambda}{Re[\eta] \mp sin\,\theta} \qquad (2.33)$$

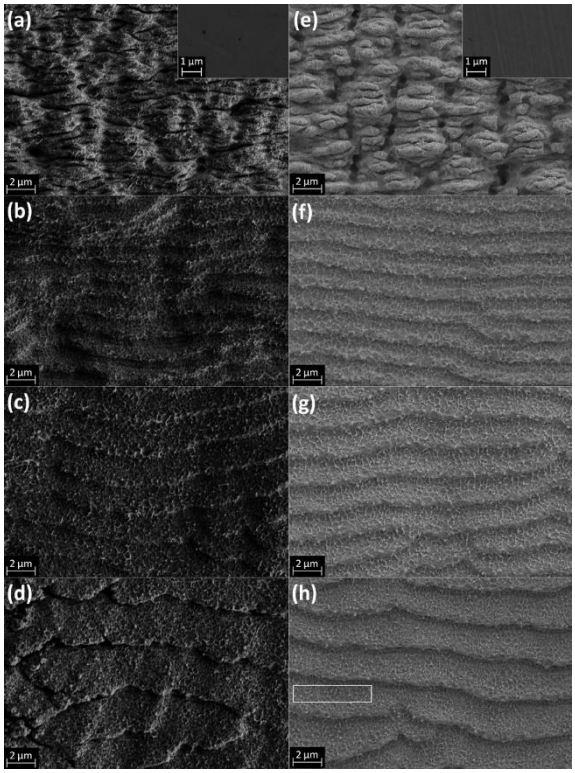

Figure 2-15 SEM images of LIPSS formed on two metals by femtosecond laser irradiation at different incident angles of 0º, (a) and (e); 35º, (b) and (f); 55º, (c) and (g); and 75º, (d) and (h) [101]

The influence of the energy deposited (by increasing the fluence or the number of pulses) on the sample was evaluated in several works and was identified as a reason for periodicity changing. Bose et al. studied the LIPSS formation in monocrystalline silicon irradiated by femtosecond single and multiple linearly polarised laser at 800 nm [102] and [103]. A decrease of LIPSS periodicity up to 37% by increasing the number of pulses was highlighted. The results were explained by a grating-assisted SPP excitation mechanism. The structure depth formed during the first laser pulses increased with the number of pulses. This deepening of the LIPSS could drive to a redshift of the SPP resonant wavelength. The redshift means a decrease in the wavelength value and then a decrease in the period of the SPP. The change of the SPP leads to a different interference with the incoming laser beam and then to a decrease in the LFSL periods during the multi-pulse feedback phase. Meanwhile, it was demonstrated that the change in LIPSS periodicity caused by the increase of the number of pulses was due to the admixture of the field-distribution effect and the grating-coupling effect [97]. Specifically, the SPP-laser interference was considered the dominant mechanism of LIPSS formation but, as ripples grew, the grating assisted SP-laser coupling was identified as the most relevant cause for the periodicity evolution.

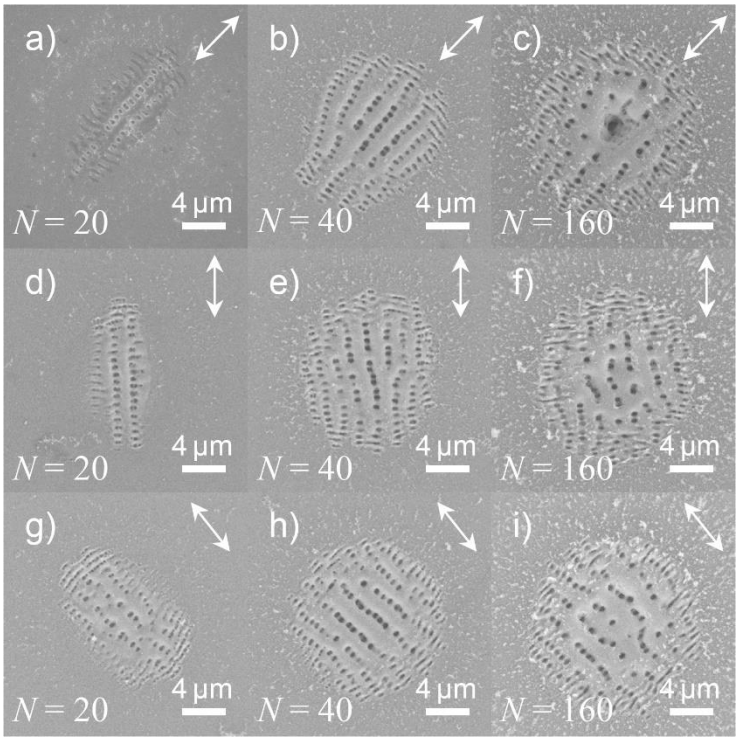

Figure 2-16 Asymmetric crater evolution with increasing of number of pulse (N = 20, 40, and 160) observed in the (110), (010), and (−110) directions corresponding to figures (a,b,c), figures (d,e,f,) and figures (g,h,i) respectively. The arrows indicate the polarisation of the laser light [104]

It was also noted that polarisation was driving anisotropy on the area patterned. It was reported that ripples formed in the initial stage facilitated the ablation along the direction parallel to the polarisation, leading to the formation of an elliptical ablated crater [104]. By modelling the electric field distribution after formation of the first structures, it was demonstrated that the structures by themselves were driving the asymmetry of the crater. The electric field resulting from the coupling of the excited surface plasmon and the scattered wave was elongated along the polarisation direction state, driving an elliptical distribution. This asymmetry disappeared, increasing the number of pulses, and the affected area evolved from an elliptical shape to a circular one. This evolution was explained by the formation of 2D nanohole arrays (Figure 2-16) in the centre of the crater that redistributed the electric field, reducing and then resetting the asymmetry effect.

The amount of energy deposited was considered only by a multi-pulse process, but recently it was demonstrated that fluence must also be considered. It was demonstrated that the LIPSS formation process on a nanoparticle-covered silicon sample was strongly dependent on laser fluence [105]. The experimental results showed that LIPSS were

forming using pulses of 1.6 J/cm^2, but by increasing the fluence up to 6.5 J/cm^2, LIPSS were disappearing. This result was explained by the competition between the LIPSS structuring and surface melting. In fact, a non-thermal melting could be generated by the femtosecond pulse, which could produce a hydrodynamic flow on the surface layer. For the case in which the laser fluence value was large enough, the flow had a dominant role in preventing the LIPSS formation. In addition to the amount of the energy deposited, the temporal modulation of the energy (the pulse temporal width and the laser frequency) was identified as capable of modifying LIPSS formation.

It was demonstrated that the polarisation-dependent anisotropy of LIPSS on silicon could be modified via a train of pulses [106]. By varying the pulse delay from 100 to 1600 fs within a double train of pulses, it was possible to reduce the contribution of the first generated ripples on the final generated elongation. The polarisation-dependent geometrical morphology of the LIPSS could be enhanced or reduced based on the delay applied between the two pulse trains. A similar method based on temporal shifting of two laser pulses was successfully used to change the LIPSS periodicity on polycrystalline ZnO films. An example of varying the pulse separation from 0 to 7 ps changed the LIPSS period from 650 nm to less than 200 nm [107].

The effect of the laser pulse temporal shape on LIPSS was investigated [108]. A pulse train composed of sub-pulses characterised by a precise temporal separation were applied to the silicon target. It was observed that the LIPSS amplitude was enhanced using a separation between pulses of 128 fs. This behaviour was explained by combining the Sipe and Drude theories that permit calculation of the residual carrier density before the next sub-pulse arrives; this density is then added to the carrier density generated by the sub-pulse. Applying the two models together enabled calculation of the carrier density at the end of the pulse train, which was considered the leading value of the LIPSS formation. A maximum of the efficacy factor for a separation between pulses of 128 fs was identified, and consequently a maximum in the LIPSS amplitude was obtained.

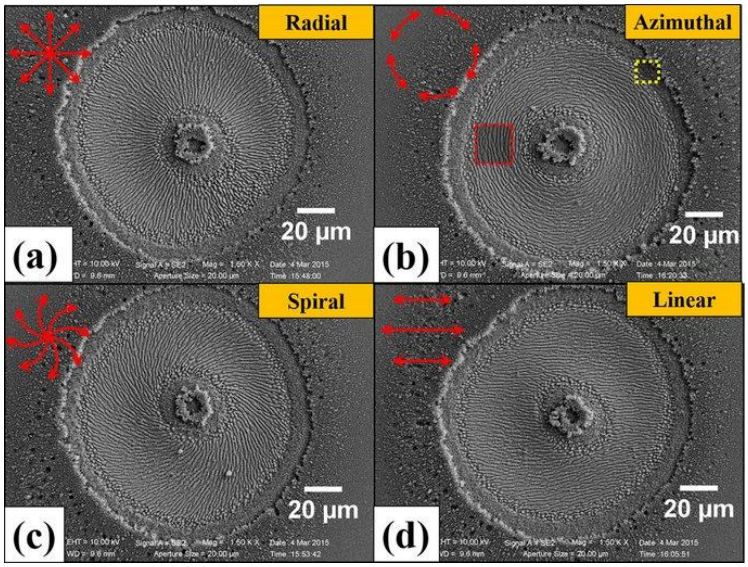

Figure 2-17 LIPSS obtained by irradiation with different SoP: (a) radial, (b) azimuthal, (c) spiral, and (d) linear [8].

The relation between polarisation and the LIPSS orientation was highlighted in Section 2.4.4.1, but recent studies have shown how numerous novel LIPSS orientations can be achieved by modifying the polarisation using an optical vortex. using a q-plate, it was possible to tune the state of polarisation of the optical vortex. Using radial, azimuthal, spiral, and linear states of polarisation, four LIPSS orientations were obtained: radial, azimuthal, spiral, and classical perpendicular LIPSS (Figure 2-17) [8]. Despite using novel polarisation states, similar behaviours to LIPSS generated with classical polarisation states were identified (e.g. increasing of the periodicity with variation of number of pulses or fluence).

It is obvious that the laser parameters influence LIPSS formation; however, because the generation system is not completely clear, the effects of laser parameters on LPSS formation must be investigated more thoroughly.

2.4.4.3 Feature and crystal orientation effects on polarisation dependence of LIPSS formation

As explained in Section 2.4.4.1, LIPSS can be related to the surface roughness. Recent studies have shown that micro fractures and structure can drive LIPSS formation by competing with polarisation in the LIPSS direction. Murphy et al.[109] studied LIPSS near 110 nm-tall Au micro-structured edges on Si substrates after single-pulse femtosecond irradiation. The contribution of Fresnel diffraction caused by the fracture, together with the SPP excitation, were investigated. It was shown that when the electric field was perpendicular to the edge, LIPSS were mostly formed parallel to the edge.

When the polarisation vector was parallel to the edge, the LIPSS were formed in both directions, perpendicular and parallel to the edge. It was revealed that in the case when the polarisation state was parallel to the surface features, Fresnel diffraction dominated LIPSS formation. In the case of polarisation perpendicular to surface features, the Fresnel diffraction effect was minimised by increasing of the SPP excitation effects.

Recently, it was found that not only the surface features can influence LIPSS direction but also the crystalline structure of the material has an effect on LIPSS direction and threshold formation. A study on a polycrystalline sample was conducted to identify any dependence of the LIPSS process formation on the crystal structure [110]. Significant differences were observed at low-to-medium number of laser pulses. In fact, when the sample was irradiated with a medium number of pulses, the LIPSS formation on the sample part that was (111) oriented was more difficult and the structures appeared less periodic compared to parts with other crystal orientation. In addition to the dependence on the crystal orientation, it was identified that the crystal with highest lattice defect storage was showing a smaller LIPSS affected area.

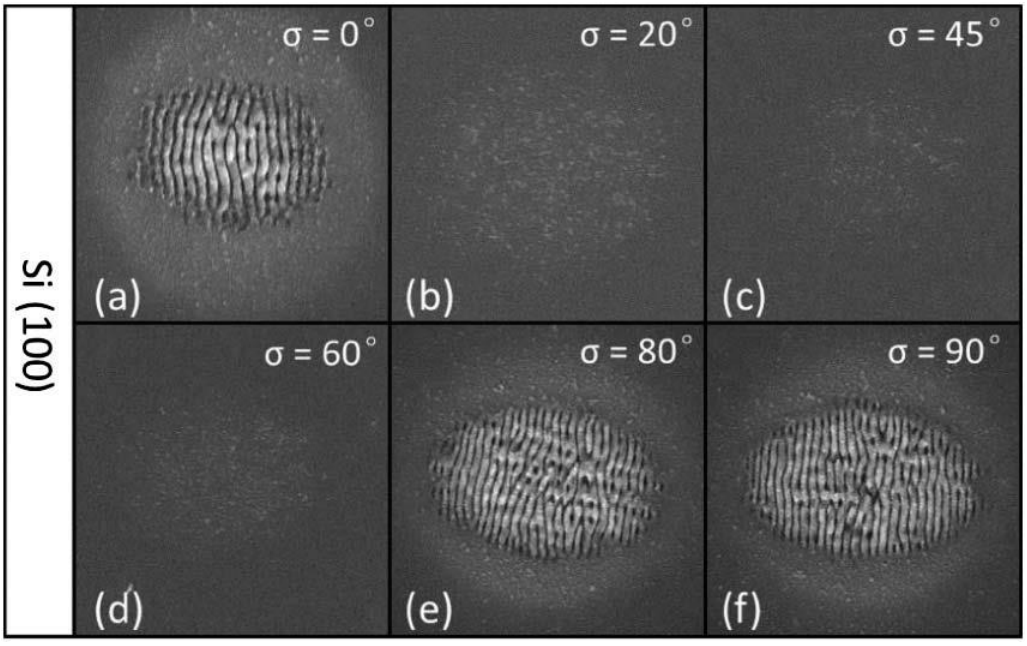

Figure 2-18 SEM images of Si (100) LIPSS irradiated from a femtosecond laser source. From (a) to (f) the sample is rotated from 0º to 90º [110].

Jiang et al. [111] tested the effects of crystal orientation on LIPSS on a Si (100) wafer processed by a linearly polarised femtosecond laser. By rotating the sample and keeping constant the laser beam, the matching between the polarisation and the lattice axis was evaluated. It was found that LIPSS formation was sensitive to crystal orientation (Figure 2-18) with a $\pi/2$ modulation. Furthermore, when the angle between polarisation and

crystal orientation was changed from 0º to 180º, the amount for the area affected by LIPSS could be described by a quasi-cosinusoid function. From this behaviour, it was discovered that generating LIPSS was much easier when the electric field vector was aligned with the lattice axis $[011]/[01\bar{1}]$. This effect was explained by the anisotropicity in the nonlinear ionisation rate along different crystal orientations. In fact, the effective electron mass is dependent on the crystal axis, and it could drive anisotropic excitation of the electrons in the conduction band.

2.4.4.4 LIPSS analysis techniques

LIPSS analysis can be difficult because they can be generated over a large surface, but the analysis must be conducted with a sub-micrometre resolution because of the size of the structures. The most common way to analyse LIPSS is by an SEM. In fact, all the result data reported in section 2.4.4.2 and section 2.4.4.3 were made using SEM. The SEM generally enables the total area affected by a laser pulse to be included in a single acquisition and a sufficient resolution to analyse LIPSS without being extremely time consuming. Unfortunately, the SEM does not provide numerical information on the z axis, but the shape information along the z axis are provided by the qualitative analysis of the associated picture colours.

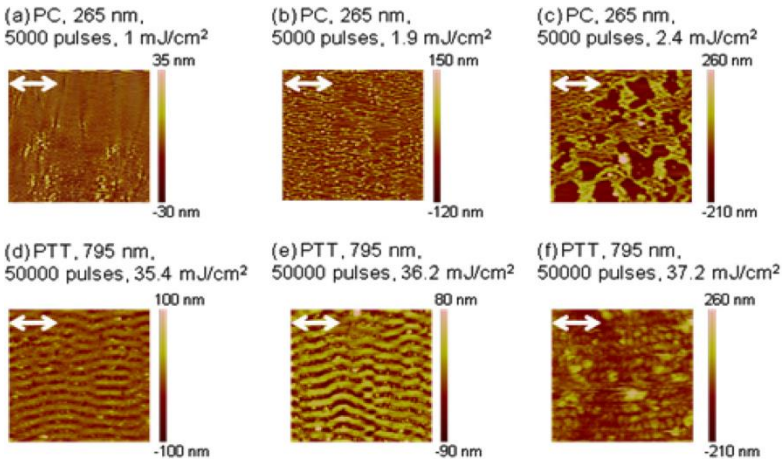

Figure 2-19 AFM analysis of LIPSS. From (a) to (c) using 5000 pulses; from (d) to (e) using 50000 pulses [112]

To have a complete 3D mapping of the laser affected area by single pulse laser while having enough precision, the best method to analyse LIPSS is to use the atomic force microscope (AFM). It has been reported that LIPSS produced in thin polymer films by the multipulse irradiation of a Ti:sapphire femtosecond laser with the fundamental (795

nm) and the third (265 nm) harmonic were analysed using the AFM [112]. With the complete 3D LIPSS data analysis, it was possible to match the information related to the periodicity and the fluence together with the height of the structures. It was noticed that the period as well as the height increased as the fluence increased. The variation in period and height was more relevant using 5,000 pulses than 50,000 pulses. In fact, in the second case, the two values were almost constant. Although the AFM is more accurate and can give a complete 3D reconstruction, it is very time consuming compared to SEM analysis. For this reason, typically with the SEM, all the single-pulse affected areas were analysed, while with the AFM, this was the case with only part of it (Figure 2-19). Moreover, AFM does not give any information about eventual change of the material composition or re-solidification, while these details can be provided by the SEM. Primarily for these two reasons, the most used analysis technique for LIPSS by others is the SEM.

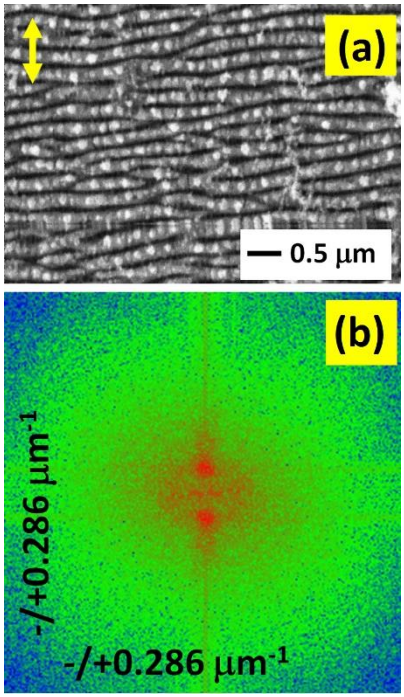

Figure 2-20 Example of application of 2DFFT: (a) SEM images of LIPSS; (b) 2DFFT of a part of (b) [112]

It is interesting to note that AFM is not necessarily needed to study LIPSS periodicity that can be obtained by analysis of the SEM. In fact, it is possible to apply the Fourier transform to conduct an analysis of the frequency spatial component of the acquired SEM images (Figure 2-20). The fast Fourier transform (FFT) in the 1D and 2D versions as well as the Power Spectral Density (PSD) were applied to evaluate the LIPSS analysis. These techniques can be applied to both the SEM and the AFM, and usually

the modulus of the PSD or of the FFT is reported. However, there is a main difference between AFM and SEM spatial frequency analysis: the modulus obtained from the SEM picture refers to the pixel colour, which is not intended to be the measured z values; the modulus obtained from the AFM represents the z values measured.

The dependence of temperature condition on the formation of LIPSS could also be evaluated using the 2DFFT [113]. It was found that LIPSS produced at room temperature were different from the ones produced at 350ºC. At 350ºC, LIPSS could be found only at the periphery area of the crater, similarly to the result using a high fluence or high number of pulses. This likely came from the enhancement of the absorption of light at elevated temperature. To evaluate the periodicities of the different LIPSS, the 2DFFT was applied.

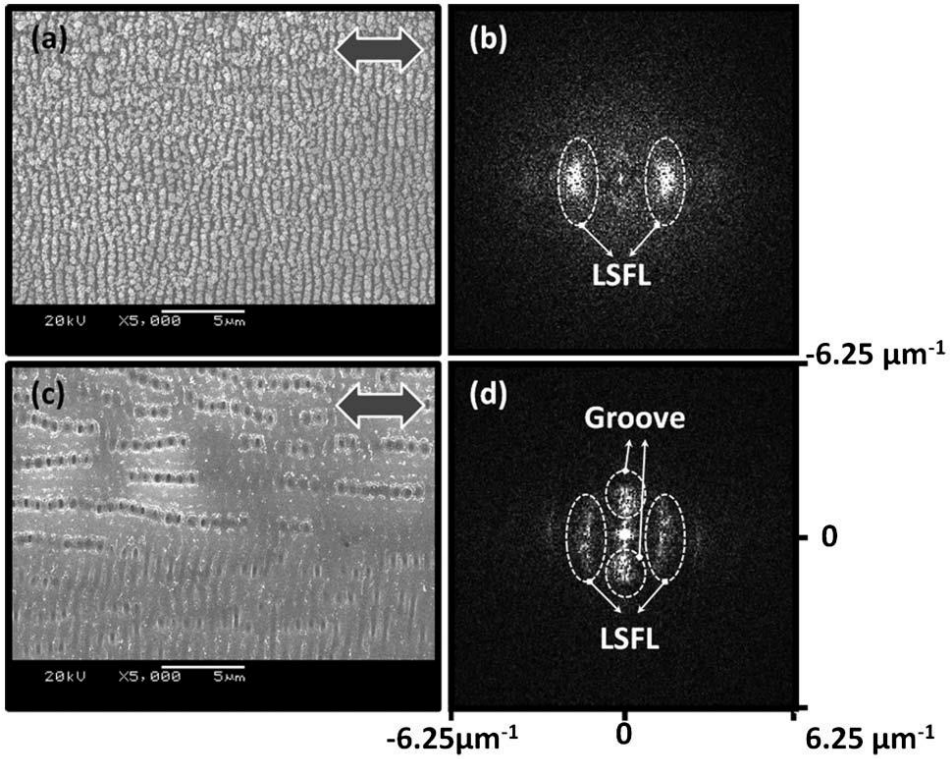

Figure 2-21 SEM pictures and corresponding Fourier transform analysis: (a) LIPSS at room temperature and (b) corresponding 2DFFT; (c) LIPSS at 350ºC and (d) corresponding 2DFFT [113].

In Figure 2-21b, the Fourier analysis shows that at room temperature, only the two peaks related to LIPSS are visible. Figure 2-21c shows two additional peaks that represented the additional grooves formed. The 2DFFT confirmed that the direction of the peaks is generally perpendicular to the LIPSS direction, and that the groove period value is higher than the LIPSS period.

Alternative to the 2DFFT analysis, other studies were based on the PSD analysis. The PSD of a discrete signal *s* composed of *N* samples with a sampling period of F_s is defined by

$$\boldsymbol{PSD_s = \frac{1}{F_s N} |FFT(s)|^2} \qquad \textbf{(2.34)}$$

The PSD was applied in a single dimension by Kumar et al. [114] on a sample analysed by the AFM. By the PSD analysis, it was revealed that the roughness increased, and the period of ripple structures decreased with increasing number of laser shots. This was due to the decrease of free electron density in the studied Indium phosphide. Comparison of Figure 2-22(e) with Figure 2-22(f) shows a shift of the peak in the 0 direction, meaning a decreasing periodicity of LIPSS.

The PSD coupled with the AFM can be an alternative to the 2DFFT coupled with the SEM. The PSD is more intuitive because it relates directly the profile extracted from the AFM analysis to the frequency study, but it considers only a small part of the LIPSS generated.

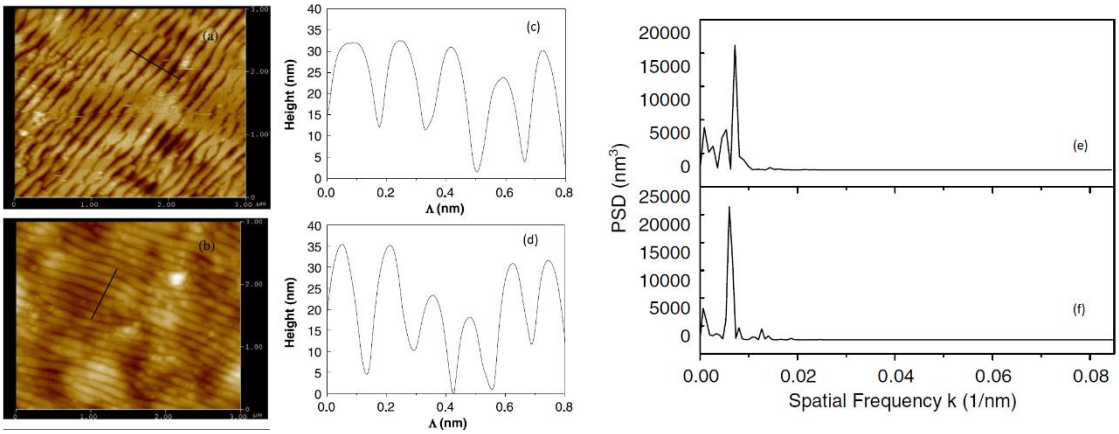

Figure 2-22 AFM and PSD LIPSS study: (a) and (b) AFM data, (c) and (d) extracted data profile, (e) and (f) PSD resulting from the profile data for 200 pulses and 400 pulses, respectively [115].

Trying to overcome the limitation of the PSD and the 2DFFT, the combination of the two techniques was attempted in other studies. Höhm et al. [115], to completely characterise LIPSS but in particular to have detailed information about the periodicity, applied both techniques. Since the LIPSS were sensitive to the fluence at the edge of the crater, where the fluence is lower compare to the centre, different structures were generated in the centre. For this reason, a limited central area was analysed. It was evaluated first by analysing characteristic peaks in the 1D PSD and then by analysing peaks in the 2DFFT of the selected regions. Therefore, while the 2DFFT provided a

completed 2D signature of LIPSS, the 1D analysis provided a more accurate and consistent value for the periodicity.

2.5 Summary of open research issues

It has been highlighted how the laser beam parameters (i.e. laser pulse duration, energy beam shape, polarisation) can affect ablated crater morphology. The multitude of the physics factors that contributes to the ablated crater morphology do not allow the description of the impact of the laser parameter relations suitable for the engineering environment. Thus, three main open research issues, which relates three laser parameters (pulse duration, energy beam distribution and polarisation) to the crater morphology (i.e. crater shape and periodic surface structures) were identified.

1. Research issue 1: crater shape and pulse duration. As highlighted in Section 2.2, laser pulse duration is one of the most relevant laser parameters which drives the phenomena involved in laser ablation. Because of the wide range of the pulse durations available and the various typologies of phenomena involved, several effects can be distinguished on a crater, depending on the laser pulse duration. In literature the following issues related to the crater ablated at different pulse duration regimes were highlighted: *i)* the melting phase in microsecond regime inducing the material re-deposition inside and around the crater; *ii)* the phase explosion in the nanosecond regime and the particles ejecting inside and around the crater; *iii)* smaller effects such as the formation of a ring around the crater in picosecond and femtosecond regime. However, the description of the experimental crater 3D shape lacks sufficient information. In fact, the crater characteristics provided are only complementary and do not give information on the total 3D crater shape. It is generally thought that the experimental crater shape is similar to the energy beam shape distribution (typically Gaussian), but an accurate analysis of it is not available. Thus, a systematic study on the crater shape is fundamental to evaluate the impact of the pulse duration on the ablated crater shape. In particular, the effects of heat diffusion, which can be directly associated to the pulse duration, can play a fundamental role on driving the crater shape. A complete description of the crater shape based on pulse duration is key to improving the modelling required, in particular for the multi-pulse ablation process that leads to good achievement of complex 3D structures.

Moreover, the knowledge of the 3D crater shape can be applied to the laser material modelling as well (e.g. on the model developed on STEEP project)

2. Research issue 2: crater shape and laser energy beam distribution. Section 2.3 reported how the laser beam can be modulated to obtain several energy beam distributions. Changing the energy beam distribution is one of the most common ways to obtain a crater shape with particular characteristics (e.g. a flat-top profile or a square x-y section). The capability to obtain alternative energy beam distribution was discussed in several papers demonstrating the possibility to obtain a crater shape such as doughnut, square, and triangular. Although devices capable of modifying the energy beam shape distribution already have been successfully applied in some industrial environments, sufficient knowledge of the effect of thermal diffusion on the final crater shape is lacking. Indeed, because of the thermal effect induced over a certain pulse duration, the crater shape can differ from the original energy beam distribution. Then, the knowledge of how the thermal diffusion can modify the crater is relevant to understand when the benefits coming from the energy beam shaper limited from the pulse duration on the final 3D crater shape were achieved (e.g. when a flat-top derives to something that is rounded). In addition, the knowledge of the impact of the thermal diffusion on the 3D crater shape can improve the model output and, consequently, the strategy to obtain a 3D complex structure can be improved based on the different crater shapes.
3. Research issue 3: crater morphology and polarisation. Laser polarisation is generally considered as a secondary parameter on laser ablation, and it is not considered in the majority of the works. However, as presented in Section 2.4, the polarisation can affect the crater morphology and has a determining role on orientation of LIPSS. Despite several studies on LIPSS, knowledge of the correlation between the influence of polarisation on LIPSS and on the crater shape is lacking. LIPSS are usually generated using ultrafast laser pulses, where several nonlinear effects occur and the Snell's Law on classical laser absorption is not valid. Moreover, LIPSS formation and the crater shape are treated as distinguishable phenomena: the first is modelled with the plasmon model, and the second with the two-temperature model. Furthermore, establishing a correlation between the two can be complex. However, identifying a relation between the crater shape and the LIPSS formation, together with the

polarisation, can be key to increasing the knowledge of the nonlinear phenomena involved in the laser material interaction during ultrafast laser ablation. Moreover because of the quite recent interest developed in LIPSS, they have been analysed in several ways (e.g. using AFM, SEM and then applying PSD, DFT, and 2DFFT). However, there is still not an effective/efficient method that can be used to completely analyse the LIPSS, and in particular, to quantify the amount over a certain area. To this end, a fast and reliable method to measure the amount of LIPSS would be fundamental to improve the analysis.

3 MATERIALS AND METHODS

In Chapter 3, all the materials and laser facilities used as well as the analysis facilities are described and justified. In the first section, the silicon samples used in this thesis are described, including the size, quality of the surface, and crystalline orientation. In the second section, the laser facilities are described: three laser facilities were used to investigate the broad range of parameters examined in this thesis. For each laser facility the information of the laser source typology, laser beam delivery system, and integrated optics is provided. Different levels of detail are given for the different laser facilities based on the role of each facility in this thesis. In addition, a description of additional optics introduced in the standard beam path is included because the additional optics are fundamental for subsequent chapters of this thesis.

Because of the different scales of the structures created, from the micro- to the nano-scale, several facilities for analysis are introduced. The equipment was divided based on the type of analysis that they were able to provide: quantitative when they could provide complete 3D crater shape information, qualitative when the data collected could not give a complete 3D mapping of the crater.

3.1 Silicon sample

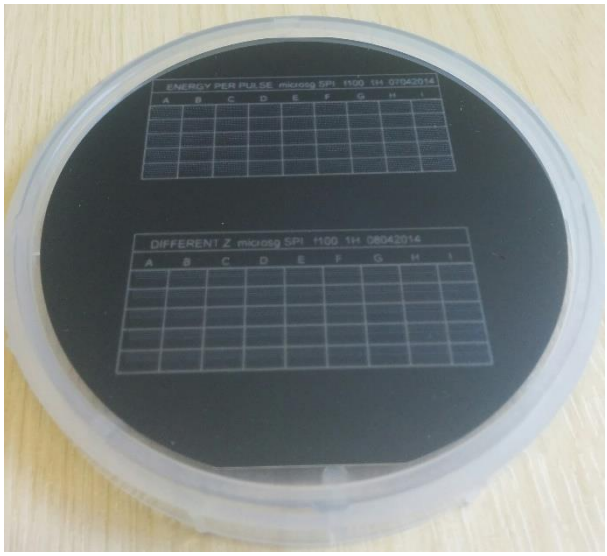

Figure 3-1 Example of a laser processed silicon wafer

The study was conducted on 3-in silicon test grade wafers obtained by the Czochralski process. They were N doped (phosphorus), single side polished with a thickness of 380 ± 50 μm. The linear resistivity of the sample was 1-10 ohm·cm. Figure 3-1 shows one of the laser ablated silicon samples.

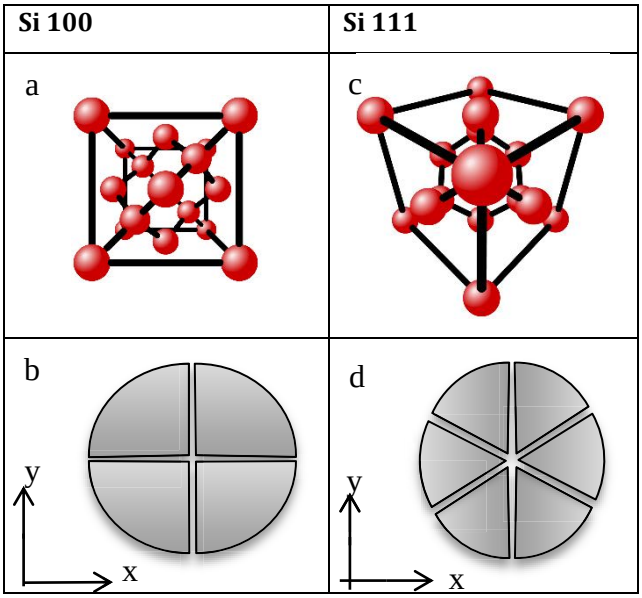

Figure 3-2 Face view of the sample used: a) of Si <100> crystal structure; b) Si <100> cleavage planes; c) Si <111> crystal structure; d) Si <111> cleavage planes

Silicon has a diamond cubic crystal structure. Two crystal orientations were used: <100> and <111>. Figure 3-2a and Figure 3-2c indicate the silicon crystalline structure from the top surface of the silicon wafer for Si <100> and Si <111>, respectively. It is significant to understand how the cleavage directions and the atomic bonds on the polished surface are correlated with the crystalline structures. For Si <100>, the in-plane bonds possess a four-fold symmetry aligned with the x and y axes; for Si <111>, the bonds possess a six-fold symmetry. The natural cleavage planes for silicon are along two directions on Si <100> tilted 90º toward each other and along three directions on Si <111> oriented 60º apart from each other (Figure 3-2b and Figure 3-2d).

3.2 Laser facilities

The large range of parameters investigated did not allow use of a single laser source, but three different laser sources were involved in the laser processing. As explained in section 2.2.2, the laser pulse duration is strongly dependent on the laser nature as well as on the gain media and on the cavity. Consequently, three different laser systems that could cover all the parameter ranges (in particular the pulse duration) considered were used in this thesis.

3.2.1 LASEA system (fs/ns pulses)

The first system that is introduced is a LASEA system (Figure 3-3), which includes two laser sources that share the beam path and the beam delivery as well as the translation system. The two lasers installed in the facilities can provide pulse in the ns regime and in femtosecond regime.

The ns laser source, shown in Figure 3-3a, is a SPI redENERGY G4 S-Type 50W fibre laser with a central wavelength of 1060 nm which can achieve a repetition rate of up to 1 MHz [116]. It is based on the master oscillation power amplifier (MOPA) architecture. This architecture consists of a seed generated by a laser diode that is subsequently amplified by an optical amplifier to increase the total output power. In this laser, the optical amplifier is represented by a dual-stage Yb GTWaveTM fibre amplifier system. The output of the amplifier fibre is equipped with a beam delivery collimator that provides a collimated beam with a diameter of 3 mm. As described in section 2.2.2, this type of laser is suitable for generating pulses with different duration, in this specific case it can provide pulse durations from a few ns to a few hundred ns. Indeed, the pulse duration of the final crater can be driven by changing the pulse of the

seed. The seed is generated by the laser diode; to change the pulse duration of the pulse emitted from the diode, it simply needs to change the duration of its electrical signal.

The ultrashort source (Figure 3-3b) is a Satsuma femtosecond laser produced by Amplitude. It is Ytterbium based and can provide an average power of 5 W at the maximum repetition rate of 2 MHz. It operates at a central wavelength of 1030 nm and provides a pulse duration of approximately 300 fs (310 fs is the pulse duration measured by the cross-correlation technique) [117]. This laser is based on a mode-locking architecture which uses the chirped pulse amplification method. A fibre as amplification for an ultrafast pulse is a novel technology that was introduced in commercial laser by Amplitude Systèmes and IMRA America, Inc it is the competitor of the classical laser that uses a crystal. The problems related to the fibre dispersion and consequently to the stretching of the pulse have been overcome, and the fibre has been introduced in commercial laser, increasing the reliability and the lifetime of the ultrashort pulse laser. In Table 3-1 the main specifications are summarised for the two lasers described above.

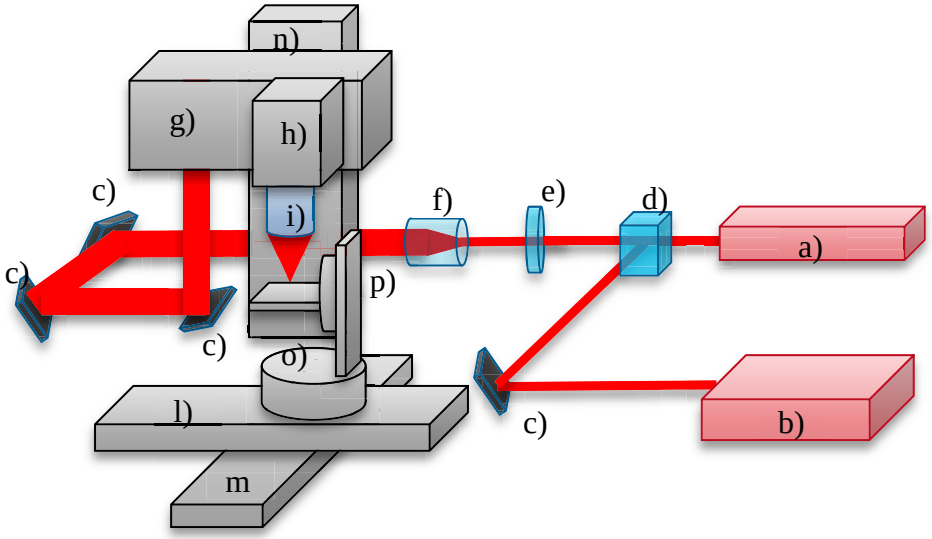

Figure 3-3 LASEA laser facility: a) SATSUMA laser; b) SPI laser; c) mirrors; d) dichroic beam splitter; e) waveplate; f) beam expander; g) z-shifter module; h) galvanometric mirrors; i) telecentric lens; l), m), and n) linear translation stages; o) and p) rotary stages.

To guide the laser beam through the selected beam trajectory, several mirrors are positioned along the path (Figure 3-3c). The mirrors used in the path are double-coated mirrors for 1064 nm, the fundamental wavelength for the Nd:YAG, and for the second harmonic at 532 nm [118]. The reflectance is greater than 99% for angles 45° and 0°. Despite the fact that the mirrors are coated for 1064 nm, the 99% level is also guaranteed at 1030 nm, so they can be used from both laser beams (Satsuma and SPI).

Table 3-1 Main specifications for SPI G4 S-type and Satsuma lasers

Parameter	SPI	Satsuma
Average output power [W]	50	5.4
Maximum pulse energy [µJ]	710	10.8
Central emission wavelength [nm]	1060	1030
Bandwidth [nm]	<10	7.5
Beam Quality M^2	<1.3	<1.3
Polarisation type	Unpolarised	Linear (S-type)

The two laser beams are coupled using a dichroic beam splitter (Figure 3-3d). The beam splitter has a cut-off frequency just beneath the emission wavelength of the SPI laser [119]. Using this cut-off frequency, it is possible to transmit the beam coming from the SPI laser and to reflect the beam coming from the Satsuma laser. Thus, after the beam splitter, the two beams are propagating on the same axis and can share the remaining beam path.

A waveplate positioned just after the beam splitter (Figure 3-3e) changes the polarisation from linear to circular and vice-versa. This element will be discussed in more depth in section 3.2.4 because it is relevant for the polarisation study.

At this point in the laser beam path is inserted a variable beam expander (Figure 3-3f). The installed beam expander can increase the beam in the range of 2X-8X times in a continuous mode, and it provides transmission efficiency greater than 97%. It is composed of a lens group. To tolerate a very high damage threshold, the lens group is made of fused silica.

By using several mirrors, the beam is guided to the z-shifter module (Figure 3-3g), which is an additional feature of the galvanometric scanners (Figure 3-3h). The z shifter module is composed of two sets of lenses that can change the divergence of the laser beam (Figure 3-4). Changing the divergence of the laser beam can modify the focal plane of the telecentric lens (Figure 3-3i). Thus, simply by moving the set of lenses, it is possible to change the focal plane and then operate at various distances from the sample to achieve complete control for 3D micromachining. The shifter module is introduced because the capability of the z axis is not always sufficient to satisfy the speed requirement of the process. The z-shifter employed is based on the principle of the moving coil; travel range is 4 mm and step width is approximately 65 nm [120].

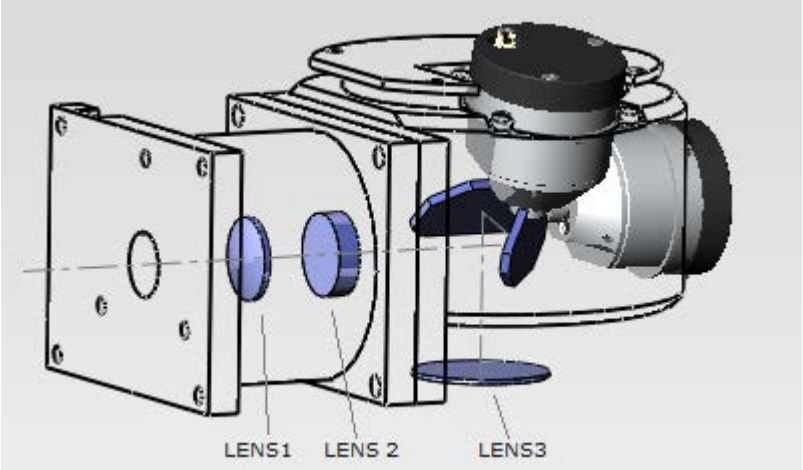

Figure 3-4 Schematic representation of the z-shifter, galvanometric mirrors, and focusing lens [120].

The galvanometric scanner mirror system is from Newson Smart NV, capable of deflecting the beam with a high dynamic (Figure 3-4). The rotary speed provided by the system is 25 rad/s, maximum angular excursion is 800 mrad, positioning repeatability is higher than 15 μrad, and tracking error is 110 μs [121].

To focus the beam, the LASEA system is equipped with two exchangeable telecentric lenses provided by QIOPTIQ (LINOS). When a beam enters the telecentric lens, which is tilted from the propagation axis, it is focused on the same focal plane and has the same size as a beam that enters on the propagation axis, but is translated. This, combined with the usage of the galvanometric scanner, allows the beam to move through a certain area while keeping the beam spot size constant. Both lenses are made from fused silica with a coating on the infrared region (1030-1060 nm) where the two lasers operate [122]. The two telecentric lenses differ in focal length—one is 160 mm and the other is 100 mm—and they can provide a beam spot size of 60 μm and 30 μm, respectively. The field of view on the focal plane is a function of both the focal length of the installed lens and the characteristics of the galvo mirror. Based on the specifications of both devices, the 3D spaces that can be covered by the 100 mm focal length lens is 35x35x6 mm, while the space covered for the 160 mm focal length lens is 60x60x10 mm.

To complete the description of the LASEA facility, a 5 axis translation system is integrated. Three linear translation stages are provided, in x (Figure 3-3l), y (Figure 3-3m), and z (Figure 3-3n) direction. The X table is a PRO165LM-0300 stage and the Y table is a PRO225LM-0300; both are based on direct drive linear technology (Aerotech). Combined on the XY translation system, they offer a ±4 μm accuracy on the

plane and a speed of 300 mm/s [123], [124] with a travel range of 300 mm. The Z table is used to move the scan head (z-shifter module, galvanometric mirrors, and telecentric lens) along the z axis, providing the proper position for the samples with different thicknesses. The Z table is a PRO115-300 (Aerotech) with the same speed and travel range as the first two but with an accuracy of ±10 μm [125]. On the XY table system are mounted two rotary stages ADRS-150 (Aerotech). Their positioning accuracy is 48 μm, and they can reach a maximum speed of 600 rpm [126]. The stages were calibrated using the High Accuracy Linear And Rotary (HALAR) Aerotech option (a method based on the interferometer calibration and error mapping), to reach the maximum accuracy and repeatability allowed from the stage itself.

3.2.2 3D Micromac System (ps)

The second laser system introduced is a microSTRUCT vario produced by 3D Micromac. This laser system was used only for the work described in section 4 because it is capable of producing pulses in the ps regime not covered by the LASEA system. Thus, fewer details are required than for the system described in section 3.2.2.

The system was built using a SuperRapid 10W, LUMERA laser source. The laser source is Nd-YAG based and can produce pulses with pulse duration in the range of picoseconds. It can provide an average power of 10 W at the maximum repetition rate of 1 MHz. It operates at a central wavelength of 1064 nm, providing pulse duration shorter than 10 ps. The single energy per pulse is up to 200 μJ and with 10 MW peak power [127]. It is made on a mode locking technology using a Nd-YAG crystal and can modulate the mode oscillating in the cavity to obtain a pulse duration close to the transform limit.

The system is equipped with an Intelliscan III (SCANLAB AG) galvo mirror system.

To focus the beam on the sample, the 3D micromac system is equipped with an F-Theta-Ronar Telecentric Lens (LINOS) [122]. This lens has a focal distance of 100 mm and can provide a spot diameter of 20 μm. The lens has a coating for three different wavelengths (355, 532, and 1064 nm). Furthermore, the laser is equipped with a harmonic generator that can generate the second and third harmonics of the laser beam. Then, to use the same lens without changing it and keep the losses low to minimise back-reflection and absorption by the lens, the laser optics is provided with three coatings, one for each laser harmonic. The system is completed by a three-axis system to move the stage.

The z shifting is provided by an Aerotech translation stage, PRO165LM. The linear motor used in this stage can move it at the maximum speed of 2 m/s with an acceleration of 3 g. The minimum resolution achievable is 10 nm, while the accuracy is ±6 µm and the bidirectional accuracy is ±0.4 µm. The total travel length that can be covered by the stage is 150 mm. These characteristics are valid with a maximum load of 45 kg [128].

3.2.3 SPI based system (µs)

The 3D Micromac SPI-based system can cover a regime that the LASEA system and the Micromac system cannot: it can operate on the microsecond regime that is the last regime investigated in Section 4. It is composed by the laser source, the galvanometric mirrors, the focusing optics, and the translation stages.

The integrated laser source is a RedPower R4, 200 W SPI. This laser can provide an average power up to 200 W, and pulse duration can be varied by a 2 to 20 µs modulation rate up to 100 kHz. This laser is based on the same architecture described for the ns laser in section 3.2.1, in which the seed is electrically generated, and a diode laser pumps the fibre amplifier system. A collimation system at the laser output has the aim to collimate the high divergence beam coming out from the fibre [129].

The galvanometric system installed in this machine is an Intelliscan 14. This scanner has an optical aperture of 14 mm with a scan angle of ±0.35 rad; when it is equipped with a 160 mm f-theta lens it has a typical marking speed (the speed which the laser beam is moved on the sample to ablate/mark) of 2 m/s and a typical positioning speed of approximately 5 m/s. The tracking error is 0.15 ms, and the angular repeatability is less than 2 µm [130].

The system can be equipped with two F-Theta-Ronar Telecentric Lenses (LINOS). Both lenses are made of fused silica with a coating on the infrared region (1030-1060 nm) where the laser operates [122]. The difference between the two lenses is the focal length—one is 160 mm and the second is 100 mm—and they produce a spot on the target of 80 µm and 40 µm, respectively. The minimum spot size achievable for this system is slightly larger than for the system described in section 3.2.1 because of the smaller collimated beam diameter of this system. Indeed, the smaller aperture of the galvo scanner system limits the expansion of the beam, but the smaller aperture enables the use of smaller mirrors and faster galvo scanners to reach a higher marking speed.

The system is provided with a manual axis translation system for the x, y, z translation of the stage. The translation system is not a commercial one; it was developed by Tekniker (the project partner that owns this laser facility).

3.2.4 Additional setup: optics and optomechanics used

In this section, the optics added to the laser facilities are described in detail. They were needed to modify or measure the laser beam characteristics involved in the study.

3.2.4.1 Waveplates

The waveplate is an optical element capable of changing the polarisation of the light. It is also known as a retarder because it works on retarding the light propagation. Waveplates are identified by the retardance amount that they can introduce. The retardance is identified based on parts of the wave period: e.g. a half waveplate introduces a retardance of π, while a quarter waveplate introduces a retardance of $\pi/2$.

Figure 3-5 Rotation mount with a half waveplate mounted

For this thesis, two waveplates were used: a quarter and a half waveplate.

The quarter waveplate, WPQ10M-1030 (Thorlabs), was a threaded mount 1 in waveplate. It was built by combining two multi-order crystalline quartz waveplates with the necessary thickness to obtain an optical path length difference of $\lambda/4$. The waveplate was also provided with an antireflection coating to obtain a reflectance lower than 0.2 [131]. Rotating the waveplate by 45º, it was possible to modify the polarisation from linear to circular and vice versa.

The half waveplate WPH10M-1030 (Thorlabs) was a threaded mount 1 in waveplate. As the one above, it was built by combining two multi-order crystalline quartz waveplates, but in this case with a thickness to obtain an optical path length difference of λ/2. It was also provided with an antireflection coating to reduce the reflectance to a value lower than 0.2 [132]. Rotating the waveplate by 45º, it was possible to modify the polarisation from parallel to perpendicular and vice versa.

The waveplates were mounted on a high-precision manual rotation mount PRM1/M (Thorlabs, Figure 3-5). This type of mounting enabled continuous rotation of the optics over 360º, and it was provided with a backlash-free micrometre adjustment [133].

3.2.4.2 Polarising beam splitter cube

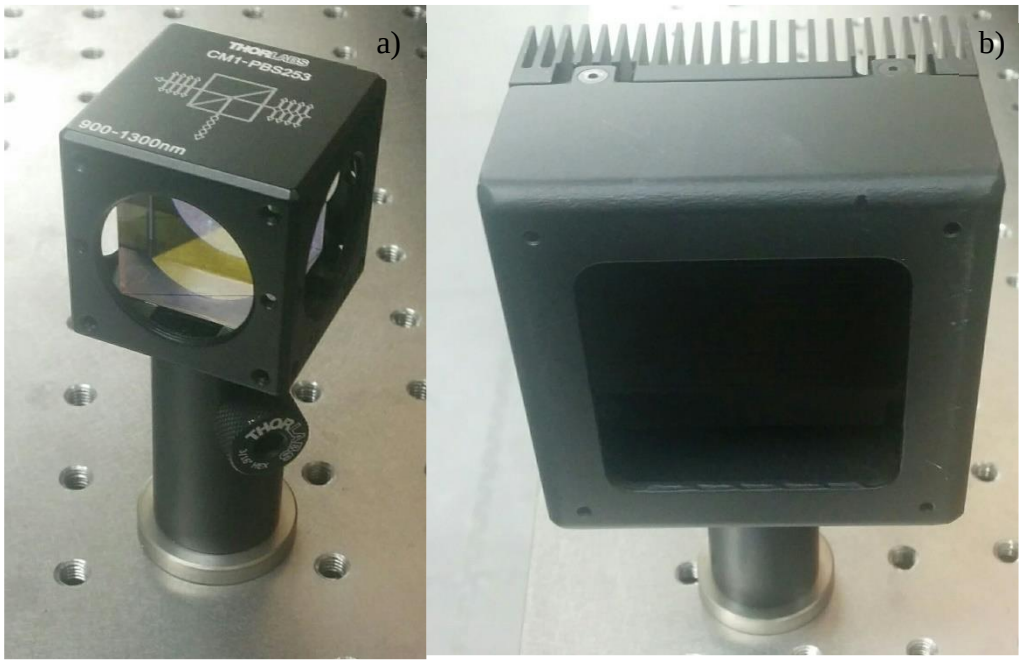

Figure 3-6 a) Polarising beam splitter, b) Beam blocker

A polarising beam splitter cube is an optic element use to split the beam based on the polarisation of the beam itself. It can work on several principles, such as the Nicol prism, the Glan–Thompson prism, the Glan–Taylor prism, and the Glan–Foucault prism. Despite the different working principles, the final effect is the same: one polarisation state is totally reflected while the other polarisation state is not reflected [134]. Thus, the reflected polarisation state can be selected because of the different propagation direction.

In this thesis, a Thorlabs Ltd polarising beam splitter cube (p.n. CCM1-PBS253/M, **Figure 3-6**a) was used. It has a dielectric coating along the diagonal interface, the interface between the two right-angle prisms that make up the cube. This coating

reflected s-polarized light and transmitted p-polarized light [135]. The reason to use the polarising cube is to quantify the amount of polarisation introduced by the waveplates mentioned above.

A beam blocker is an element that is introduced in the beam path to block a high-energy laser beam. It avoids undesired back-reflection or interference between beams. The employed beam blocker Thorlabs Ltd (p.n. LB2/M Thorlabs, **Figure 3-6**b) is capable of absorbing CW and pulsed laser beams over the 1 to 12 µm wavelength range with maximum average power of 80 W (CW) or a maximum energy density of 25 J/cm^2 (pulsed) [136]. While one of the beam paths was blocked by the beam dumper, the other was measured by the power meter described in section 3.3.1.

3.2.4.3 Energy beam shaper

As described in section 2.3.2, several devices can be used to generate a non-standard energy beam shape. In this thesis, two devices based on diffractive optics were used. Both energy beam shapers were provided by Holo/Or Ltd. The first one was a top hat energy beam shaper (ST-230-I-Y-A) capable of providing a round flat-top energy beam distribution once the laser energy beam was focused with external optics. The shaper was made of fused silica with a diameter of 20 mm and had a clear aperture of 18 mm and thickness of 3 mm. The input requirements to achieve a round flat-top distribution were i) A/R coating wavelength, 1064 nm; ii) beam diameter, 7 mm; and iii) beam mode, single mode TEM00 with M^2<1.5. The output on the focal plane was based on the focusing optics integrated in the system.

The second system was a top hat energy beam shaper and lenses (ST-203-I-Y-A) capable of providing a square flat-top energy beam distribution on the focal plane. The first Diffractive optical elements (DOE) was inscribed in a window, while the second was inscribed in a focusing optics. In this last case, it was possible to focus the spot without additional optics. It was made of fused silica with a diameter of 25.4 mm, a clear aperture of 20 mm, and a central thickness of 5.3 mm. The inputs were optimised for the following values: i) A/R coating wavelength, 1064 nm; ii) beam diameter, 6 mm; and iii) beam mode, single mode TEM00 with M^2<1.5. The corresponding outputs on the focal plane were i) working distance, 52mm; ii) spot size ($1/e^2$) 50x50 µm; and iii) transfer region, 4 µm.

3.3 Laser beam characterisation instruments

The laser facilities used in this thesis were provided with an internal power meter capable of measuring the power from the exit of the laser. However, the presence of several optics on the laser beam path reduced the power delivered to the sample by back reflection. Thus, a measurement at the end of the beam path was required to know the exact energy amount that was hitting the sample. Moreover, the introduction of the additional optics described in section 3.2.4 can change the total amount of power delivered, so measurement of power with an external device is essential. Furthermore, the measurement of the energy beam energy distribution is important to identify the exact focal position of the diffractive optics. In fact, they have a short depth of focus and are quite sensitive to translation on the z position. Finally, analysis of the energy beam shape is needed as reference when the craters are generated by non-standard energy beam distribution.

3.3.1 Power meter

A laser power meter was used to measure the power reaching the sample. The power reaching the sample is typically less than the power provided by the laser because of the losses introduced by various optics placed in the beam path. Thus, for an accurate measurement of the power, an additional measurement is required in the vicinity of the sample. The power meter consisted of a thermal head UP19K-50L-W5-D0 (Gentec, Figure 3-7) capable of measuring up to 50 W or 100 kW/cm^2 with a 17 mm diameter sensor [137]. The meter was provided with a large heat sink to increase the thermal dissipation. The head was connected to a UNO monitor (Gentec, Figure 3-7) equipped with a 24 bit A/D converter for high-resolution measurements [138].

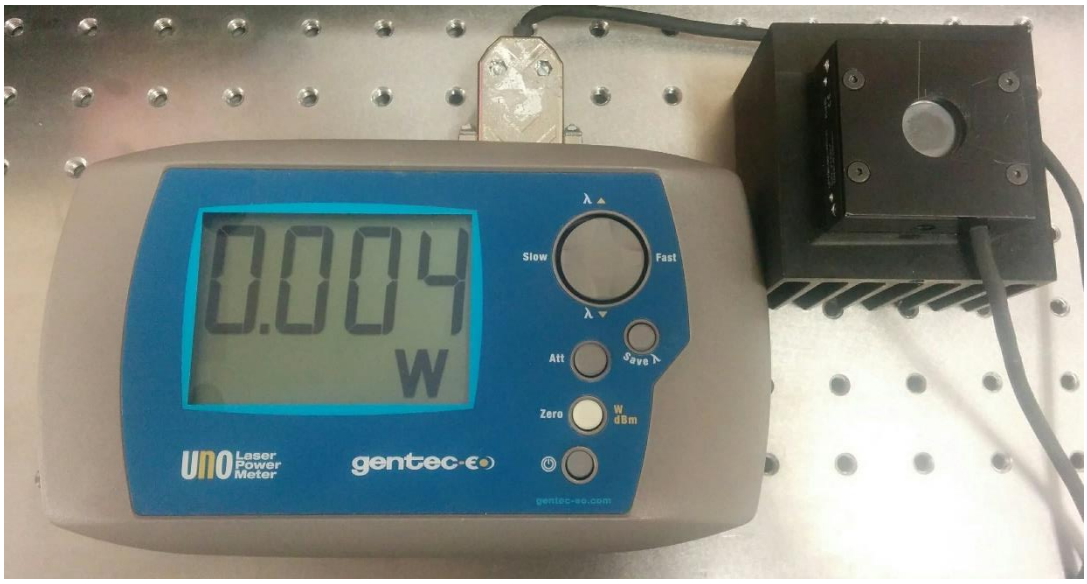

Figure 3-7 Gentec power meter: on the left, the UNO monitor; on the right, the head UP19K-50L-W5-D0

3.3.2 Energy beam profilers

There were two devices used to characterise the energy beam shape. The first device was a CinCam CMOS Series (CINOGY Figure 3-8a), a traditional energy beam profiler based on a CMOS camera. It was equipped with a 1/1.8 in 2 MP sensor, operating in the spectral range between 400 nm and 1320 nm. Each pixel had a size of 4.5x4.5 μm. The bit depth was 8 bits with a dynamic of 62 dB. This type of beam profiler provides the real energy beam distribution of the laser beam. Each pixel collected a certain amount of energy, and the energy beam profile was built for the entire beam area. The limit of this device was the pixel size, which was a few micrometres [139]. Then, for laser spots smaller than a few tens of micrometres, the number of pixel involved in the measurement is not sufficient for a correct analysis of the laser beam energy distribution.

The second device was a scanning slit-beam profiler. The device used was a Beam'R2 (DataRay Inc., Figure 3-8b), which employed a silicon detector that could measure a signal from 190 nm to 1150 nm with a resolution of 0.1 μm and an accuracy of 0.5 μm [140]. It was based on a slit that was translated in front of the sensor. The sensor acquired the profiles on each axis but missed the information in between. Thus, the measurement was accurate for the beam width, divergence, and other related parameters compared to the first type, but it could not highlight hot spots or other beam distribution discrepancies [139].

a) b)

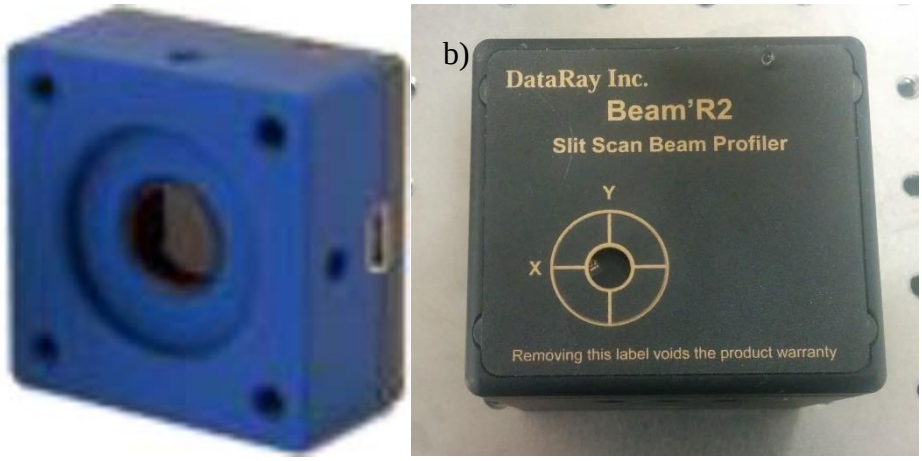

Figure 3-8 For the two-beam profile analysis, a) Camera-based and b) Slit-based devices were used

3.4 Laser patterning methodology

This section describes the methodology used to pattern the silicon sample. This thesis does not require the patterning of 3D shapes but only single crater ablation; thus, it does not require high-level patterning strategies. The patterning methodology that was employed is described in the following subsections.

3.4.1 Laser sample alignment

One of the most important steps before the laser material processing was the alignment of the sample. For a single crater ablation, the x-y alignment was not a critical point. However, as described in section 3.2, the field of view of the scanner was limited to a few centimetres depending on the focusing optics and on the galvo scanner used. The silicon wafers were 3” in diameter; to move around the samples, the use of the linear stage was necessary. To optimise the sample area used, and to be repeatable in more than one sample, a reference point was chosen in the sample itself. The reference is highlighted in Figure 3-9 and is the “corner” in the bottom left. For example, the sample in Figure 3-9 was organised in 10 main groups, and each main group contained 18 subgroups. Each subgroup was identified by a tag containing the information about the parameters evaluated in that experiment. For each subgroup a certain number of craters with the same parameters were ablated to ensure a certain reproducibility of the results.

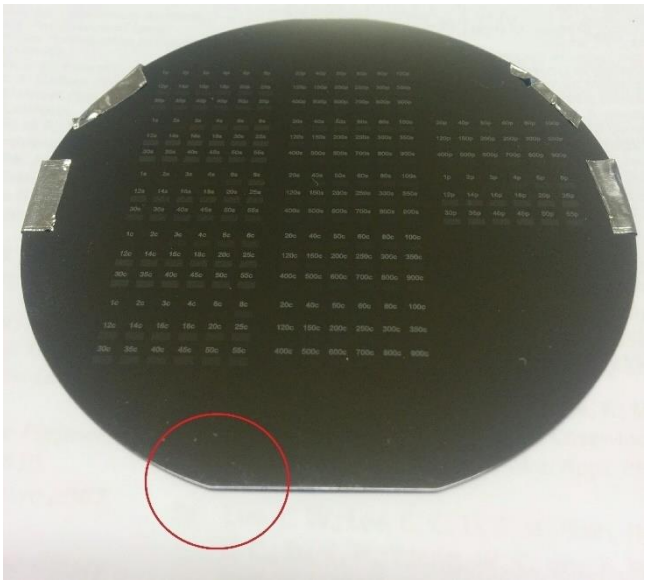

Figure 3-9 Example of a silicon sample pattern. The red circle indicates the corner chosen as a reference point

A fundamental role in the alignment was the spot along the z axis, because at the focus position, the spot size reaches its minimum. To identify this position, a line of single-pulse, single-crater ablation was made at a fixed energy amount, moving the z translation system a fixed step. The resulting matrix represented the interaction between the material along the z axis and the laser beam with fixed laser beam parameters. Repeating this procedure for decreasing laser fluence, it was possible to identify the z range where the spot size reached the smallest values. For those z values, the fluence overcame the single ablation threshold, and craters were generated; for the z values outside of that range, there was no ablation, and no craters were appearing on the sample.

For example, for the laser system described in section 3.2.1, the Rayleigh length (the length for which the spot size radius increases by a $\sqrt{2}$ factor) was between 0.5 and 1 mm. Then, once the middle value of this z range was identified, it was easy to reposition the sample due to the high accuracy of the translation stages (section 3.2).

For the beam shaper element, the expected shape was not in the Rayleigh length, but it was in a position closer to the focusing lens. It is noted that the z range where the expected shape was obtained was very short (tens of micrometres), and a more accurate positioning was required. In particular, it was required that the sample be normal on the x-y plane to the incident laser beam. To verify this condition, a confocal camera installed on the galvo head was used to measure the distance between the laser head and the sample. Then, the rotating axes were used to compensate any tilting of the sample from the normal plane to the laser beam, identified by the confocal camera.

3.4.2 Laser sample processing

Now that the alignment and the positioning of the sample have been described, the patterning process will be discussed. Each laser facility provided a CAD (computer-aided design) interface to command the galvo scanner.

The interface gave the user two possibilities: to draw simple geometries or to import more complex geometries from the most common CAD software. Once the drawing was uploaded in the software interface, it was possible to set the required laser parameters. Some laser parameters such as pulse duration (in nanosecond and microsecond regimes), power, and repetition rate could be set using the software interface. Moreover, the interface allowed the process parameter to be set by its relation

to the galvanometric scanner (e.g. marking speed and jump speed) and to the linear stage (speed and acceleration).

The requirements of this thesis were to obtain a single crater produced by a single laser pulse or multiple pulses. To meet these requirements, two main strategies were applied:

1. Use a "vectorial mode" and change the speed accordingly with the repetition rate to obtain a single crater spot
2. Use the "picture mode" mode where the software interface considered the drawing made by several pixels and each single pixel corresponded to a single crater.

Two examples are now introduced to better clarify the two operation modes. To generate single craters, the typical required pattern is shown in Figure 3-10a, where single craters are positioned one after the other at a certain distance d_c and parallel to the reference side.

To obtain this pattern in the "vectorial mode," a line from point 1 to point 2 was drawn using the galvo interface. This line corresponded to a continuous movement (considering acceleration and deceleration) of the galvo motors, moving the laser beam spot from point 1 to point 2. To obtain the single crater, the laser repetition rate (R_r) had to be set together with the galvo speed (g_v), based on the d_c desired value following the relation $d_c = g_v/R_r$.

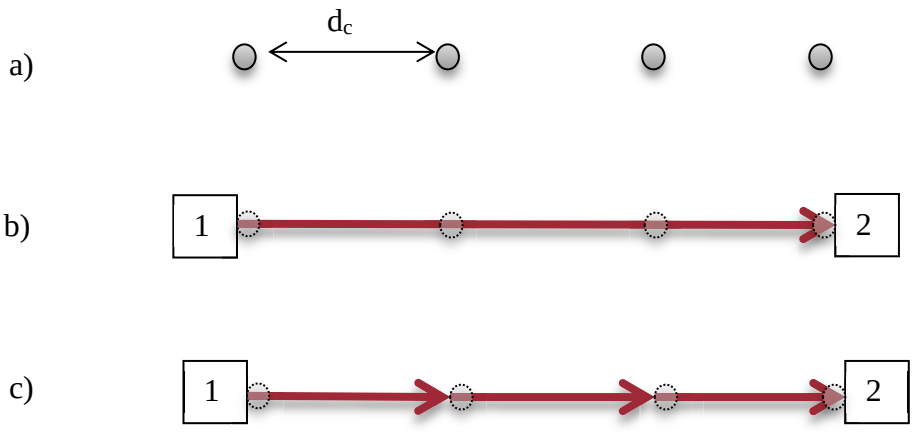

Figure 3-10 Crater patterning strategies: a) Description of the single crater position, b) Vectorial mode process, and c) Image mode process

To obtain the single crater using the "picture mode," the line was drawn as for the vectorial mode, but in this case, the line was not considered as a trajectory going from point 1 to point 2, but it was considered as a finite sum of pixels between point 1 and point 2. Then, galvanometric scanners were moving the laser beam spot from one pixel

to another pixel, in a step-by-step motion. The value d_c, which was equal to the distance between pixels, was an input parameter of the interface software.

The main difference between the two modes was in the case of multiple pulse regimes (more than one laser pulse in the same position). Indeed, in the case of the "vectorial mode," to generate a crater by multiple pulses, it was necessary to repeat the line a number of times equal to the number of pulses required. The time between one pulse and the next pulse in the same position was the time that the galvo scanners needed to complete a line and then jump back.

For the "image mode," it was possible to make more than one pulse without moving the galvo head, keeping the laser on the crater position. The time between one pulse and the next was equal to the inverse of the repetition rate. Setting a time multiple of the inverse of the repetition rate allowed a specific number of pulses to be delivered in each spot. This time was set as the time that the laser spot was staying in the same pixel.

For the ns laser source, the vectorial mode was used because in those cases the scanner motion and the pulse timing were synchronised, and when repeating the line, the pulses were delivered exactly in the same position. For the femtosecond laser source, because of the non-synchronisation between the galvo and the pulse timing, when using the "vectorial mode," the craters were not overlapped. For this reason, the "image mode" was necessary to produce a multiple-pulse crater, which was essential for the multiple-pulse experiments.

3.5 Analysis facilities

The analysis facilities that were used had the scope to obtain information about the morphology of the craters generated by the laser material ablation. The facilities can be divided into two main typologies: quantitative and qualitative. It is defined quantitative facilities to be those capable of giving a numerical 3D description of the crater. We defined qualitative facilities as the facilities that do not give a numerical 3D description of the crater but can provide a crater image. However, in Section 6 the possibility to obtain a quantitative analysis of some crater characteristics from a qualitative analysis facility is also described.

3.5.1 Quantitative analysis: 3D Alicona confocal microscope, Bruker GT-Contour white light microscope interferometer

The 3D Alicona confocal microscope (Figure 3-11) is a confocal microscope based on the focus variation technique. This technique can provide topographical and colour information from the variation of focus by combining the small depth of focus of an optical system with a high-resolution vertical scanning process [141]. The system in this thesis was equipped with five different objectives—x5, x10, x20, x50 and x100—that provided a lateral maximum resolution of 3.52 µm, 1.76 µm, 0.88 µm, 0.64 µm, and 0.44 µm and a maximum vertical resolution of 0.41 µm, 0.1 µm, 0.05 µm, 0.02 µm, and 0.01 µm, respectively [142]. However, it was possible to lower the resolution to decrease the data acquisition time. To position the sample under the objective and to focus it accordingly with the objective focal length, the system was provided with three mechanical stages in x, y, and z with a travel range of 100 mm [142].

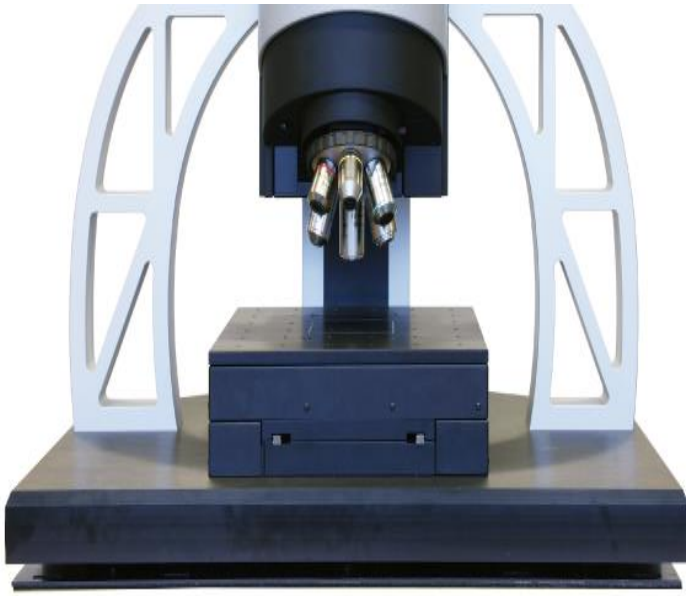

Figure 3-11 Alicona 3D confocal microscope

The Bruker GT-Contour (Figure 3-12) was a white light microscope based on the interference technique. It was based on the superimposition principle that happens when two electromagnetic waves are combined and their wavefronts change. It is known that when two different laser beams are combined they can interfere each other, creating a new pattern that depends on the phase of the electromagnetic wave. Thus, if the pattern is produced by a beam that was reflected by a surface, it is possible to identify the surface morphology by analysing the interference pattern.

The system was provided with three mechanical translation axes, x, y, and z, with a travel range of 150 mm, 150 mm, and 100 mm, respectively. It had three objectives—2.5x, 10x, and 20x—and three zoom lenses—0.55x, 1.5x, and 2x—to improve the objective imaging. The maximum achievable lateral resolution was 0.32 µm, and the maximum vertical resolution was 0.05 nm. Vision64 Analysis Software allowed the collection of 3D data by the Contour –GT [143] .

The two devices described above were capable of collecting the same type of data (3D morphology), but the preliminary tests showed that the two devices were suitable for two different silicon surface morphologies. Shallow and smooth morphologies limited the capability of the Alicona microscope to focus on different planes. Alternatively, craters with features with a periodicity close to the laser spectrum employed can create some artefacts on the data obtained with the Countour-GT; in this case, the Alicona microscope was more effective. For these reasons, the analysis of the large number of craters in this thesis required two different devices.

Figure 3-12 Bruker GT-Contour

3.5.2 Qualitative analysis: SEM

The SEM used to perform the qualitative analysis on the sample was an environmental scanning electron microscope, Philips XL30 ESEM FEG (Figure 3-13). The main advantage of this ESEM compared to a classical SEM is that any material can be

examined in its natural state in a gaseous environment. It is based on a Schottky-based gun using a point-source cathode of tungsten. The minimum magnification is 20x, resulting in a field of view of approximately 2 mm x 2 mm, while the resolution at 30 kV is 3.5 nm, but operation at low voltage (around 500 V) is possible. Two sensors, one for the secondary electrons and one for the back-scattered electrons, are available. The back scattered electron detector is usually applied when more than one element is analysed, indeed using it the elements with greater atomic mass appear brighter in the image. Considering that a single element (Silicon) will be study in this thesis, the back scattered electron detector will not be used.

Figure 3-13 ESEM Philips XL30 ESEM FEG

This instrument is fitted with an Oxford Inca 300 EDS system. In addition, it has a PolarPrep 2000 cryo-stage system that allows observation of rapidly frozen hydrated samples.

4 LASER PULSE DURATION EFFECTS ON THE CRATER SHAPE

The pulse duration is the most relevant laser parameter to consider for laser micromachining because of its role in driving thermal and non-thermal mechanisms during the laser ablation process. Identification of the thermal and non-thermal effects resulting from the laser process is time consuming because of the slow facilities that are involved in the analysis (e.g. SEM, TEM, AFM).

This chapter reports a novel method to identify the thermal and non-thermal effects based on analysis of the crater shape and considering the laser pulse duration. Starting from the models proposed by the literature, an iso-thermal function was developed, and an iso-energetic function was defined to approximate the crater of the single-pulse laser ablation. Using these two functions, a quantitative factor was defined to identify the thermal effects present on the target. A systematic study from the femtosecond to the microsecond regime was conducted. It was demonstrated that the quantitative factor defined can be used to evaluate the presence of thermal effects. Analysis of the quantitative factor confirms the fundamental role of the pulse duration on driving the ablation mechanism during laser ablation. Moreover, the analysis highlights the contribution of fluence on the crater shape for the time regime longer than femtosecond

and shorter than microsecond. Parallel with the novel method proposed, a classical SEM analysis was conducted to confirm the behaviour revealed by the quantitative factor.

4.1 From the model to the quality factor

As illustrated in Section 2.2, because of the mechanisms involved in laser ablation, the process can be divided into thermal and non-thermal processes depending on the laser pulse duration. Based on this consideration, two different functions that can estimate the thermal impact on the crater shape produced by the material removal, were searched. The goal was to identify two functions that can be written in the form of z=f(x,y). The thermal function is based on the isothermal curves and considers diffusion effects. The second function is based on the iso-energetic curves and neglects the effect of thermal diffusion; it considers only the energy distribution inside the sample.

4.1.1 General solution to the heat diffusion problem

Before introducing the solution for a specific problem, it is described the general solutions for the heat problem.

$$\begin{cases} \boldsymbol{u_t - \Delta u = s(r,t)} \\ \boldsymbol{u|_{t=0} = u_0} \end{cases} \boldsymbol{r \in R^3, t > 0} \qquad \textbf{(4.1)}$$

where u is the general solution for the heat problem and s(r,t) indicates a time and space dependent source. Applying the Fourier transform to Eq. 4.1, the following system is obtained:

$$\begin{cases} \boldsymbol{\hat{u}_t + |k|^2 \hat{u} = \hat{s}(k,t)} \\ \boldsymbol{\hat{u}|_{t=o} = \hat{u}_0(k)} \end{cases} \boldsymbol{k \in R^3, t > 0} \qquad \textbf{(4.2)}$$

The solutions for the ordinary differential equation (ODE) system written in Eq. 4.2 are the following:

$$\boldsymbol{\hat{u}(k,t) = e^{-|k|^2 t} \hat{u}_0(k) + \int_0^t e^{-|k|^2 (t-\tau)} \hat{s}(k,\tau)\, d\tau} \qquad \textbf{(4.3)}$$

To find the solution for the original ODE, the inverse Fourier transform is applied:

$$\boldsymbol{u(x,t) = \frac{1}{(4\pi t)^{\frac{3}{2}}} e^{-\frac{|r|^2}{4t}} * u_0(r) + \int_0^t \frac{1}{(4\pi(t-\tau))^{\frac{3}{2}}} e^{-\frac{|r|^2}{4(t-\tau)}} * S(r,\tau)\, d\tau} \qquad \textbf{(4.4)}$$

It results in the following solutions:

$$\boldsymbol{u(x,t) = \frac{1}{(4\pi t)^{\frac{3}{2}}} \int_{R^3} e^{-\frac{|r-r'|^2}{4t}} v_0(r')\, dr' + \int_0^t \int_{R^3} \frac{1}{(4\pi(t-t'))^{\frac{3}{2}}} e^{-\frac{|x-y|^2}{4(t-t')}} f(r,t) dr'\, dt'} \qquad \textbf{(4.5)}$$

From Eq. 4.5, the following function can be isolated:

$$\boldsymbol{k(r,t)} = \frac{\mathbf{1}}{(\mathbf{4\pi t})^{\frac{3}{2}}} \boldsymbol{e}^{-\frac{|r|^2}{4t}} \tag{4.6}$$

Equation 4.6, which is called the "heat kernel," represents the general solution for the heat diffusion equation. When $u|_{t=0} = 0$, by the substitution the heat kernel into Eq. 4.5 and it is obtained

$$\boldsymbol{u(x,t)} = \int_0^t \int_{R^3} \boldsymbol{k(r-r',t-t')s(r',t')dr'\,dt'} \tag{4.7}$$

Two characteristics of the source are introduced: i) the source is time dependent, but its time duration is much shorter compared to the time required for the diffusion process; ii) the source is spatially dependent, but the source area is much smaller compared to the area affected by the diffusion effect. Under this hypothesis, the point source can be written as follows:

$$\boldsymbol{s(r,t)} = \boldsymbol{\delta(r-\xi,t-t'')} \tag{4.8}$$

Then substituting Eq. 4.8 in Eq. 4.7 and applying the Dirac delta function properties, it is obtained:

$$\boldsymbol{u(r,t)} = \boldsymbol{k(r-\xi,t-t'')} = \frac{\mathbf{1}}{(\mathbf{4\pi(t-t'')})^{\frac{3}{2}}} \boldsymbol{e}^{-\frac{|r-\xi|^2}{4(t-t'')}} \tag{4.9}$$

So, under the conditions described above, and with $\xi = 0$ and $t'' = 0$, finally the form of the heat kernel can be written as it is commonly known:

$$\boldsymbol{u(r,t)} = \frac{\mathbf{1}}{(\mathbf{4\pi t})^{\frac{3}{2}}} \boldsymbol{e}^{-\frac{r^2}{4t}}, \boldsymbol{r \epsilon R^3} \tag{4.10}$$

In Cartesian coordinates, $r^2 \rightarrow x^2 + y^2 + z^2$, and

$$\boldsymbol{u(x,y,z,t)} = \frac{\mathbf{1}}{(\mathbf{4\pi t})^{\frac{3}{2}}} \boldsymbol{e}^{-\frac{x^2+y^2+z^2}{4t}}, \qquad \boldsymbol{x,y,z \epsilon R} \tag{4.11}$$

4.1.2 Solution for the thermal PDE model on silicon

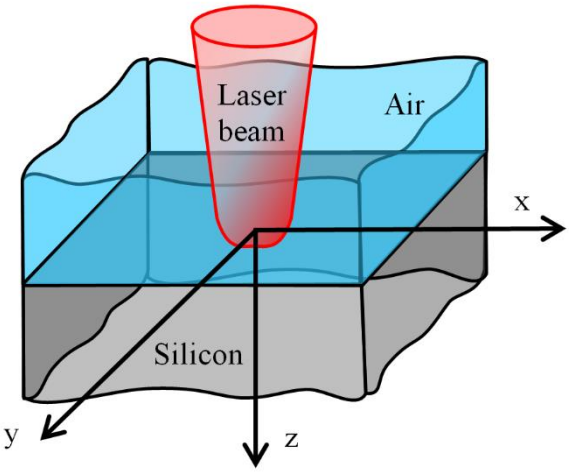

Figure 4-1 Schematic representation of the laser beam, silicon sample, and coordinates of axes

It is now set the condition for our specific case of laser material interaction. It is considered that the laser hits the silicon sample at 90° incidence angle, and the coordinate system are set as described in Figure 4-1. The silicon sample and the air are treated as the semi-infinite media. Taking into account the thermal equation described by the Fourier Law in Eq. 2.18, it is possible to apply the partial differential equation (PDE) system that is commonly used to described the laser ablation thermal model [144], [145] and to obtain the following equation system:

$$\begin{cases} v_t - d^2 \Delta v = s(x,y,z,t); \\ v(x,y,z,t=0) = 0; \\ v_z(x,y,z=0,t) = 0. \end{cases} \qquad (4.12)$$

where $0 \leq z \leq +\infty$, $-\infty \leq x,y \leq +\infty$, and $0 \leq t \leq +\infty$, d^2 is thermal diffusivity and s(x,y,z,t) is the time-dependent source represented in Cartesian coordinates. The condition of nulling of the normal derivative on the surface comes from the fact that the thermal conductivity of silicon is considerably higher than the heat transfer coefficient from silicon to air. Starting from the solution discussed in the previous paragraph, which represents a solution for the infinite media, the solution for the semi-infinite media can be built, considering the condition $v_z(x,y,z=0,t) = 0$:

$$\Phi(\vec{r},\vec{r}',t,t') = \frac{1}{\left(4\pi a^2 (t-t')\right)^{3/2}} \left(e^{-\frac{(x-x')^2+(y-y')^2+(z-z')^2}{4a^2(t-t')}} + e^{-\frac{(x+x')^2+(y-y')^2+(z-z')^2}{4a^2(t-t')}} \right) \qquad (4.13)$$

where the point source is placed at an arbitrary point $r' = (x', y', z')$ at the time t'.
The solution for the ODE can then be written as follows:

$$v(\vec{r}, t) = \int_0^t \int_{\mathbb{R}^3} \Phi(\vec{r}, \vec{r}', t, t') f(\vec{r}', t') d\vec{r}' dt' \qquad (4.14)$$

where Φ is obtained by placing the point source symmetrical to the boundary.
If the point source is in $\vec{r} = (x = -\varepsilon, 0, 0)$, the source can be written as $s(\vec{r}, t) = \delta(x + x', y', z', t)$, and the solution results:

$$v(x, y, z, t) = \frac{1}{(4\pi a^2 t)^{\frac{3}{2}}} e^{-\frac{(x+\varepsilon)^2+y^2+z^2}{4a^2 t}} + \frac{1}{(4\pi a^2 t)^{3/2}} e^{-\frac{(x-\varepsilon)^2+y^2+z^2}{4a^2 t}} \qquad (4.15)$$

When ε→0, the solution is

$$v(x, y, z, t) = \frac{2}{(4\pi a^2 t)^{\frac{3}{2}}} e^{-\frac{x^2+y^2+z^2}{4a^2 t}} \qquad (4.16)$$

It is interesting to note that the semi-infinite space differs from the infinite space solution only for the multiplier 2.
A source is now introduced, that is not a point but takes into account the laser energy beam distribution. Taking a source with a Gaussian spatial energy beam distribution

$$f(\vec{r}, \tau) = \frac{Q}{2\sigma^2} e^{-\frac{x'^2+y'^2}{2\sigma^2}} \delta(z' + \varepsilon) \delta(\tau) \qquad (4.17)$$

where ε is a generic distance from the boundary. Substituting the source into Eq. (4.14), considering only the part that is dependent on y' and integrating by y', it is obtained:

$$\int_{-\infty}^{+\infty} \frac{1}{(4\pi a^2 t)^{\frac{1}{2}}} e^{-\frac{(y-y')}{4a^2 t}} \frac{1}{2\sigma^2} e^{-\frac{y'^2}{2\sigma^2}} dy' = \frac{1}{\sqrt{2\sigma^2 + 4a^2 t}} e^{-\frac{y^2}{2(\sigma^2+2a^2 t)}} \qquad (4.18)$$

The same methods can be applied for the x direction. Then it is possible to combine the two integrals to obtain

$$v(x, y, z, t) = \frac{Q}{2\sigma^2 + 4a^2 t} e^{-\frac{x^2+y^2}{2\sigma^2+4a^2 t}} \frac{1}{\sqrt{2\sigma^2 + 4a^2 t}} \left(e^{-\frac{(z+\varepsilon)^2}{4a^2 t}} + e^{-\frac{(z-\varepsilon)^2}{4a^2 t}} \right) \qquad (4.19)$$

Thus, when ε→0

$$v(x, y, z, t) = \frac{Q}{2\sigma^2 + 4a^2 t} e^{-\frac{x^2+y^2}{2\sigma^2+4a^2 t}} \frac{1}{\sqrt{2\sigma^2 + 4a^2 t}} e^{-\frac{z^2}{4a^2 t}} \qquad (4.20)$$

Introducing the dependence to the electromagnetic propagation defined by the Beer-Lambert la, the solution of the integral described in Eq. (4.21) is:

$$\boldsymbol{I = \int_0^{\infty} e^{-\frac{(z-z')^2}{4a^2(t-\tau)}} e^{-kz'} dz'} \tag{4.21}$$

where k is the electromagnetic penetration coefficient. For simplicity, the notation $4a^2(t-\tau) = L^2$ will be used to solve the integral:

$$\boldsymbol{-\frac{(z-z')^2}{L^2} - kx' = \cdots = -\frac{1}{L^2}\left(z' + \left(z - \frac{L^2k}{2}\right)\right)^2 - kz + \frac{L^2k^2}{4}} \tag{4.22}$$

Next, substituting the integral in Eq. (4.21) it is obtained:

$$\boldsymbol{\int_0^{\infty} e^{-\frac{\left(z' + \left(z - \frac{L^2t}{2}\right)\right)}{L^2}} e^{-kz + \frac{L^2k^2}{4}} dz'} \tag{4.23}$$

Substituting $\tilde{z} = z' + \left(z - \frac{L^2k}{2}\right), dz' = d\tilde{z}, z' = 0 \rightarrow \tilde{z} = z - \frac{L^2k}{2}$ it is obtained:

$$\boldsymbol{\left(L\int_{\frac{z}{T}-\frac{Lk}{2}}^{\infty} e^{-z'}\, dz'\right) e^{-kz+\frac{L^2k^2}{4}} dz' = L\frac{\sqrt{\pi}}{2} erfc\left(\frac{x}{L} - \frac{Lk}{2}\right) e^{-kz+\frac{L^2k^2}{4}}} \tag{4.24}$$

where *erfc* = complementary error function. Thus, Eq. (4.21) can be written in the following way:

$$\boldsymbol{I = \sqrt{\pi a^2(t-\tau)} erfc\left(\frac{z}{\sqrt{4a^2(t-\tau)}} - k\sqrt{a^2(t-\tau)}\right) e^{-kz + a^2k^2(t-\tau)}} \tag{4.25}$$

In the same way, it is possible to obtain the second part of the integral:

$$\boldsymbol{\tilde{I} = \int_0^{\infty} e^{-\frac{(z+z')^2}{4a^2(t-\tau)}} e^{-kz'} dz' = \cdots = L\frac{\sqrt{\pi}}{2} erfc\left(\frac{z}{T} + \frac{Lk}{2}\right) e^{-kz+\frac{L^2k^2}{4}}} \tag{4.26}$$

Using the integrals in Eq. (4.21) and Eq. (4.26) to describe the general solution in the case of two semi-infinite media with a Gaussian pulse described by the following function:

$$\boldsymbol{s(x,y,z,\tau) = \frac{Q}{2\sigma^2} e^{-\frac{x^2+y^2}{2\sigma^2} - kz} \delta(\tau)} \tag{4.27}$$

The solution of the PDE problem is

$$v(x,y,z,t) = \frac{Q}{2\sigma^2 + 4a^2 t}\left(erfc\left(\frac{z}{2a\sqrt{t}} - ka\sqrt{t}\right) + erfc\left(\frac{z}{2a\sqrt{t}} + ka\sqrt{t}\right)\right)e^{-kz+a^2k^2t-\frac{x^2+y^2}{2\sigma^2+4a^2t}} \quad (4.28)$$

4.1.3 ERFC asymptotic expansion

The solution in Eq. (4.28) contains the complementary error function, so it is impossible to extract a function in the form of z=f(u,x,y,t). However, it is possible to substitute the erfc with its asymptotic expansion as follows:

$$erfc(x) = \frac{e^{-x^2}}{x\sqrt{\pi}} \quad (4.29)$$

To substitute the erfc with its asymptotic expansion, the condition arg(erfc)>>0 must be verified. In the specific case, the condition that must be verified is $erfc\left(\frac{z}{2a\sqrt{t}} - ka\sqrt{t}\right), erfc\left(\frac{z}{2a\sqrt{t}} + ka\sqrt{t}\right) \gg 0$; consequently, when the condition $erfc\left(\frac{z}{2a\sqrt{t}} - ka\sqrt{t}\right) \gg 0$ is verified, the main condition is also verified.

Table 4-1 Properties of silicon that are used to verify the asymptotic condition: a^2 is the thermal diffusivity[146], k is the penetration depth coefficient for temperature close to the boiling point [147], and z is the maximum depth measured from the experimental data.

	Silicon
a^2 [cm^2/s]	0.88
k [μm^{-1}]	1 (high temperature)
z[μm]	<7 (measured depth of the crater)

The condition it was verified with the values reported in Table 4-1. The reported value for the penetration coefficient is related to the value measured at high temperature. The depth of crater (z) was experimentally identified by measuring the deepest crater to introduce the worst-case scenario to verify the asymptotic condition. Applying the

discussed parameters, it is found that the asymptotic expansion can be applied to pulses longer than 220 ns with an error of 4%.

So applying the asymptotic expansion, the square argument of the erfc becomes $-\left(ka\sqrt{t}-\frac{z}{2a\sqrt{t}}\right)^2=-k^2a^2t+kz-\frac{z^2}{4a^2t}$ for the first component and

$-\left(ka\sqrt{t}+\frac{z}{2a\sqrt{t}}\right)^2=-k^2a^2t-kz-\frac{z^2}{4a^2t}$ for the second component.

So, the solution can be written as follows:

$$\boldsymbol{v(x,y,z,t)=\frac{Q}{2\sigma^2+4a^2t}\frac{k}{2}e^{-\frac{x^2+y^2}{2\sigma^2+4a^2t}}\frac{1}{\sqrt{\pi}}\left(\frac{e^{-\frac{z^2}{4a^2t}}}{ka\sqrt{t}-\frac{z}{2a\sqrt{t}}}+\frac{e^{-\frac{z^2}{4a^2t}}}{ka\sqrt{t}+\frac{z}{2a\sqrt{t}}}\right)} \qquad \textit{(4.30)}$$

That can be simplified, and we obtain

$$\boldsymbol{v(x,y,z,t)=\frac{Q}{2\sigma^2+4a^2t}\frac{k}{2}e^{-\frac{x^2+y^2}{2\sigma^2+4a^2t}}\frac{1}{\sqrt{\pi}}e^{-\frac{z^2}{4a^2t}}\frac{2ka\sqrt{t}}{k^2a^2t+\frac{z^2}{4a^2t}}} \qquad \textit{(4.31)}$$

Thus, it can be written:

$$\boldsymbol{v(x,y,z,t)=\frac{Q}{2\sigma^2+4a^2t}\frac{k}{2}e^{-\frac{x^2+y^2}{2\sigma^2+4a^2t}}\frac{1}{\sqrt{\pi a^2t}}e^{-\frac{z^2}{4a^2t}}} \qquad \textit{(4.32)}$$

4.1.4 Thermal and non-thermal functions

Equation (4.32) is the solution for the PDE system described in Eq. (4.12), on the hypothesis of pulses longer than 220 ns. This hypothesis allows the use of asymptotic expansion and thus the solution to be obtained in the form of Eq. (4.32), which is without any integral operators. It follows that keeping the temperature value constant, it can be written

$$\boldsymbol{T=\frac{Q}{2\sigma^2+4a^2t}\frac{k}{2}e^{-\frac{x^2+y^2}{2\sigma^2+4a^2t}}\frac{1}{\sqrt{\pi a^2t}}e^{-\frac{z^2}{4a^2t}}} \qquad \textit{(4.33)}$$

Keeping constant the pulse duration, and applying the logarithmic function on both sides of Eq. (4.33), a function in the form described in Section 4.1 is obtained. Indeed, from Eq. (4.33), the following relation is obtained:

$$\boldsymbol{\frac{x^2}{A}+\frac{y^2}{A}+\frac{z^2}{C}=1} \qquad \textit{(4.34)}$$

where *A* and *C* are arbitrary constants. Equation (4.34) is commonly known as an ellipsoid equation; it defines the isothermal function. It can be considered that the ablation process, for a thermal ablation, takes place when the material exceeds a certain temperature. In this case, when the thermal effects have a dominant role in the ablation process, the isothermal function describes the crater shape.

It should be noted that the maths developed up to this point does not intend to find the classical solution of the thermal ablation model that has been developed and studied over the years. Not even is the goal of Eq. (4.33) to simplify the solution of the PDE describing the heat problem. The main goal is to demonstrate that, under certain hypotheses that allow the use of erfc asymptotic expansion, it is possible to identify an isothermal function. This function is described by Eq. (4.34) and permits a relation to be built on the form of z=f(x,y).

After the definition of the thermal function, also a non-thermal function can be defined. As it was described in Section 2.2, there are several ways to model the non-thermal ablation mechanism. To obtain a function in the form of z=f(x,y), the thermal diffusion was neglected in this case, to identify the non-thermal function based on the energy distribution inside the sample. Thus, to describe the energy distribution inside the sample, the Gaussian energy beam distribution was imposed together with the energy beam distribution defined by the Lambert-Beer law, which describes how the energy is distributed along the z axis. Therefore, the pulse energy distribution inside the sample is described by

$$s(x,y,z) = \frac{Q}{2\sigma^2} e^{-\frac{x^2+y^2}{2\sigma^2}-kz} \qquad (4.35)$$

Similarly to Eq. (4.33), the logarithmic function can be applied to both sides of Eq. (4.35), obtaining:

$$\frac{x^2}{A_1} + \frac{y^2}{A_1} + \frac{z}{C_1} = 1 \qquad (4.36)$$

where A_1 and C_1 are arbitrary constants. Equation (4.36) is known as a paraboloid function.

Finally, two functions in the form of z=f(x,y) have been obtained and that will be compared with the experimental crater obtained as an alternative method to quantify the amount of thermal effects induced by the material laser ablation.

4.1.5 Quantitative factor

To quantify the amount of the thermal (or non-thermal) effects on the crater shape, a quality factor was defined. The experimental 3D craters were compared against the 3D surfaces identified by Eq. (4.34) and Eq. (4.36), respectively. The closest function to the crater was identified using the coefficients (A, C, A_1, C_1) that minimise the residual sum of squares (RSS) between the function and the experimental data.

$$\boldsymbol{RSS_e = \sum_{i,j}\left(c_{i,j} - e(x_i, y_j)\right)^2 \ , RSS_p = \sum_{i,j}\left(c_{i,j} - p(x_i, y_j)\right)^2} \qquad \textit{(4.37)}$$

Where $c_{i,j}$ is the z value of the crated at the coordinate (x_i,y_j), $e(x_i, y_j)$ is the ellipsoid that minimise the RSSe at the coordinate (x_i,y_j) and $p(x_i, y_j)$ is the ellipsoid that minimise the RSSp at the coordinate (x_i,y_j) Thus, for each crater, two minimum RSS's were obtained: the first resulted from the comparison of the crater data shape with the ellipsoid function (RSS_e), and the second resulted from the comparison of the crater data shape with the paraboloid function (RSS_p). Using the two minimum RSS's, the quality factor was defined as the percentage difference (PD) :

$$\boldsymbol{PD = 100\frac{RSS_e - RSS_p}{\mathbf{average}(RSS_p, RSS_e)}} \qquad \textit{(4.38)}$$

In the case of non-thermal ablation, when there was no presence of thermal effects, $RSS_e > RSS_p$. This relation between the two values defined a positive PD, which indicates that the paraboloid function represents the crater shape better than the ellipsoid function. In the case for which the thermal effects were greater than the non-thermal effects, the $RSS_e < RSS_p$ and PD was negative. This meant that the ellipsoid function was a better representation of the crater than the paraboloid function. All these relations are summarised in Table 4-2.

Table 4-2 Summary of relations between the two regimes, functions, RSS, and PD

	Dominant function	RSS	PD
Non-thermal	Paraboloid	$RSS_e > RSS_p$	>0
Thermal	Ellipsoid	$RSS_e < RSS_p$	<0

4.2 Experimental design

The samples were the 3 in Silicon <100> wafers described in section 3.1. To verify the reliability of the two functions, a systematic study was performed, from the ultrafast regime to the microsecond regime. In Table 4-3 are reported the four regimes investigated. The femtosecond and the nanosecond regimes were investigated using the

LASEA system (Section 3.2.1), the picosecond regime using the 3D Micromac system (Section 3.2.2), and the microsecond regime using the SPI System (Section 3.2.3). The femtosecond laser had a fundamental wavelength at 1032 nm (Ytterbium based); meanwhile, the other lasers had a fundamental emission wavelength at 1064 nm (Neodymium based). Because of the small variation of laser wavelengths, all the silicon characteristics that are wavelength dependent (e.g. penetration depth coefficient) were considered equal for all the sources. All the three lasers were chosen with an M^2 smaller than 1.3 to prevent affecting the crater shape by the energy beam distribution. Thus, the energy beam distribution was considered Gaussian for all the beams.

Table 4-3 Laser beam parameters used corresponding to each pulse duration regime investigated

	Fs	ps	ns	µs
Pulse duration	310	10	25,50,70,110,150,170,220	2,4,6,8,10,12,14,16,18,20
Wavelength [nm]	1032	1064	1064	1064
M^2	<1.3	<1.2	<1.3	<1.3
Repetition rate [kHz]	250	10	10	10

The repetition rate and the galvo speed were determined to obtain separate pulses on the target surface to allow individual craters to be analysed (i.e. no crater overlapping). In every system, the marking speed was set at 1 m/s. Then, to obtain a separation of 100 µm, the repetition rate was obtained by Eq. 4.39:

$$\boldsymbol{Rr = \frac{m_s}{c_s}} \qquad \textbf{(4.39)}$$

where Rr is the repetition rate, m_s is the marking speed, and c_s is the spacing between two craters.

In the Amplitude laser (Section 3.2.1), a pulse picker was integrated in the system. Thus, it was not necessary to adapt the marking speed to the repetition rate to obtain the desired spots spacing. Then, the repetition rate was chosen to be 250 kHz.

For each pulse duration, the laser power (and consequently the energy per pulse and the fluence) were varied from the minimum to the maximum available on the laser source. When the ablation threshold was greater than the minimum emission of the laser, the tests were run from the ablation threshold value.

4.3 Data acquisition and Matlab post-processing

Figure 4-2 shows the data acquisition and post-processing flow implemented: from the data collection to the comparison of the PD for different regimes.

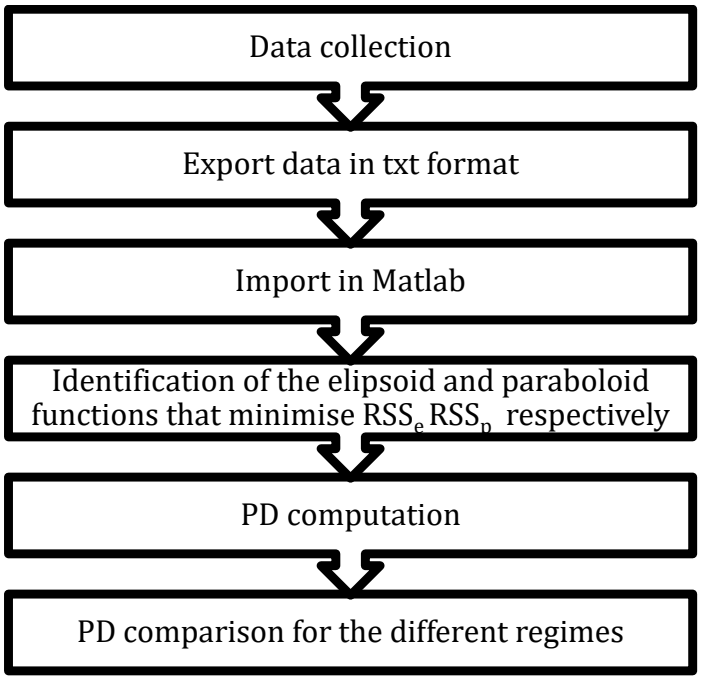

Figure 4-2 Schematic flow for the PD calculation process

After the craters were generated using the three laser facilities, they were measured using the Alicona microscope (for pulses on the nanosecond and the microsecond regimes) and using the GT-Contour (for pulses in the femtosecond and the picosecond regimes). With Alicona microscope the craters were acquired using x50 magnification with a lateral resolution of 1.50 µm a vertical resolution 0.1 µm while with the GT-Contour 10x magnification objective was used together with 1.5x lens; the lateral resolution was 1.5 µm and the vertical resolution was 0.1 µm.

Using the proprietary software provided by the two facilities, a certain area of the sample was analysed. The data were collected in a form of 3 columns corresponding to x, y and z values (which define the 3Dcrater shape). Data were exported as .txt files containing the 3 columns for the post processing by Matlab. Once that the data were imported in Matlab they were reshaped to be treat as a matrix. A graphical representation of an analysed area is shown in Figure 4-3.

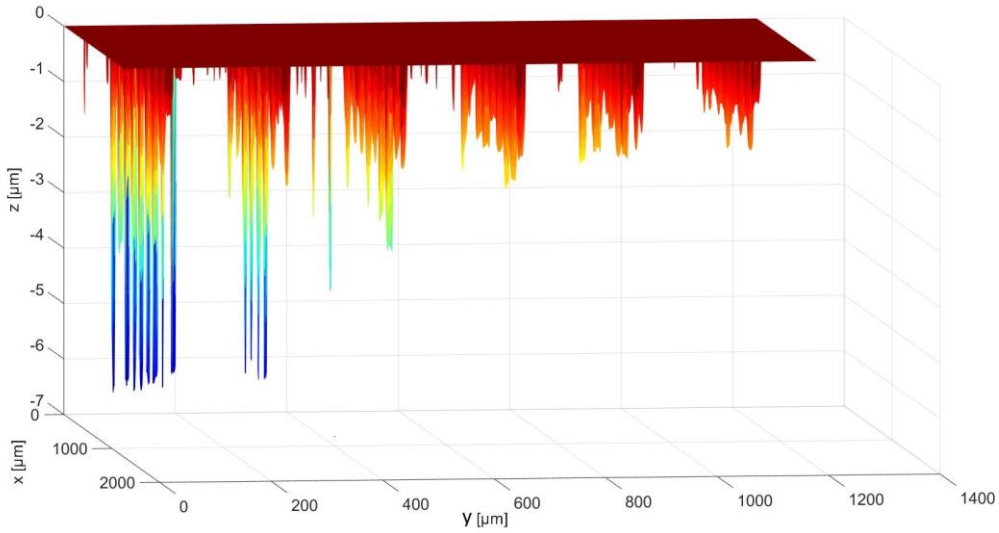

Figure 4-3 Example of imported data matrix 6x8. 8 craters are ablated along the x axis with the same energy while along the y axis the energy per pulse was decreased.

Figure 4-3 is an example of one data set that was imported and partially processed (the debris on the top surface was removed to highlight the craters). Along the x axis, the craters were made with the same energy, but along the y axis, the energy per pulse was decreased.

A sequential analysis followed the reshaping. For every crater, the ellipsoid and the paraboloid function that minimised the RSS_e and the RSS_p, respectively, were identified (Eq. 4.37). From a practical point of view, each point of the 3D experimental crater was compared with the closest point of the 3D function to find the coefficient of the functions described in Eq. (4.34) and Eq. (4.36).

After the two RSS's were calculated, the PD was computed by using Eq. 4.38. the number of replicated craters and successfully measured were 10 for each condition of pulse duration and energy per pulse for a total amount around 1200 craters. Consequently, each PD obtained resulted from the average of 10 craters, at least. The PD was compared by examining the pulse duration and the fluence. The comparison will be addressed in detail in the next chapter.

4.4 Results and discussion

The following section describes the results obtained using the new method developed to identify the thermal effect based on the evaluation of the crater shape by the PD. A comparison of the PD with the SEM picture of the same crater is presented. Thus, using

a classical analysis technique such as SEM analysis, the results obtained with the new method were verified.

Figure 4-4 shows the PD values for some representative pulse durations covering the entire range from the femtosecond to microsecond regime. The PD evaluation started from the ultrashort pulses (i.e. 310 fs), when a PD varying between 70% and 30% was seen, but upon increasing the pulse duration, the PD generally decreased. For high-energy pulses at 10 ps, and low energy at 70 ns and 220 ns, the PD values were around zero. For pulses at 220 ns and higher energy, the PD changed up to -25% and remained relatively constant (i.e. around -10 % of the PD) for pulses up to 4 μs. From these general observations, the crater shape follows the expected trend suggested in section 4.1. Indeed, the paraboloid function represents the crater shape better for pulses shorter than the phonon-photon coupling time. In contrast, the ellipsoid function works better for pulses longer than the photon-phonon coupling time. It is interesting to note that for nanosecond and picosecond regimes, the PD decreases with increasing fluence, suggesting that the fluence plays a fundamental role in driving thermal effects. The SEM were used to verify the results obtained by the PD study. They showed that in the 'non-thermal region' around the craters, no splashes occurred. Several modifications appeared in the 'intermediary region', and they became evident and clear in the 'thermal region', where a zone around the crater was covered by molten and ejected material debris. Next is provided a description of the PD for each of the regions identified (non-thermal, intermediary, and thermal) and its comparison with the SEM images.

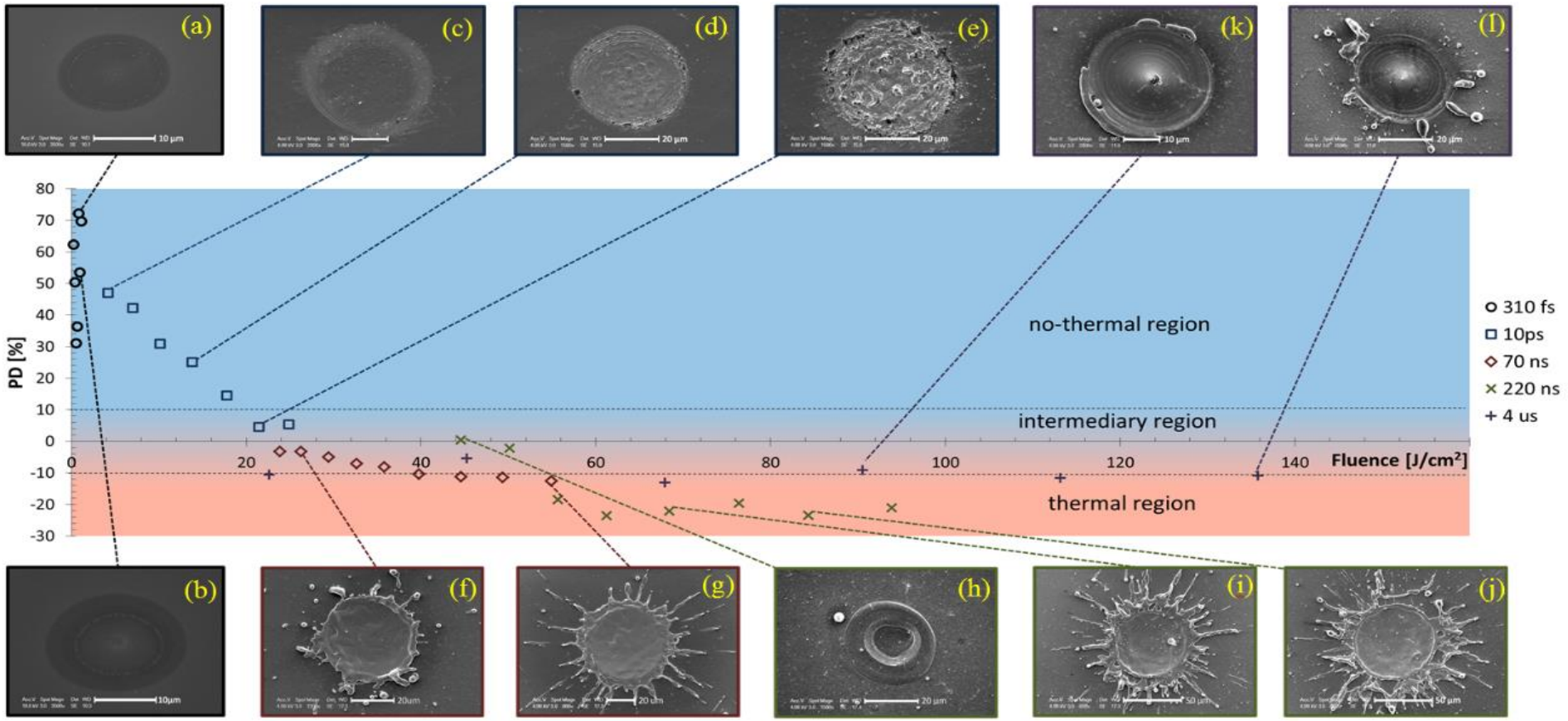

Figure 4-4 Percentage difference is reported for five different pulse durations: 310 fs, 10 ps, 70 ns, 220 ns, and 4 µs. A dotted line separates three regions: no- thermal (PD>10%), intermediary (-10%<PD<10%), and thermal (PD<-10%). Around the chart, SEM pictures are shown, connected to the related values.

4.4.1 Non-thermal region

The PD values related to the 310 fs pulse (Figure 4-4 circle legend) were greater than 30% and are in the 'non-thermal region'. This means that the parabolic function had a lower error than the ellipsoid function on representing the crater, suggesting the absence of relevant thermal effects. The SEM images confirmed the absence of relevant thermal effects: indeed, no morphological modifications were found to be attributed to a thermal process. Moreover, no surface differences between a crater close to the ablation threshold (0.3 J/cm^2) in Figure 4-4a and a crater at higher fluence (1.2 J/cm^2) in Figure 4-4b can be seen (excluding any role of fluence). This confirms that the distribution of PD values does not seem related to the fluence in this regime. However, it is notable that crater diameter increased with increasing fluence (see Figure 4-4a and Figure 4-4 b). This behaviour is described by the Liu's relation, and typically occurs in this pulse regime [148].

In the non-thermal region, even the PD values obtained with pulse duration in the picosecond regime (Figure 4-4, square points) had fluence lower than 20 J/cm^2. These points started from a value of 50% and decrease to a value of 10%. This means that when fluence is just above the ps ablation threshold, the paraboloid function can be considered the function that better describes the crater shape. However, the PD decreased, because of similar RSSe and RSSp values, when fluence increased. This suggests that when high fluence is involved in the picosecond regime, thermal processes can be initiated, reducing the non-thermal behaviour. The supporting SEM images confirmed the absence of strong thermal effects caused by increasing the fluence. However, a few small modifications on the crater bottom surface morphology suggested a change in the phenomena involved. In fact, for craters obtained with a fluence close to 4 J/cm^2 (Figure 4-4c), the crater surface was smooth and regular, but for higher fluence, the crater was irregular and some modification appeared on the crater bottom (Figure 4-4d). The volume of these irregularities was not significant compared to the crater ablated volume, and they cannot completely confirm the presence of thermal effects. However, they suggested, as well as the decreasing trend of the PD, some modification of the ablation mechanism.

4.4.2 Intermediary region

The two PD values for the picosecond regime at highest fluence of that regime were in the intermediary region between 10% and 0%. This means that, although the non-thermal mechanisms were still the most relevant, the thermal processes begin to be significant in the ablation process. The SEM images confirmed the presence of thermal effects on the crater: some significant crater modifications appear on the bottom, on the edge and around the crater (Figure 4-4e). The pulse duration (around 10 ps) was very close to the photon-phonon coupling time, and consequently it can be considered a borderline pulse duration. This explains why fluence plays a fundamental role in driving the typology of the ablation process. Moreover, the thermal and the breakdown mechanisms are not two separated phenomena; they can coexist, and they can both contribute to the crater formation [38]. Thus, a transition region around this pulse duration is expected.

In the intermediary region, craters obtained using pulses at 70 ns for fluence lower than 40 J/cm^2 were seen. The PD values go from -2% to -10%. Despite the negative values of PD, the values of RSS_p and RSS_e were similar, and the difference were not large enough to clearly identify whether the process were thermal nor non-thermal. This is in accordance with the condition described by the asymptotic approximation of Eq. (4.29). In fact, it was verified that for 220 ns, the asymptotic expansion can be used with an error lower than 4%; as 70 ns is a pulse duration value larger than the photon-phonon coupling time and smaller than 220 ns, so it cannot be included in thermal and neither in the non-thermal regime. However, the results show that the PD values were consistent even for pulse durations that do not satisfy the asymptotic condition or that are shorter than the phonon-photon coupling time and an intermediate regime can be identified. So, despite the various mechanisms that can take part in the removal process at this pulse regime [149], it seems that the method proposed can be applied to quantify the amount of thermal effects also for temporal regimes between the two defined in Section 4.1.4. The SEM picture for low fluence for this pulse duration (Figure 4-4f) shown debris and molten material around the crater edge. They are the effects of a thermal mechanism but are not strong enough to be the dominant ablation mechanism. This confirms the behaviour identified by the PD analysis.

The fluence effects were reduced compared to those in the picosecond regime: for 10 ps, doubling the fluence, the PD was reduced by almost 40%; meanwhile, for 70 ns, doubling the fluence, the PD was reduced by 10%. This can be explained by the plasma absorption effect that reduces the amount of energy absorbed by the sample [150].

Indeed, the plasma is generally generated several nanoseconds after that the laser pulse hit the sample, so there is no interaction with pulses in the picosecond regime, but the interaction starts with pulses in the nanosecond regime. Thus, although plasma is formed in both regimes, it interacts with the laser beam only for pulse durations starting from the nanosecond. When they interact, the plasma absorbs part of the laser energy beam, reducing the amount of energy delivered to the target. Consequently, the effect of fluence and the thermal impact is reduced.

In the intermediary region contained also PD values of 220 ns pulse with a fluence less than 50 J/cm^2. In this case, the PD value was close to 0%, which means that the RSS's of the two equations were almost equivalent. Then, it is not possible to identify the dominant function nor to identify if the dominant mechanisms driving the ablation are thermal or non-thermal.

The SEM image (Figure 4-4h), revealed a shape without splashes or debris around the crater but with a ring of molten material. This confirms the PD analysis: despite the fact that the 220 ns completely satisfies the condition to apply the asymptotic expansion, at low fluence the thermal effect were strongly limited. The crater size at this fluence was much smaller than expected. This indicates that the fluences used were close to the ablation threshold because only the more energetic part of the pulse can ablate.

4.4.3 Thermal region

The first group of PD values present in the thermal region was for the 70 ns pulse duration at fluence higher than 40 J/cm^2. These points were just below -10%, indicating the presence of a thermal mechanism. Accordingly, with the PD values, SEM images for this group of points indicate a relevant impact of the thermal mechanism. Several modifications are visible at the crater surface, such as splash or more generally residual of material ejection (Figure 4-4g).

The PD values for pulse duration equal to 220 ns obtained for fluence higher than 50 J/cm^2 decreased from -20% to -25%. This indicates that the RSS_e is smaller than RSS_p and the thermal effects are dominant. This pulse duration matches the requirements for the asymptotic condition; however, the PD did not decrease below the 25%. This happens because of the plasma absorption at high fluence: over certain fluence, the energy beam is absorbed by the plasma and the contribution of the fluence is reduced, as it is for 70 ns pulse duration in the intermediary region.

The SEM images confirm that for PD lower than -20%, changes in morphology caused by the thermal mechanism surround the crater (Figure 4-4i and Figure 4-4j). A large amount of splashed material was visible around the edge. The splashed material can be attributed to the phase explosion, which is a typical phenomenon occurring at this time regime [151].

Most of the PD values obtained in the microsecond regime were present in the thermal region as well. The behaviour was similar among the microsecond pulse durations tested, from 2 µs to 20 µs. For this reason, the 4 µs pulse duration, which better represent all the other pulse durations, is reported in Figure 4-4.

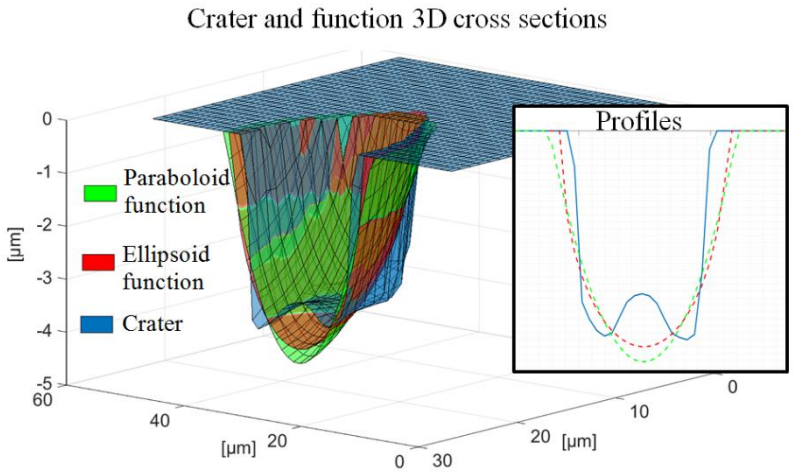

Figure 4-5 Example of 3D cross-sections of a crater and the two defined functions for a 4 µs pulse. The profile shapes are reported in the square.

The PD was around -10% for all the fluencies tested. At the first analysis, it seemed to be an unexpected result, because the pulses in the microsecond regime completely satisfy the condition required to apply the asymptotic expansion (4.29). For this reason, the PD values were expected to be much smaller, or at least they were expected to be smaller than the values obtained for the 220 ns pulse duration. This can be explained by observing the crater shape, and in particular, the crater profile. In , where both the cross-section and the profile are shown, a certain amount of molten material is present in the centre of the crater bottom. shows also the cross-sections and the profiles of the ellipsoid and the paraboloid function that minimise the RSS's for the crater. Observing the profiles, it is clear how the molten material in the centre of the crater increases RSS_e and RSS_p values. Thus, despite the difference between the two values, the "*average*(RSS_p,RSS_e)", which is affected by the central molten material, becomes higher and the absolute PD value decreases. Thus, the capability of the method to quantify the

thermal impact on the ablation process is slightly reduced, but the PD remains negative and in the thermal region despite the decreasing of its absolute value.

The SEM pictures confirm the presence of redeposited material in the centre of the crater (Figure 4-4k), indicating a primary role of the thermal mechanism in the ablation process. Moreover, the SEM images show that instead of the splashes around the crater, some residuals, which are restricted to a surface much smaller than the surface containing the splashes obtained in other regimes, are seen (Figure 4-4l). Consequently, thermal mechanisms such as phase explosion (discussed previously) can be excluded; instead, a more classical melting and evaporation can be identified as the primary thermal mechanism that drives the laser ablation. The two SEM pictures reported were obtained with a fluence of 90 J/cm^2 and with a fluence of 130 J/cm^2, respectively. However, they look similar to each other, and no notable differences are visible. Again, this behaviour is in accord with the PD values that are almost constant around -10%. This result suggests that for this regime the fluence does not influence the amount of thermal effect as noticed in other temporal regimes.

4.5 Conclusions

This chapter contains a systematic study of the effects of the pulse duration on the crater shape from the femtosecond to the microsecond regime. It was conducted using several laser facilities and exploiting a range of fluence for each available pulse duration tested. The study was supported by the new method developed together with the classical analysis of the thermal effect via SEM images.

The main findings of this work are summarised as follows:

1. Starting from the models on laser material ablation presented in the literature review, one analytical function (iso-thermal) was developed and another function (iso-energetic) was identified to approximate the crater shape of silicon single-pulse laser ablation. Each of the two functions was associated with a temporal pulse regime, and it was verified that the isothermal function approximates the crater shape well for pulses longer than 220 ns. In contrast, it was verified that the iso-energetic function works better for pulses shorter than 220 ns. This can be extended to analytical models for laser material ablation on a large scale. Indeed, the analytical model which used the overlapping of a single function to predict a 3D complex laser ablated structure, can be improved by

using the iso-thermal or the iso-energetic function, depending on the pulse duration involved. Small changes in the single laser pulse crater shape can be fundamental on a highly overlapped ablation process, and they can increase the accuracy of the final 3D shape prediction.

2. A novel method was developed to quantify the amount of thermal or non-thermal effects generated by silicon laser pulsed ablation. The method is based on the analysis of the crater shape instead of the analysis of the classical thermal morphology of induced features such as debris, HAZ, splashed, and redeposited material. The crater diameter is generally a few micrometres, while the morphology changes are on the micrometre or sub-micrometre size. The novel method allows the use of fast metrology techniques with micrometre lateral resolution (such as WLI or confocal microscopy) instead of classical methods with sub-micrometre lateral resolution (such as SEM, TEM, or AFM) because of the bigger size of the crater shape compared to the size of the generated thermal features. Thus, the method proposed, although it requires post-processing data analysis, is much faster than the classical analysis technique, and it allows evaluation of the presence or absence of thermal mechanisms in the laser ablation process in less time. Although the method was defined for pulses shorter than 10 ps or longer than 220 ns, the results for pulse durations in between these two values are in line with the remaining results. This reveals the consistency of the method also for the pulses in between the two pulse duration conditions.
3. The influence of the pulse duration on the crater shape was highlighted by the new proposed method. Based on the crater shape, a quantitative factor allowed three different pulse duration regions to be associated with three different thermal effect regions: non-thermal, intermediary, and thermal. Up to 10 ps, the results were in the non-thermal region; between 10 ps and 220 ns, the results were in an intermediary region; and for pulses equal to or longer than 220 ns, the results were in the thermal region. A parallel analysis study using the SEM picture was conducted and confirmed the results of the proposed method.
4. The proposed method developed and the SEM image analysis revealed that for pulses in the picosecond and the nanosecond regimes the fluence played an important role on the crater shape and consequently on the morphological aspect. Indeed, for these pulse regimes, when increasing the fluence, the thermal

effects on the crater shape and crater morphology increased. However, for pulses in the femtosecond and microsecond regimes, the fluence effect was not detectable, suggesting that in these regimes the fluence did not affect the single-pulse laser ablation. Thus, fluence must be considered for a complete description of the evolution of the thermal effects on ablated craters, based on the laser pulse duration.

5 THERMAL EFFECTS ON CRATER SHAPE FOR NONCONVENTIONAL LASER ENERGY BEAM DISTRIBUTIONS

Chapter outline

Chapter 4 included a discussion of the effect of laser pulse duration on the crater shape for a wide range of pulse durations. It was highlighted that for pulses longer than 220 ns, the thermal diffusion inside the sample drives a modification of the crater shape. In fact, the final crater obtained revealed a shape that did not correspond to the laser energy beam distribution inside the sample.

For this reason, in this chapter, the thermal effects on the crater shape are evaluated for two common non-conventional energy beam distributions: the round and the square flat-top. Starting from the heat diffusion phenomenon and considering the math developed in the previous chapter, applying a similar approach based on the comparison between the ellipsoid function and the energy beam distributions, the effect of the thermal shape is evaluated.

A study of silicon ablation using an infrared laser source at 220 ns was carried out. Using the quantitative factor developed in Chapter 4, an evaluation was performed to determine if the experimental crater shape was better approximated by the ellipsoid function or by a function representing the round (or the square) flat-top energy beam distribution. By applying this factor, the variation of the crater shape from the original energy beam distribution was evaluated. The evaluation was confirmed by the data collected via SEM analysis. It was shown that the square flat-top energy beam distribution was less sensitive to the thermal effects and the crater shape better matches the original energy beam distribution than the round flat-top energy beam distribution.

5.1 Extension of thermal and non-thermal functions for a round and a square flat-top energy beam distribution

In Chapter 4, was demonstrated that, for pulses longer than 220 ns, thermal diffusion can induce a change in the crater shape from the original shape related to the energy beam distribution. Indeed, it has been experimentally proven that, using a Gaussian energy distribution, the crater shape in the thermal regime results in an ellipsoid crater.

The following section would explain how the same concept can be extended to the two non-Gaussian energy beam distributions: a round and square flat-top.

The concept is that when the fluence and the pulse duration are high and long enough, respectively, it is reasonable to suppose that the corresponding crater shape does not represent the original energy beam distribution. In fact, if the energy and pulse duration are high and short enough, respectively, the heat diffusion contribution can overcome the contribution of the energy beam distribution inside the sample to drive the material ablation process. Because of the orthotropic nature of the silicon wafer employed, the diffusion of the temperature can be considered omnidirectional. This means that the heat diffuses with the same speed and the same quantity in all directions. When the energy source is a point, the isothermal function in a 3D orthotropic medium can be described by the ellipsoid function (Eq. (4.34)). However, if the diffusion effects are large enough, a generic energy beam distribution can be considered as a point source and the resulting crater can differ from the laser energy beam distribution used to ablate. Figure 5-1 shows a graphic representation of this concept: Figure 5-1a shows the Gaussian energy beam distribution inside the medium as described by Eq. (4.36) (paraboloid function), the arrows indicate the propagation of the heat inside the sample, while Figure 5-1b

shows the difference between the paraboloid (blue shape) and the ellipsoid (red shape) function with the same depth and radius.

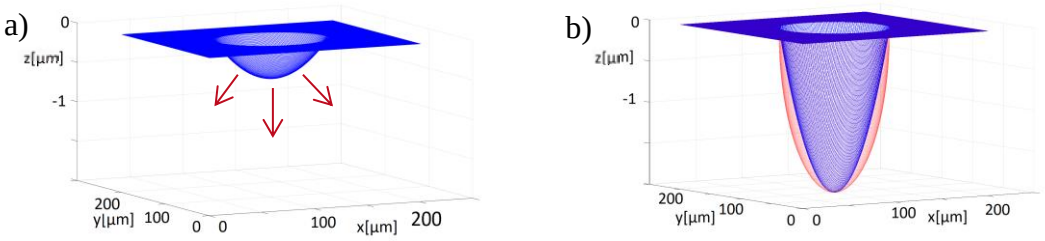

Figure 5-1 Description of the change in crater shape due to thermal effects for a Gaussian energy beam distribution: a) Paraboloid energy beam distribution based on a Gaussian energy beam distribution (the red arrows indicate the directions of the heat diffusion), and b) Comparison between the paraboloid function (blue) and the ellipsoid function (red) after the thermal diffusion

It is important to highlight the scale between the x, y, and z axes. The z axis is approximately 10 times smaller than the x and y axes. This is a common characteristic of laser ablation: while the x and y minimum crater sizes depend on the diffraction limit, the size along the z axis is based on several other factors, such as penetration depth or pulse duration. For this reason, the crater depth is generally smaller than the crater diameter. Then considering the same quantity of heat diffusion in all directions, the ratio between the crater size (defined by diameter and depth) and the increment due to the heat diffusion are much more visible along the z axis than along the other axes.

In this chapter the thermal effects at the regime of 220 ns, which was identified in the previous chapter as the pulse duration with the strongest thermal effect on the crater shape was evaluated, on two non-classical energy beam distributions: the round flat-top and the square flat-top. The objective is to verify whether the crater shape is better approximated by the ellipsoid function when affected by the thermal effects even when the initial energy beam distribution is not Gaussian. Figure 5-2 highlights the shape of the round and square flat-top energy beam distributions (Figure 5-2a and Figure 5-2c, respectively) and compares them with the ellipsoid function (Figure 5-2b and vd, respectively).

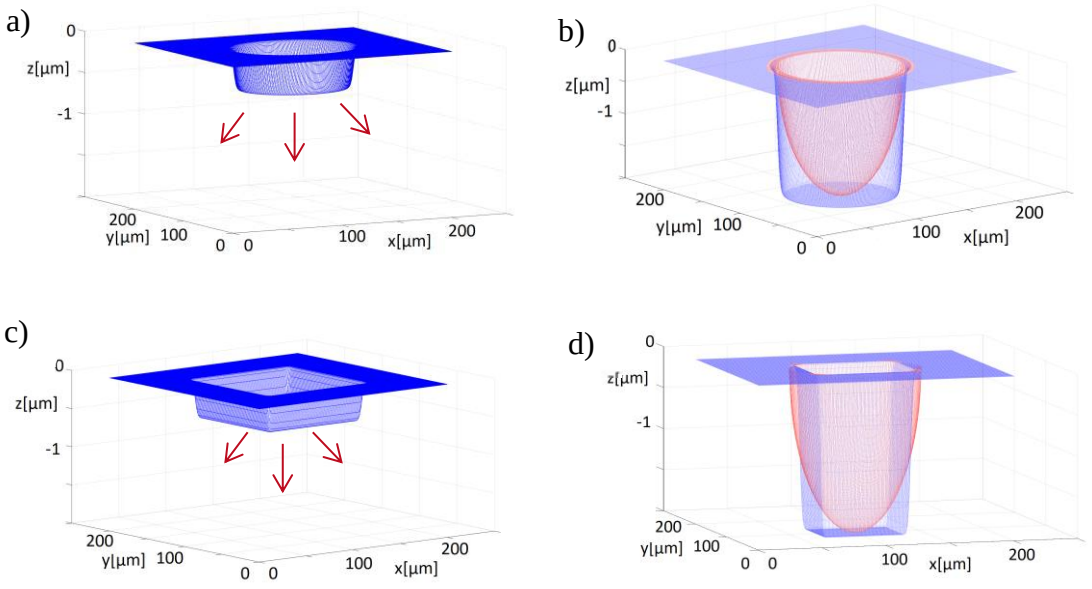

Figure 5-2 Description of the change in crater shape due to thermal effects for a) round flat-top and c) square flat-top beam energy beam distribution. Comparison with the ellipsoid shapes after heat diffusion with , the round flat top b) and the square flat top d) respectively.

5.1.1 Square and round flat-top functions and the new quantitative factor

Both of the round and the square flat-top energy beam distributions are characterised by having a flat-top profile. In the first case, the section in the x-y plane is defined by a circle, while in the second case, it is defined by a square. Based on the experimental profile, the z function for the round flat-top beam is defined as

$$z = C_2 * erfc(x^2 + y^2 - A_2)/D_2 \qquad (5.1)$$

where C_2 and A_2 are constant for depth and radius, respectively, and D_2 is a constant that defines the tilt of the lateral surface of the beam.

Similarly, the z function for the square flat-top beam is defined as

$$z = C_3 * erfc(-x - A_3)/D_3 * erfc(x - A_3)/D_3 * \\ * erfc(-y - A_3)/D_3 * erfc(y - A_3)/D_3 \qquad (5.2)$$

where C_3 and A_3 are constant for depth and radius, respectively, and D_3 is a constant that defines tilt of the side surface of the beam.

Once the two profile functions are defined, it can be proceeded by defining a quantitative factor capable of revealing if the crater shape obtained is more similar to an ellipsoid or to the original energy beam distribution. As shown in Section 4.1.5, the first step is to identify the error between the experimental crater and the functions. Then, in addition to the RSS_e defined in Eq. 4.37 , two new RSS's are calculated, for the round (RSS_{round}) and square (RSS_{square}) flat-top energy beam distributions as follows:

$$\boldsymbol{RSS_{round} = \sum_{i,j} \left(c_{i,j} - round(x_i, y_j)\right)^2 \ , RSS_{square} = \sum_{i,j} \left(c_{i,j} - square(x_i, y_j)\right)^2} \qquad \boldsymbol{(5.3)}$$

where $round(x_i, y_j)$ and $square(x_i, y_j)$ are the shape coordinates corresponding to Eq. (***5.1)*** and Eq. (***5.2)***, respectively.

As mentioned in the previous chapter, the quantitative factor based on the PD was used to determine the degree of thermal effect. But in this case two PDs were needed to conduct two comparisons: the first between the ellipsoid function and the round flat-top (PD_{er}), and the second between the ellipsoid and the square flat-top (PD_{es}):

$$\boldsymbol{PD_{er} = 100 \frac{RSS_e - RSS_{round}}{average(RSS_{round}, RSS_e)}} \qquad \boldsymbol{(5.4)}$$

$$\boldsymbol{PD_{es} = 100 \frac{RSS_e - RSS_{round}}{average(RSS_{round}, RSS_e)}} \qquad \boldsymbol{(5.5)}$$

The case PD>0 indicates that the RSS_e value was bigger than the RSS (round or square) one. This meant that thermal effects were not large enough to change the crater shape from the shape defined by the energy beam distribution to the ellipsoid shape. The case PD<0 indicates that the RSS_e value was lower than the RSS (round or square) one. This meant that thermal effects were large enough to change the shape of the crater from the shape defined by the energy beam distribution to the ellipsoid shape. It is interesting to note the slightly different meaning of the PD compared to the one evaluated in the previous chapter, even though they were calculated in the same way. That is because, the pulse duration (220 ns) mentioned in this chapter was in fact in the thermal ablation regime. Then, the PD values did not provide an indication of the ablation type (thermal

or non-thermal) but it gave an insight about the capability of the experimental crater to keep the initial energy beam shape or to be modified by the heat diffusion to an ellipsoid shape. However, PD actually indicated if the thermal ablation process has a strong or weak effect on the modification of the crater shape. These relations are summarised in Table 5-1.

Table 5-1 Summary of the relations between the two cases: the functions, RSS, and PD

Thermal effect	Dominant function	RSS	$PD_{es\ //er}$
Weak effect	Square or round flat-top	$RSS_e > RSS_{round//square}$	>0
Strong effect	Ellipsoid	$RSS_e < RSS_{round//sqaure}$	<0

5.2 Experimental design

The laser parameters used in this experiment are reported in Table 5-2.The facility used to carry out the experiments was the LASEA laser system, described in Section 3.2.1.

Table 5-2 Laser parameters used for the round and the square flat-top energy beam distribution

	Round and square flat-top
Pulse duration [ns]	220
Wavelength [nm]	1064
Repetition rate [kHz]	10
Fluence [J/cm^2]	From 33 to 43

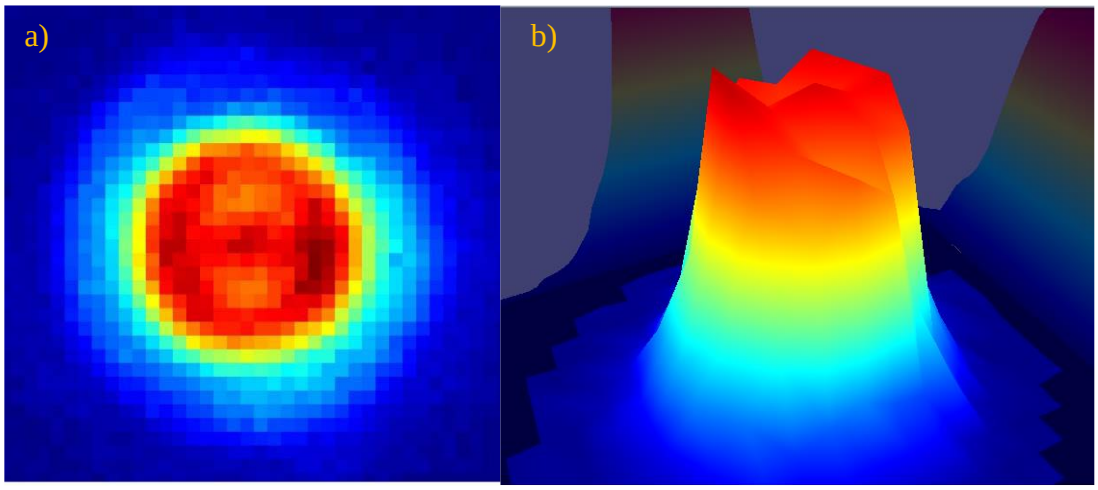

Figure 5-3 Energy beam distribution using the round flat-top energy beam shaper: a) top view, b) 3D reconstructed profile

The maximum fluence value achieved in this experiment was smaller than the fluence reached using the same pulse duration with a Gaussian energy beam distribution. This was because, to obtain a good shape, it was required to respect the requirement of the Diffractive Optic Element (DOE). To accomplish this, the laser beam was cut using an iris, and part of the power was lost.

The two energy beam shapes, round and square flat-top, were obtained using the DOE described in Section 3.2.4.3. The energy beam distribution in the focal plane was acquired using the energy beam shape analyser described in Section 3.3.2. Figure 5-3 shows the energy beam distribution for the round flat-top, while Figure 5-4 shows the energy beam distribution obtained with the square flat-top energy beam shaper.

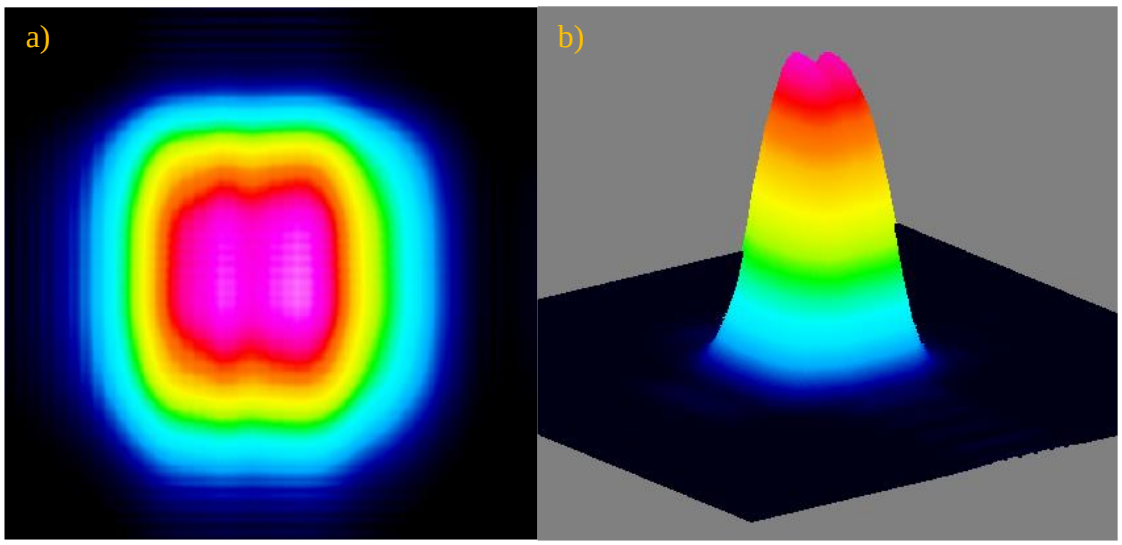

Figure 5-4 Energy beam distribution using the square flat-top energy beam shaper: a) top view, b) 3D reconstructed profile

5.3 Data acquisition and Matlab post-processing

The methods for data acquisition and post-processing were equivalent to the methods described in Section 4.3. In particular, the data were collected by an optical microscopy technique and then exported in ".txt" format and post-processed by Matlab. The Matlab code was changed to meet the new requirements (the introduction of two new functions and the evaluation of two new PDs).

5.4 Results and discussion

Figure 5-5 shows the PD values obtained for both, the square and the round energy beam distributions. While for the square flat-top energy beam distribution the PD values were almost constant around the value of 10%, for the round flat-top energy beam distribution the PD values decreased from a 4% to a value of around -20% by increasing the laser fluence from 33 J/cm^2 to 43 J/cm^2 . To better explain these two behaviours, these results were compared with the SEM analysis conducted for both energy beam distributions in the following section.

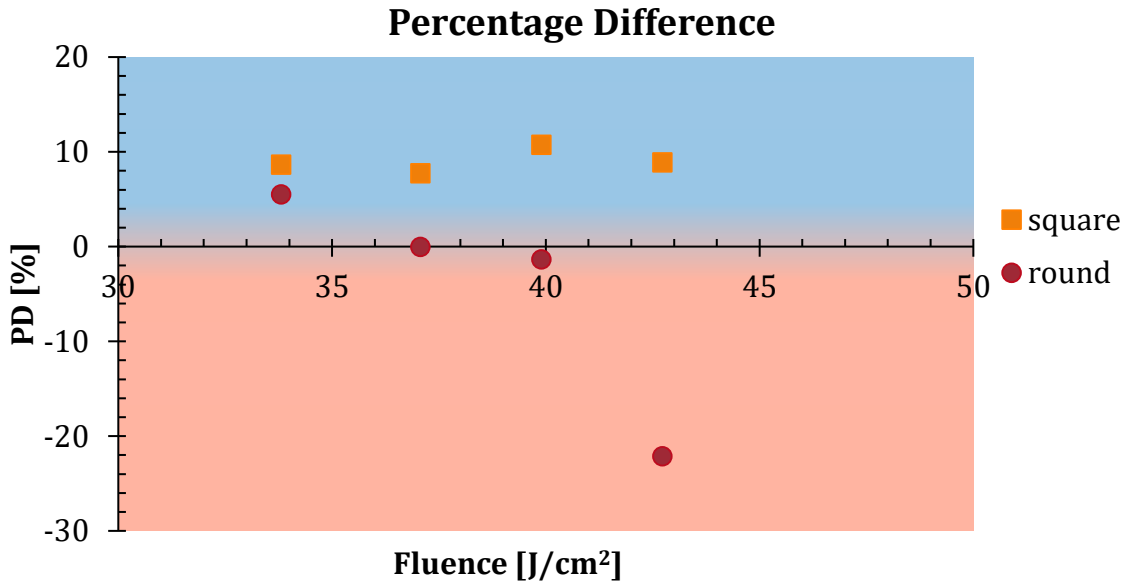

Figure 5-5 Percentage difference (PD) for the two energy beam distributions: the legend of squares and circles indicates the values obtained with the square flat-top and the round energy beam distribution, respectively.

5.4.1 Round flat-top energy beam distribution

Referring to Figure 5-5, the PD values for the round flat-top energy beam distribution varied from 7% using a fluence (33 J/cm^2) close to the ablation threshold, to -22% for higher fluence (43 J/cm^2). This means that for fluence close to the ablation threshold, the experimental craters were better approximated by the round flat-top function, while for higher values of fluence, the craters were better approximated by the ellipsoid function. The SEM images reveal the impact of the laser fluence at different levels on the final crater shape. Figure 5-6 shows the SEM images of the crater obtained: in Figure 5-6a (33 J/cm^2) the thermal effects were limited to molten material on the crater

rim; in Figure 5-6b (43 J/cm^2), the splashes of molten material were all around the edge and partially inside the crater itself.

Looking at more detailed morphological features, Figure 5-6a shows that the bottom of the crater was flat, and the crater shape matched the round flat-top energy distribution that was measured. This corresponds to a theoretical positive PD value and agrees with the PD values calculated from the experimental data. Conversely, the crater bottom of Figure 5-6b did not seem flat but revealed a curved surface, indeed a central darker area compare to the crater side area is visible in the SEM image, indicating a deeper zone in the centre of the crater. Moreover, the SEM image, suggest a certain roughness on the bottom of the crater and with the curved surface, corresponding to a negative PD. Moreover, the splash around the edge gave a contribution to reduce the step on the edge. Combining the results of the PD and the SEM images, it was found that the primary variation effects on the crater shape were due to the morphological transformations on the bottom. The effects on the edge gave a lower, secondary contribution.

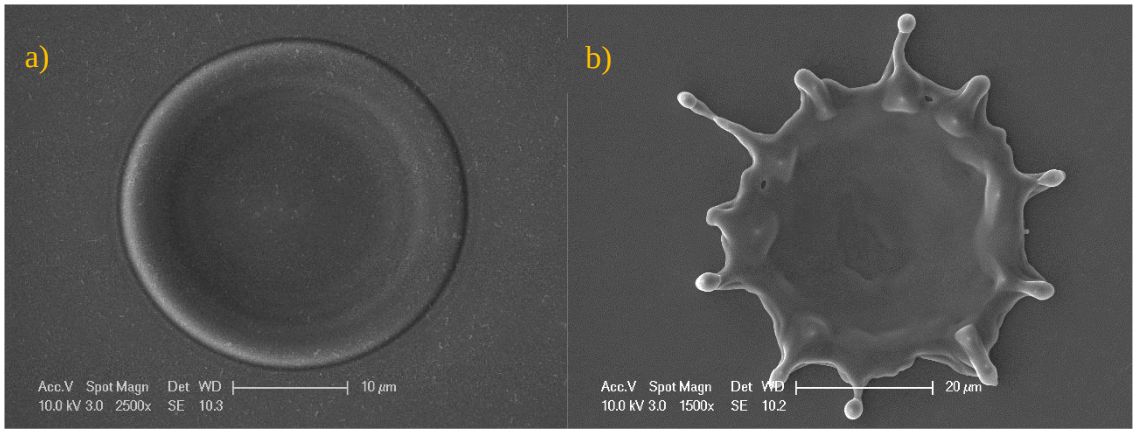

Figure 5-6 SEM images of the crater obtained using the round flat-top energy beam distribution: a) 33 J/cm^2; b) 43 J/cm^2

The PD values and the SEM analysis both suggested that the crater shape obtained was not flat-top for the high fluence over 40 J/cm^2. Consequently, for higher fluence than 40 J/cm^2, the round flat-top energy beam distribution does not maintain the experimental crater shape.

5.4.2 Square flat-top energy beam distribution

For the square flat-top energy beam distribution, the PD values (Figure 5-5) were constant around 10% for the whole range of fluence studied. This means the square flat-

top shape approximated the experimental crater with a smaller error than the ellipsoid shape. Thus, despite the relevant thermal effect that can be associated with the time regime operated, the crater shape was kept more like the laser energy beam distribution than to the ellipsoid shape.

The thermal effects are visible in Figure 5-7: Figure 5-7a reports a crater obtained with fluence (37 J/cm^2) close to the ablation, while Figure 5-7b reports a crater obtained at a higher fluence (45 J/cm^2). On both craters, the splashes caused by the thermal effects were present along the crater edges. In Figure 5-7b, in addition to the splashes, a high amount of redeposited material along the edge, which generates a rim, was visible. Moreover, a certain amount of debris was deposited in the form of solidified drops, highlighting the presence of a strong thermal process because of the clear melting nature of the material drops. In both cases, the bottom of the crater did not seem flat. Even the edges were not very steep because of the splash. Figure 5-7b shows that in the bottom of the crater are two zones with a rectangular shape. These two zones were generated in agreement with the shape obtained by the analysis of the energy beam distribution described in Figure 5-4.

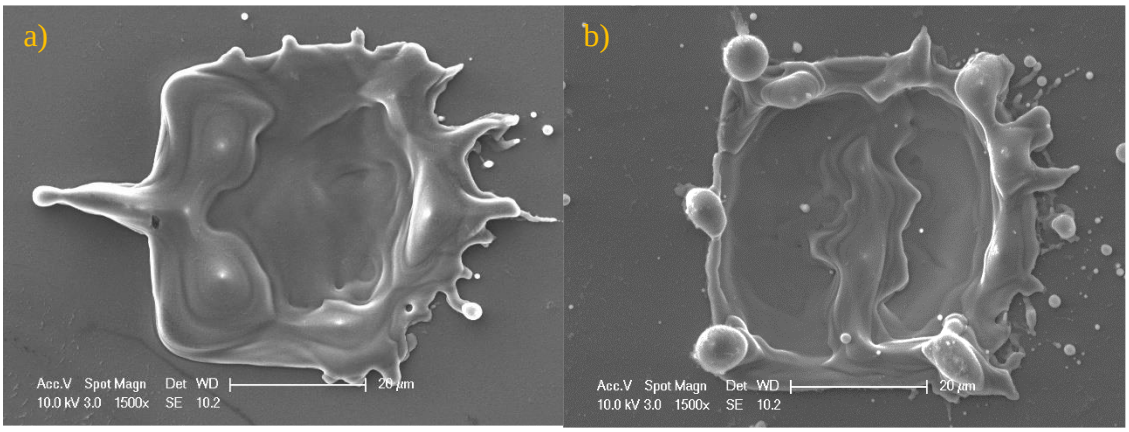

Figure 5-7 SEM images of the crater obtained using the square flat-top energy beam distribution: a) 37 J/cm^2; b) 43 J/cm^2

Thus, even though thermal effects were present and visible, the crater shape cannot be approximated with the ellipsoid function. The approximation made by the square flat-top shape produced better results.

This behaviour can be explained by the different sections between the ellipsoid (circle) and the square flat-top (square) energy beam distributions. As highlighted in Section 5.1, the major effects of heat diffusion are along the z axis because the crater depth value is smaller than the diameter. Indeed, if the heat diffusion propagates only for few

micrometres in all directions, the effects will be more visible along the z axis where the electromagnetic penetration at high temperature is around one micrometre, rather than on the x-y plane where the spot size is around tens of micrometres. This means that the major contributions of the thermal effects will affect the crater shape bottom rather than its side. Then, the thermal effect to change the square cross-section of the square energy beam distribution to a round shape one (which is the one of the ellipsoid function) must be higher than the one of 43 J/cm^2 induced at 220 ns or in other words the heat diffusion on the x-y plane is not enough to modify the section from round to the square one (the one of the square flat top energy beam distribution).

This was also congruent with the fact that the crater shape obtained with a round flat-top at the same fluence was better approximated by the ellipsoid function. In fact, both the round flat-top function and the ellipsoid function have a round cross-section on the x-y plane. The crater shape modifications generated by the thermal effects along the z axis were much more relevant compared to the modifications along the x and y axis, because the cross-sections remain the same. As explained before, the z direction was much more affected than x and y directions by the thermal effects. Thus, it was easier, in terms of fluence and pulse duration, to change the crater shape from the round flat-top shape to the ellipsoid shape rather than the square flat-top shape.

5.5 Conclusions

This chapter presented a comparison between the craters obtained using a round energy beam distribution and those obtained using a square flat-top energy beam distribution at a range of fluence levels (33 to 43 J/cm^2) on silicon. The study was conducted using a pulse duration of 220 ns. It was focused on the identification of the crater shape capability to keep a non-Gaussian energy beam distribution in a thermal nanosecond regime. By PD evaluation and by the support of the SEM analysis, the following findings were identified:

1. Starting from the considerations on the isotropic nature of the heat diffusion, the method developed in the previous chapter was extended to quantify the amount of thermal effect for a round and a square flat-top energy beam distribution. By extension, it was possible to estimate whether the experimental crater shape was better approximated by an ellipsoid function or the original energy beam distribution.

2. A round flat-top energy beam distribution was investigated with infrared 220 ns pulses. For fluence close to the ablation threshold, the crater was better approximated by the function replicating the round flat-top energy beam distribution than by the ellipsoid function, but for fluence sufficiently higher than the ablation threshold, the crater shape had an opposite behaviour. Indeed, for high fluence, the ellipsoid function approximated the crater better than the function replicating the round flat-top energy beam distribution. This was caused by the amount of splashes due to the thermal effects involved in the process that reduced the step on the edge, increased the bottom roughness, and reduced the flatness of the crater bottom.
3. A square flat-top energy beam distribution was investigated with infrared 220 ns pulses. For the whole fluence range analysed, the function based on the energy beam distribution better approximated the experimental crater shape, despite the strong thermal effects visible on the surface of the crater (e.g splashes and drops of melted material) and on the bottom of the crater (e.g. the increase in roughness and decrease in flatness). The high capability to keep the original energy beam distribution shape in the crater shape was explained by the different cross-sections of the ellipsoid function (circular) and the square flat-top function (square) and the small value of the electromagnetic penetration along the z axis compared to the diameter value.

6 INVESTIGATION OF THE POLARISATION EFFECT FOR NONLINEAR ABLATION IN THE FEMTOSECOND PULSE REGIME

The effects of polarisation on linear ablation are well-known and they are defined by the Fresnel's equations. These equations describe different polarisation states and different incidence angles of the laser beam with the surface, the polarisation states influence the reflectance and consequently affect the material absorption. However, the effects of polarisation on nonlinear absorption in the femtosecond pulse duration regime, in particular for a multiple-pulse process, are still unclear because of the various phenomena present in this time regime. Moreover, on nonlinear ablation, the formation of Laser Induced Periodic Surface Structures (LIPSS) can generate complex crater surface structures and can induce more complex interaction mechanisms. This chapter shows how some crater morphological behaviours are related to polarisation during nonlinear ablation.

The chapter identifies a novel correlation of the polarisation effects on LIPSS formation and on crater depth. It discusses how a LIPSS formation threshold that was lowered by using linear polarisation rather than circular one. Moreover, it was found that LIPSS periodicity reveals a dependence on polarisation: the maximum periodicity value was associated with parallel polarisation. The value decreases for circular polarisation and reaches the minimum for perpendicular polarisation. To identify any correlation with the crystal structure as suggested from previous studies, first the study was performed on the silicon crystal structures, Si<100> and later it was extended to Si<111>.

The early surface structure formation typically leads to an increase in absorption and crater depth by inducing a multi-scattering process. For this reason, an analysis of the crater depth was performed and is presented here. A small difference in depth was identified between the craters formed with circular and linear polarisations, suggesting that the induced structures are driving a change in the absorption for a certain regime of pulse number.

6.1 Experimental design

In this section, a detailed experimental description is reported, focusing on the polarisation. The LASEA facility, described in Section 3.2.1, was used. Although two laser sources (ns and fs) were available in this facility, the fs source was selected because it was the only source that permitted investigation of nonlinear absorption. The experiment was split in two phases: the first focused on the crater depth and the second on the LIPSS. The polarisations tested were identical for both phases; the fluence and the number of pulse ranges were different for each phase and are specified later.

6.1.1 Polarisation setup and configuration

To change the polarisation, the two waveplates described in section 3.2.4.1 were installed. The laser beam polarisation at the exit of the laser was parallel. In the laser system a quarter waveplate was pre-installed. Rotating this waveplate by 45º, the laser beam was changed from parallel to circular and vice versa when rotated back to 0º. Keeping the quarter waveplate at 0º and inserting a half waveplate, it was possible to change the polarisation from parallel to perpendicular. The repeatability of the waveplate rotation position was confirmed by the rotation system, which was provided with a backlash-free micrometre adjustment. Using the beam splitter described in

Section 3.2.4.2, the power of the parallel and the perpendicular components were measured. The polarisation contrast ratio was the parameter used to quantify the amount of vertical and parallel polarisation of the laser beam, the higher the contrast ratio the more "polarised" the laser beam. The contrast ratio measured after the waveplate was better than 1:100, as specified from the laser datasheet. However, the best contrast ratio achievable on the workpiece sample, by the optimisation of the waveplate position, was 1:20 for parallel polarisation and 1:37 for perpendicular polarisation. The optics inducing the decrease of the contrast ratio were inside the z-shifter and were not removable because they were integrated in the galvo head.

6.1.2 Secondary laser parameters: fluence and number of pulses

In this experimental setup, two secondary, but no less important, laser parameters were exploited, because as it was reported in Section 2.4.4 the polarisation effects are usually correlated to other parameters. These parameters were the fluence and the number of pulses delivered on the same position. Table 6-1 summarises the experimental laser and material parameters.

Table 6-1 Laser parameters and material used for the study of the effects of polarisation on LIPSS

Laser parameters	
Polarisation	Parallel, perpendicular, and circular
Fluence [J/cm^2]	From 0.069 to 0.82
Number of pulses	40, 50, 60, 80, 100, 120, 150, 200, 250, 300, 350, 400, 500, 600, 700, 800, 900 (at 0.069 and 0.076 J/cm^2)
	2, 3, 4, 6, 8, 12, 14, 16, 18, 20, 25, 30, 35, 40, 45, 50, 55 (at 0.56 and 0.82 J/cm^2)
Material parameters	
Crystal structure	Si <100> and Si <111>

For the study related to LIPSS, each polarisation test was divided into two main regimes. Indeed in Section 2.4.4 LIPSS formation was identified for two regimes. The first regime was identified as "beneath the ablation threshold (around 0.3 J/cm^2): for this regime two fluence values were investigated (0.069 and 0.076 J/cm^2) for a number of pulses range from 40 to 900. The second regime was identified as "above the ablation

threshold": in this regime two fluence values were investigated (0.56 and 0.82 J/cm^2) for a number of pulses ranging from 2 to 55. In addition, a first experimental stage was performed on the silicon crystal structures, Si<100> and later it was extended to Si<111>.

For the study related to the crater depth, for each polarisation, the fluence ranged from 0.225 to 1.8 J/cm^2 and the number of pulses were investigated from 10 to 60, as described in Table 6-2.

Table 6-2 Laser parameters used for the study of the effects of polarisation on crater depth

Laser parameters	
Polarisation	Parallel, perpendicular, and circular
Fluence [J/cm^2]	0.225, 0.4, 0.59, 0.795, 1.01, 1.21, 1.39, 1.54, 1.65, 1.73, 1.77, 1.8, 1.81
Number of pulses	10, 20, 25, 30, 35, 40, 50, 60

6.2 Analysis method

The following two methods were used to measure the effects of laser polarisation on nonlinear absorption.

The first characteristic evaluated was the area covered by LIPSS. To measure the amount of LIPSS that were covering a certain area, a method based on the PSD was developed, using SEM image acquisition and Matlab post-processing.

The second crater characteristic evaluated was the depth. Once the 3D crater shape was measured (using Alicona microscope), the crater depth was evaluated by measuring 4 crater profiles by Matlab post-processing, with each profile sampled at sampled at 0, $\pi/4$, $\pi/2$ and $3\pi/4$ respectively

6.2.1 LIPSS data acquisition and PSD based analysis method

As described in Section 2.4.4.4, LIPSS analysis was conducted using several types of facilities (e.g. AFM and SEM) and based on different post-processing techniques (e.g. DFT, 2DFT, PSD). Despite the AFM analysis would be the best method to analyse LIPSS it is too time consuming for a high number of crater as the one investigated in this study. Indeed, as described in Section 2.4.4.4 the time for an AFM analysis can be at least 10 time more compare to the SEM analysis. For this reason, the SEM is a good

trade-off between analysis time and result information. Here a hybrid method based on the SEM images and the PSD that can obtain the LIPSS periodicity, orientation, and amount of LIPSS over a certain area is defined.

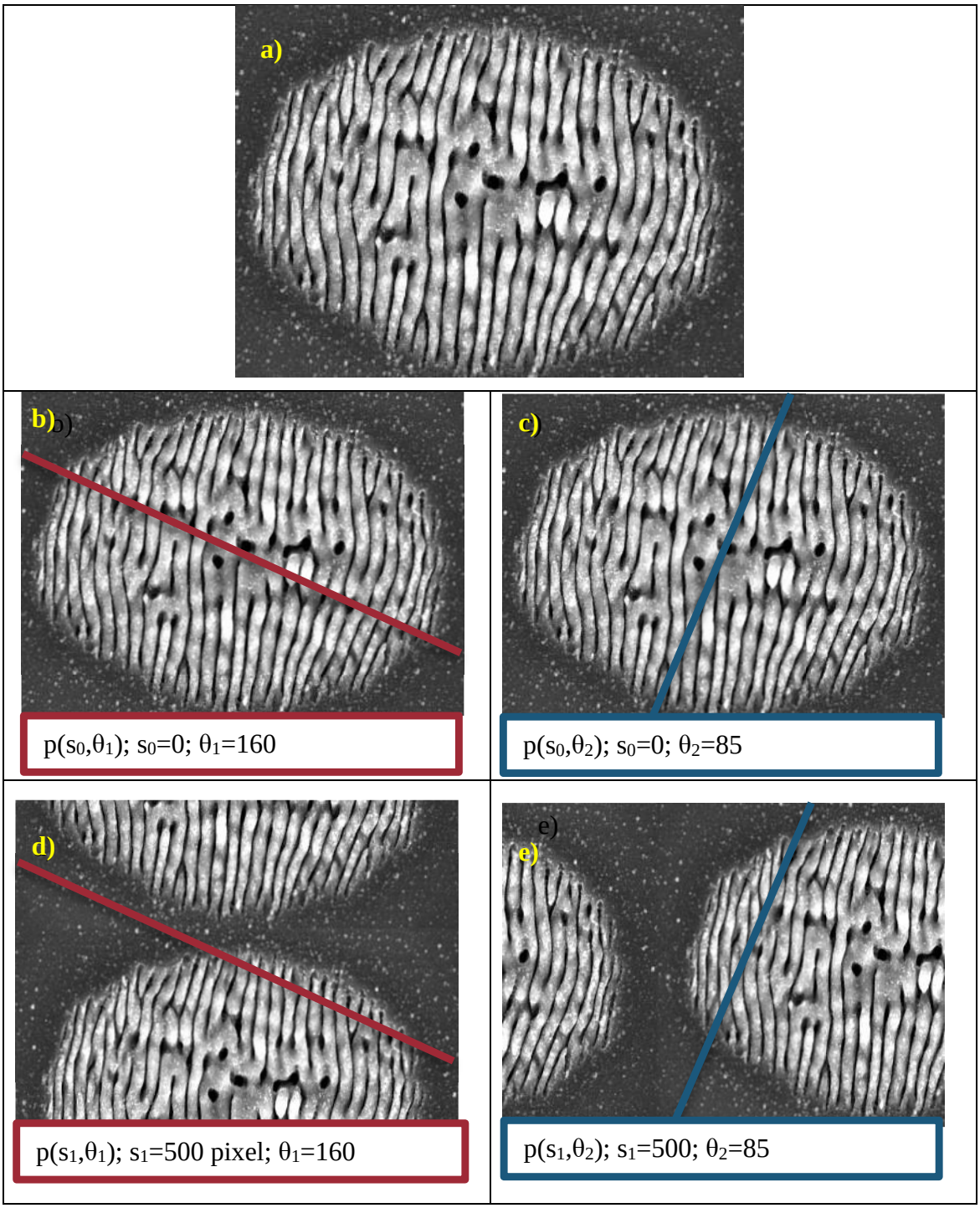

Figure 6-1 Graphic example of the method used to define the variable profile (s,θ): a) image given from the SEM; b) and c) profile acquired for two different angle θ_1 and θ_2; d) and e) profile acquired for two different angle θ_1 and θ_2 and shifted along y and x axis respectively.

All the SEM pictures were acquired using a magnification of 3500X, a beam energy of 10KeV, and a working distance of 10 mm. The signal was collected using only the secondary electron detector.

Figure 6-1a shows a classical image of data obtained by the SEM analysis. The picture data can be considered as a matrix *M*x*N*, where *M* is the number of rows and *N* is the number of columns which correspond to the image pixel number. Each cell contains an integer value between 0 and 255.

A picture profile is defined by the variable *p(θ,s).* The following 4 points describe how *p(θ,s)* is defined: *i)* tilted at a certain angle *θ*, *ii)* passing from the centre of the picture, *iii)* connecting two opposite sides of the picture, and *iv)* shifted from the centre by a number of pixels, *s*.

Figure 6-1b and Figure 6-1c show examples of two profiles: one defined for $\theta = \theta_1$ and one for $\theta = \theta_2$, respectively. Two cases can be identified based on θ as follows:

1. $tan^{-1}\frac{M}{N} < \vartheta < \pi - tan^{-1}\frac{M}{N}$ means that the two connected sides are parallel to the x axis, as in Figure 6-1b and Figure 6-1d.
2. $\theta < tan^{-1}\frac{M}{N}$ or $\theta > \pi - tan^{-1}\frac{M}{N}$ means that the two connected sides are parallel to the y axis, as in Figure 6-1c and Figure 6-1e.

In the first case (Figure 6-1b), the image is shifted along the y axis (Figure 6-1e), while in the second case (Figure 6-1c), the image picture is shifted along the x axis (Figure 6-1d).

The PSD of *p(θ,s)* is defined by

$$\boldsymbol{PSD_{p(\theta,s)} = \frac{1}{L\Delta x}|FFT(p(\theta,s))|^2} \qquad \textit{(6.1)}$$

where *L* is the number of pixels of *p(θ,s)* and *Δx* is the pixel size.

If *s*=0, this means that the profile is acquired without shifting the image, and the PSD is the classical value calculated previously in various papers [115] and discussed in Section 2.4.4.4. In the method which follows, PSD is calculated by keeping the angle constant but shifting the SEM image. Then, the average PSD is calculated at a fixed angle over a certain number of shifted images by:

$$\boldsymbol{PSD_{p(\theta)} = \frac{\sum_{NS}^{i=1} PSD_{p(\theta,s_i)}}{NS}} \qquad \textit{(6.2)}$$

where *NS* is the number of shifted images.

To have a factor that can evaluate the amount of the LIPSS over a certain area but at the same time have a factor that considers the LIPSS orientation, $PSD_{p(\theta)}$ is required. Indeed, the measure of the crater size is not sufficient because the LIPSS could not cover the entire surface of the crater. Moreover, because LIPSS evolve in periodicity by increasing the number of pulses, the resulting surface crater could be covered by LIPSS with different periodicity, and this effect needs to be distinguished from a crater covered by LIPSS with a single periodicity. Then, it is fundamental to associate the amount of the area affected by the periodic structure to the periodicity of these structures [75]. Furthermore, LIPSS are not only changing in periodicity, but they are also affected by an erasure effect [105]. Figure 6-2 shows an example of this evolution: in Figure 6-2a, LIPSS are covering almost all the crater surface; in Figure 6-2b, LIPSS start to change from the centre of the crater surface to the edges; in Figure 6-2c, LIPSS are limited only to the edge of the crater surface, while in the centre are bigger and less periodic structures. By $PSD_{p(\theta)}$, it is possible to quantify the amount of surface affected by structures with certain periodicity and oriented in certain directions. This method gives similar results to the 2DFFT method but allows better management of the 1D data because they can be associated to 1D PSD and then to 1D profile.

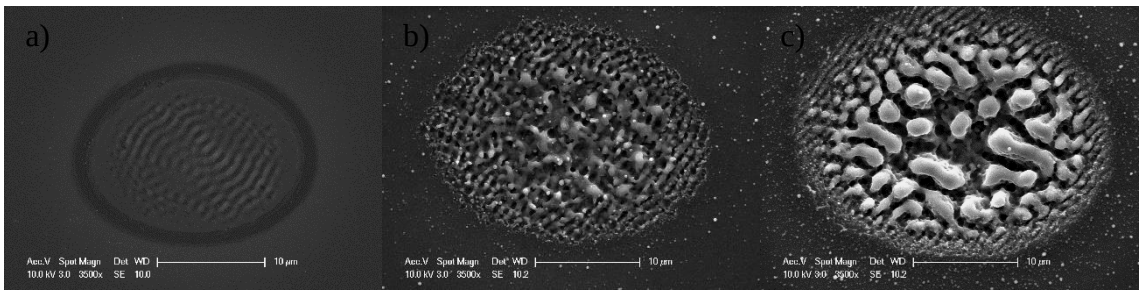

Figure 6-2 LIPSS generated at 0.82 J/cm^2 with circular polarisation on Si <100> with a) 2 pulses; b) 12 pulses; c) 55 pulses

Calculation of the $PSD_{(\theta)}$ for all the angles from 0 to π gives a complete description of the PSD intensity. Figure 6-3 shows how every crater was analysed. Figure 6-3a shows the crater imported in Matlab and the selected area. Figure 6-3b shows in a single chart the scatter plots of all the PSD(θ) from 0 to π. The colours are associated with the angles using a colourmap that varies from red to yellow: the red points correspond to PSD(θ) with θ close to 0º or 180º. The yellow points correspond to PSD(θ) with θ close to 90º. In Figure 6-3b, a visible peak with a value around 1700 pixel^{2}µm corresponding to an x coordinate around $\Delta x = 1$ µm^{-1} (the exact value is 1.172 µm^{-1}) is noticed. This indicates that the structures with a periodicity around 1 µm^{-1} were those covering the majority of

the area of the corresponding image (Figure 6-3a). As mentioned previously, the points in red colour indicate that the angle is close to 0º or 180º. In fact, LIPSS were almost parallel to the y axis, and the higher PSD(θ) was expected for a value rotated at 90º compared to the LIPSS orientation and then around 0º or 180º. The exact value of the peak angle is easily achievable (in this case it is 23º; the LIPSS seems slightly counter-clockwise rotated compared to the y axis). It is then possible to find the peak for all the LIPSS produced by evaluating the area affected and its corresponding periodicity and angle.

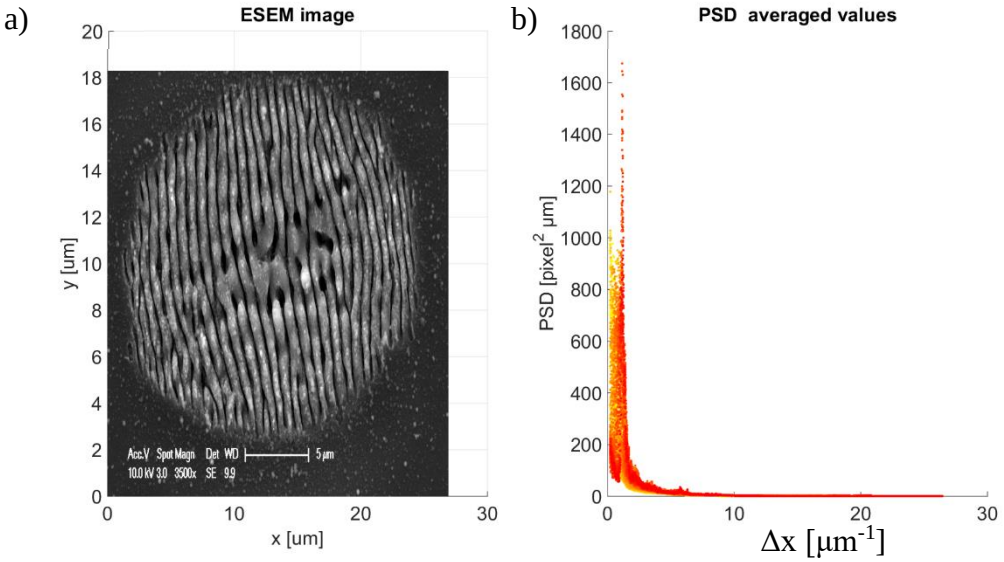

Figure 6-3 Example of the method used to study LIPSS: a) ESEM image obtained on Si <100> at 0.069 J/cm^2 with 200 pulses; b) PSD(θ) scattered for all the angles. The colour of the point goes from red to yellow (red: θ close to 0º or 180º; yellow: θ close to 90º).

6.2.2 Depth data acquisition and Matlab post-processing

The data acquisition for this section is the same as shown in Section 4.3, so it is not reported here again. However, the Matlab post-processing is different, so it is reported here (Figure 6-4). The data were imported in Matlab in the matrix of the crater, as shown in Figure 4-3, but the analysis of the depth was performed crater by crater.

For each crater, the centroid was identified by the centre of mass. The identification of the centre of mass is fundamental, particularly for a crater with a high roughness on the bottom. Setting the centre of mass at the point (0,0), four profiles at different locations (x=0, y=0, x=y, and x=-y) were extracted for each crater. The profiles were obtained by

averaging the three closest lines to the functions defined previously. Then, for each crater four profiles were obtained: in the case of a smooth crater surface, the depth of each profile was the same, but for a very irregular crater surface, the depth could differ because the minimum of the crater did not always correspond to the centroid point. The final depth of the crater was obtained by the average of six craters (in total, 24 profiles).

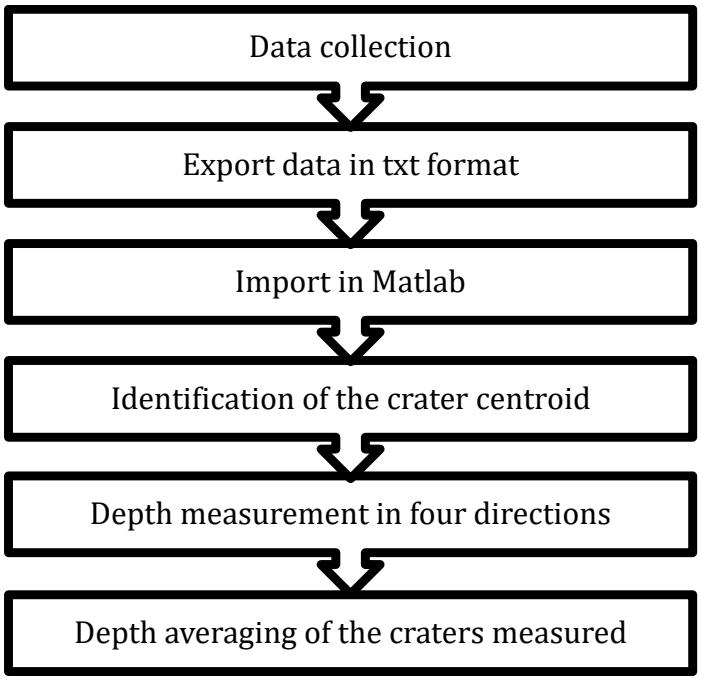

Figure 6-4 Schematic flow for the depth calculation process

6.3 Results and discussion

6.3.1 Polarisation effects on LIPSS periodicity

Before showing the results of the effects of polarisation on LIPSS periodicity obtained by PSD post-processing, two example using two pictures (Figure 6-5) chosen from all the SEM pictures analysed for each combination described in Table 6-2 are described. This will introduce the reader to the results explained in the next sections.

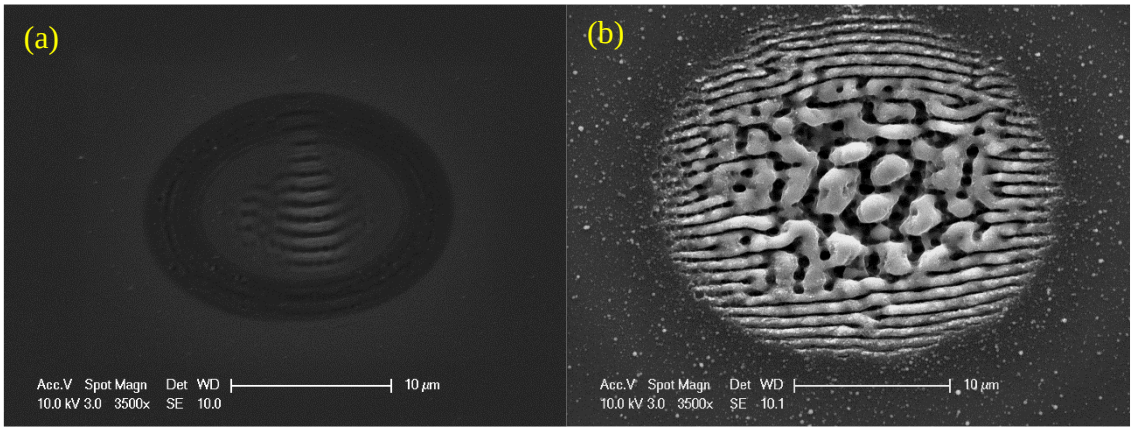

Figure 6-5 SEM images of LIPSS obtained using perpendicular polarisation at 0.56 J/cm^2 with a) three pulses and b) 55 pulses, respectively.

Figure 6-5a and Figure 6-5b show the LIPSS obtained using a fluence above the single pulse ablation threshold with 3 and 55 pulses, respectively, using perpendicular polarisation. These two images were selected because the LIPSS analysis was more difficult compare to other cases. In both cases, there was the presence of LIPSS, but they were in different regions of the crater and with different intensities. In Figure 6-5a, it was possible to identify only a single type of structure. These structures were the classical LIPSS obtained with a low number of pulses using a fluence above the single pulse ablation threshold. Figure 6-5b shows two kinds of structures: LIPSS around the edge and columns in the crater centre, as already remarked on in a published paper as due to particle nucleation [152]. It is evident that the LIPSS around the edge were the periodic structures with the highest contribution in the domain of the Fourier transform because the structures in the centre did not have a strong periodicity. These two pictures are representative of the cases illustrating when the method developed in Section 6.2.1 is fundamental to a good analysis of LIPSS. For example, by the method developed, it is possible to obtain the periodicity of the dominant structure (e.g. for Figure 6-5a it is 0.959 μm, while for Figure 6-5b it is 0.820 μm) and the direction of the dominant structure.

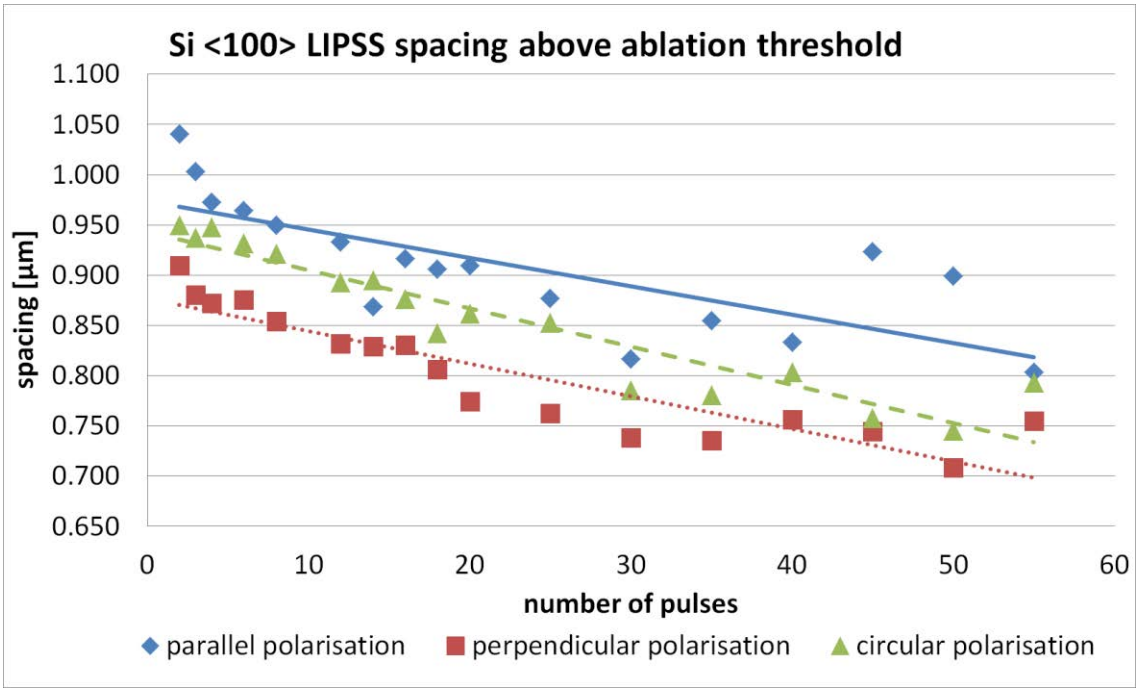

Figure 6-6 LIPSS spacing for LIPSS generated at 0.82 J/cm^2 on Si <100> sample in a range between 2 and 55 pulses

The experimental results are split into two regimes: beneath and above the silicon ablation threshold. Figure 6-6 shows the values of the period obtained with fluence (i.e. 0.82 J/cm^2) "above the single ablation threshold" (0.3 J/cm^2) obtained by increasing the number of pulses from 2 to 55 for the three polarisations. The craters made with the three polarisations each show a different LIPSS spacing. Each presents a decreasing trend by increasing the number of pulses, but they are shifted along the y axis. The bigger values are for the parallel polarisation, middle values are for circular polarisation, and smaller values are for perpendicular polarisation, respectively. Indeed, the values for parallel polarisation decreased from 1 µm to 0.85 µm, those related to circular polarisation decreased from 0.95 µm to 0.8 µm, and the perpendicular values decreased from 0.9 µm to 0.7 µm. Figure 6-6 confirms that when the number of pulses was increased, the LIPSS period decreased, as demonstrated in other papers [102] regarding the study of the influence of pulses and LIPSS period. This means that the method developed is reliable and can be extended to other analyses as well.

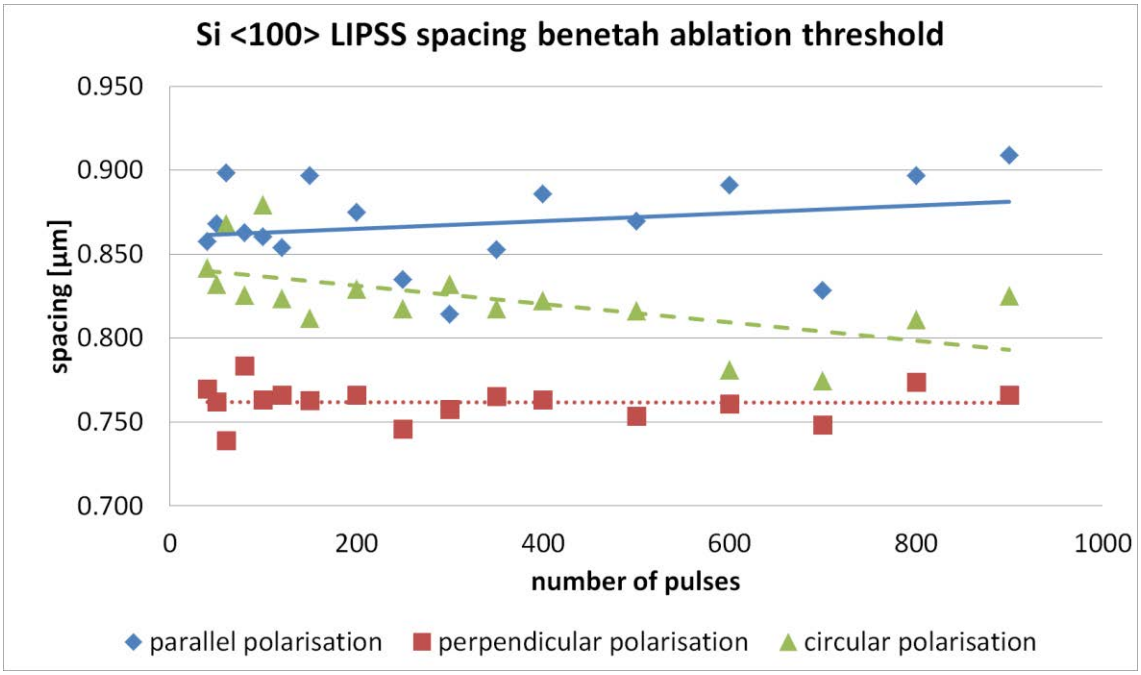

Figure 6-7 LIPSS spacing for LIPSS generated at 0.069 J/cm^2 on Si <100> sample in a range between 40 and 900 pulses

Figure 6-7 shows the values of the LIPSS spacing / period obtained with fluence (i.e. 0.069 J/cm^2) "beneath the single ablation threshold" (i.e. 0.3 J/cm^2), by increasing the number of pulses from 40 to 900 for the three polarisations. The values of the period were almost constant for each polarisation state; however, also in this case one polarisation was shifted along the y axis compared to the other ones. The shift along the y axis is the same as the one for fluence beneath the ablation threshold. In fact, the LIPSS produced using parallel polarisation have the highest period value, followed by those obtained using circular polarisation; the LIPPS generated using perpendicular polarisation have the smallest values. Considering the LIPSS values as almost periodic for each polarisation state, it was possible to calculate the average and the standard deviation values. The resulting values are 0.868, 0.824, and 0.759 with a standard deviation of 0.025, 0.024, and 0.010 for parallel, circular, and perpendicular polarisation, respectively. The same trend, were obtained with the other two fluences investigated, one beneath the single pulse ablation threshold (0.076 J/cm^2) and the other above it (0.56 J/cm^2).

The dependence of LIPSS periodicity on polarisation state has previously been unnoticed. In a recent paper [111], the enhancement of generation of LIPSS when the polarisation state was aligned with a particular lattice axis was demonstrated. The alignment between the polarisation state direction and the lattice enhances the ionisation

effect because of the effective electron mass. The effective electron mass is a quantity that depends on the crystal structure. This means that, depending on the coupling between the polarisation state and the crystal structure, the ionisation effect is different, and the amount of promoted electrons is different, as well.

It is possible to use the Drude model to relate the number of electrons to the dielectric constant in a semiconductor by [62]

$$\boldsymbol{\varepsilon' = 1 + (\varepsilon_g - 1)\left(1 - \frac{n_e}{n_0}\right) - \frac{n_e e^2}{\varepsilon_d m_e}\frac{1}{1 + i\nu_c/w}} \qquad \textit{(6.3)}$$

where ε' is the material dielectric constant, ε_g is the dielectric constant of unexcited material, n_e is the electron number density, n_0 is the valence band electron density, ε_d is the dielectric constant of the air, m_e is the mass of electrons, ν_c is the collision frequency, and w is the laser frequency.

Equation 6.3 shows how, by increasing the number of electrons, the dielectric constant can be increased. At the same time, the dielectric constant is related to the wavelength used to define the module of the wave vector of the surface plasmons (λ_s) and to the LIPSS periodicity (Λ) in normal incidence of the laser beam by [97]

$$\boldsymbol{\Lambda = \lambda_s = \lambda\sqrt{\left(\frac{\varepsilon' + \varepsilon_d}{\varepsilon'\varepsilon_d}\right)}} \qquad \textit{(6.4)}$$

where λ is the laser wavelength.

It comes directly from Eq. 6.4) that if the silicon dielectric constant increases, the module of the wave vector of the surface plasmons decreases, and then the LIPSS periodicity decreases.

In other words, the relation between the polarisation state and the LIPSS period identified can be explained by the coupling between the polarisation state and the crystal structure. Indeed, the crystal structure can enhance the promotion of electrons that drives an increase of the dielectric constant. Then, a decrease of the dielectric constant drives a decrease of LIPSS periodicity. Thus, the LIPSS periodicity could depend on the polarisation state.

6.3.2 Polarisation effects on LIPSS formation amount

In the previous section, the effect of polarisation on LIPSS periodicity was discussed. In this section, the polarisation state effects on the LIPSS amount by using the method described in Section 6.2.1 will be discussed. The method developed allows the possibility to quantify the amount of periodic structure with a certain periodicity that are generated over an area by using the $PSD_{p(\theta)}$ value. There was an attempt that the LIPSS amount was evaluated and the affected area parameter was used [111]. The area ellipse containing the LIPSS was visually identified and then the area of the ellipse was calculated. However, measuring the affected area can be difficult in certain cases: for instance, when more than one structure type is generated over the crater.

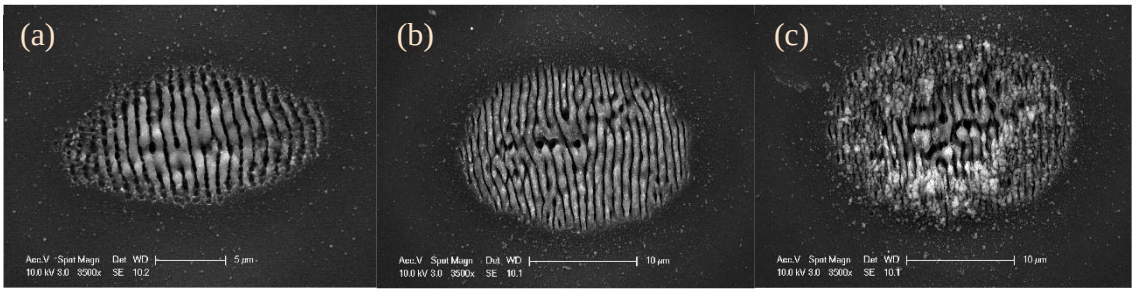

Figure 6-8 LIPSS obtained with parallel polarisation using 0.069 J/cm^2 on Si <100> with a) 40, b) 200, and c) 900 pulses, respectively

The following is a preliminary example to clarify how the method works and to explain the interpretation of the results reported in this section. Figure 6-8 shows three cases of LIPSS formation via parallel polarisation on Si <100> at 0.069 J/cm^2 using 40 pulses, 200 pulses, and 900 pulses, respectively. The area affected in Figure 6-8a has a non-standard shape, similar to an elongated ellipse. Moreover, the LIPSS generated on the left and right side of the elongated ellipse are different from the ones generated in the centre. In this case, by the application of the PSD method, the maximum value of PSD is 1058 μm, with a period of 0.858 μm at 9º. Figure 6-8b shows LIPSS formation with a classical elongated shape [90]; however, in the centre of the crater LIPSS are not consistently distributed. By the application of the PSD method, the resulting maximum value of the PSD is 1280 μm; it was obtained at 169º with a period of 0.875. Figure 6-8c shows a high amount of debris due to the high number of pulses involved. Moreover, two different structures are visible, one in the crater centre and the other close to the edge. By the application of the PSD method, the max value of the PSD associated with this image is 517 μm at 155º with a period of 0.909. It is clear that using the PSD, it is

possible to identify the amount of the periodic structure that covers the affected area and correlate it to a certain LIPSS period and orientation.

Figure 6-9 shows the maximum value of the PSD obtained using a fluence (0.56 J/cm^2) above the "single pulse ablation threshold" and with a number of pulses between 2 and 55. For all three polarisations, the craters generated with less than 5 pulses do not present a periodic structure, and the maximum PSD value are about 0.

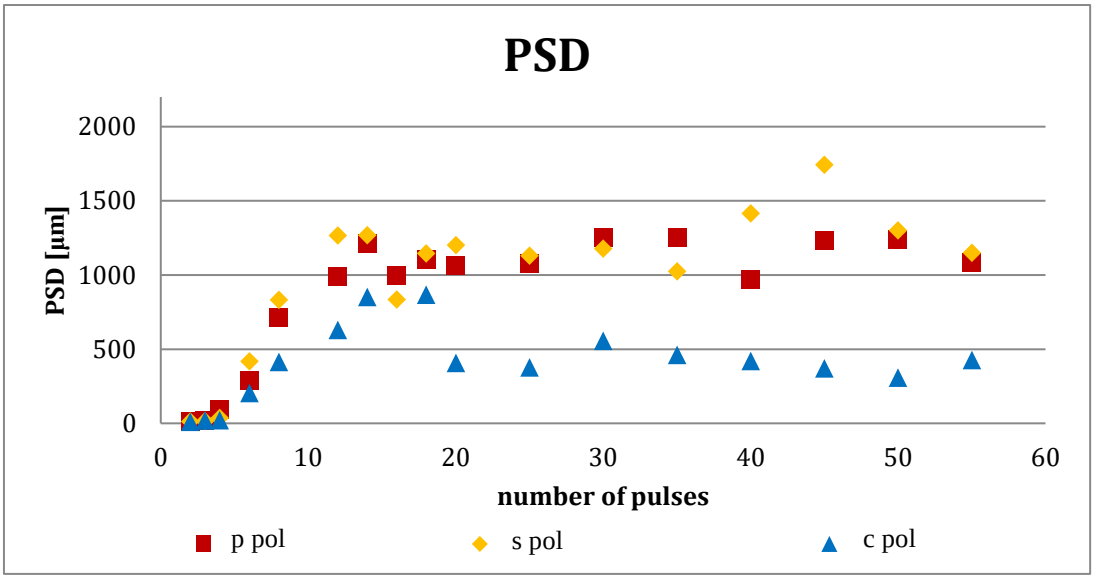

Figure 6-9 LIPSS PSD generated at 0.56 J/cm^2 on Si <100> sample in a range between 2 and 55 pulses

For the two linear polarisation states, the increase of the PSD values is similar; for the circular polarisation, the increase is slower. The maximum PSD value for the circular polarisation is less than 1000 μm at 18 pulses, and the value decreases up to 500 μm and remains almost constant up to 55 pulses. The two linear polarisations show a similar

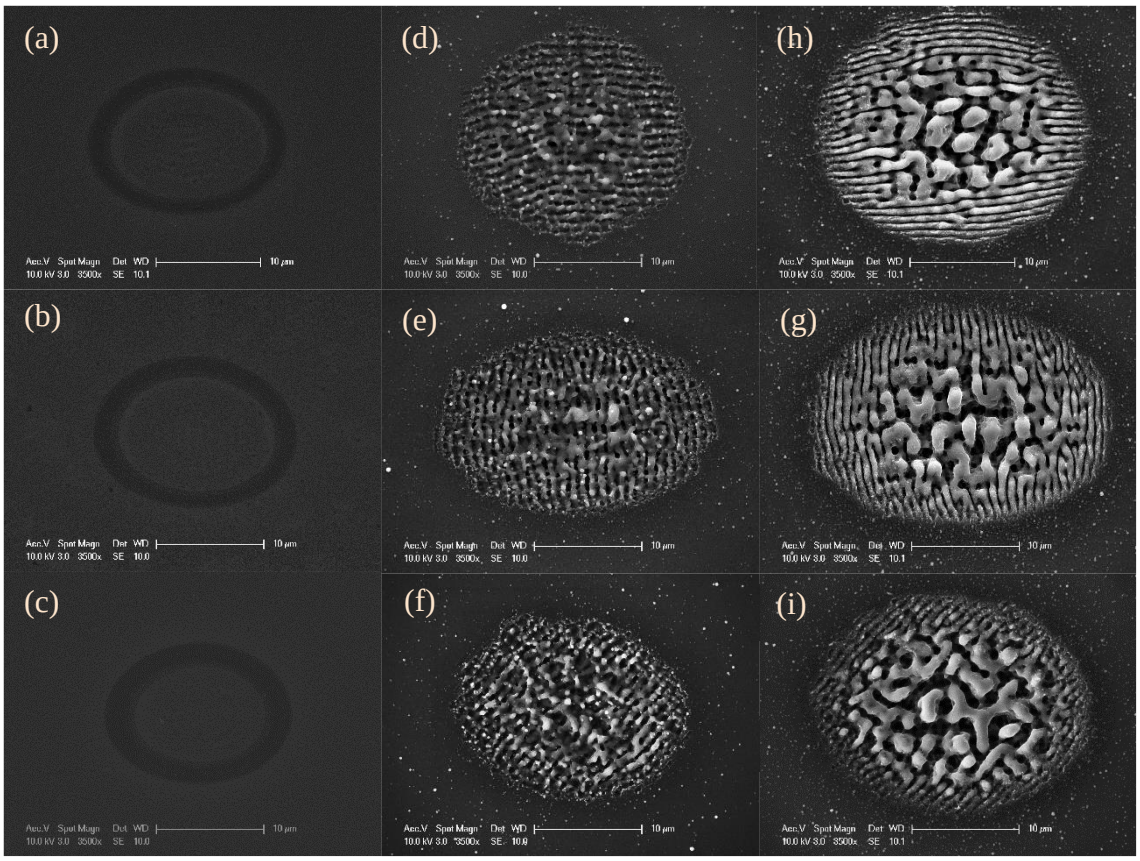

Figure 6-10 SEM image of affected area at 0.56 J/cm^2 with 2 pulses (a,b,c), 14 pulses (d,e,f), and 55 pulses (h,g,i) with perpendicular (a,d,h), parallel (b,e,g), and circular polarisation (c,f,i)

trend. In fact, the PSD values increase linearly up to 1500 μm and then remain almost constant for both polarisation states. The fact that the PSD values do not increase over a certain number of pulses can be explained by the nucleation phenomenon that starts in the centre of the crater. Despite the increasing size of the crater area, the LIPSS amount does not increase because the periodic structures created on the edge of the crater are compensated by the pillars generated in the centre of the crater.

Figure 6-10 shows the SEM images of the laser affected area produced on Si <100> at 0.56 J/cm^2 with 2 pulses (a,b,c), 14 pulses (d,e,f), and 55 pulses (h,g,i) with different polarisation: first row – perpendicular, second row – parallel, and third row – circular. Using 2 pulses, there was no generation of LIPSS for any of the polarisation states used.

LIPSS were produced with 14 pulses, and they look similar for the three polarisation states (d,e,f). However, upon observing the image in greater detail, it can be seen that the crater shown in Figure 6-10f had less uniform LIPSS than the one in Figure 6-10d and Figure 6-10e. This confirms that the PSD value obtained for circular polarisation was smaller than the PSD values obtained for the two linear (i.e. perpendicular and parallel) polarisations. From the comparison of Figure 6-10d/e/f with Figure 6-10h/g/i it is seen that the affected area produced using 55 pulses was larger than the area produced using 14 pulses. The increasing of the area is followed by the formation of a central pillar and the erasing of LIPSS. This agrees with the fact that the PSD values over 18 pulses remained constant despite the increasing affected area. Indeed, the formation of pillars in the crater centre balanced the formation of more LIPSS on the crater edge.

Using 55 pulses, the LIPSS amount on the edge was found to be greater for the linear polarisations than the circular, creating a sort of larger LIPSS ring around the central pillars. In fact, comparing Figure 6-10h and Figure 6-10g with Figure 6-10i it is seen that the width of the LIPSS ring formed around the central pillars was larger for the linear polarisations than the circular. This behaviour can explain why the PSD values in a regime over the 20 pulses for linear polarisations was about three times bigger than the values obtained for the circular polarisation.

Figure 6-11 shows the PSD values for LIPSS PSD generated at 0.069 J/cm^2 on the Si <100> sample in a range between 40 and 900 pulses. The PSD values for LIPSS obtained by using fluence beneath the ablation threshold showed the same behaviour as the one obtained using fluence above threshold. For 40 pulses, the circular and linear polarisations showed small gap values. Increasing the number of pulses, the gap increased, while the PSD values for circular polarisation remained almost constant around 500 μm, and the PSD values for linear polarisations increase and reach the maximum value (almost 2000 μm) around 400 pulses. Then, the PSD values decreased for both polarisations, and at 900 pulses they were around 1000 μm. Despite the decrease, the linear polarisations did not reach the same value as the circular one, and a certain gap is kept.

To conclude, regarding the amount of LIPSS, in both regimes, above and beneath the ablation threshold, the amount of LIPSS induced using circular polarisation was less than the one induced using linear (for both parallel and perpendicular) polarisations. A similar behaviour was highlighted by generating LIPSS on Si(100) using linear polarisation [111]. In that paper, by rotating the silicon sample along the laser beam

propagation axes and keeping constant the polarisation, it was noticed that the coupling of the polarisation direction with the crystal orientation enhanced LIPSS formation. Comparing those results with the current works, a similar behaviour was obtained by modulating the polarisation state. It was reported that when polarisations were coupled with [011] and $[01\bar{1}]$ crystal axes (x and y Cartesian axes, respectively) the laser affected area was similar [111],. However, when the laser was coupled with the [001] (45º tilted) crystal axis, the affected area was reduced to half values. The LIPSS orientation obtained in the results can be compared with the orientation from that work in the following way: parallel with [011] crystal axis, perpendicular with $[01\bar{1}]$ crystal axis, and circular with [001] axis. Then, the same enhancing was identified in the current work by varying the polarisation. The enhancing of LIPSS when the polarisation is coupled to a certain crystal direction can be attributed to orientation-dependent effective electron mass that modulates ionization rate for different crystal orientations, like what was shown in Section 6.3.1. The results obtained here show that the ionisation effects are the same regarding LIPSS amount for parallel and perpendicular polarisations, but they were different using the circular polarisation.

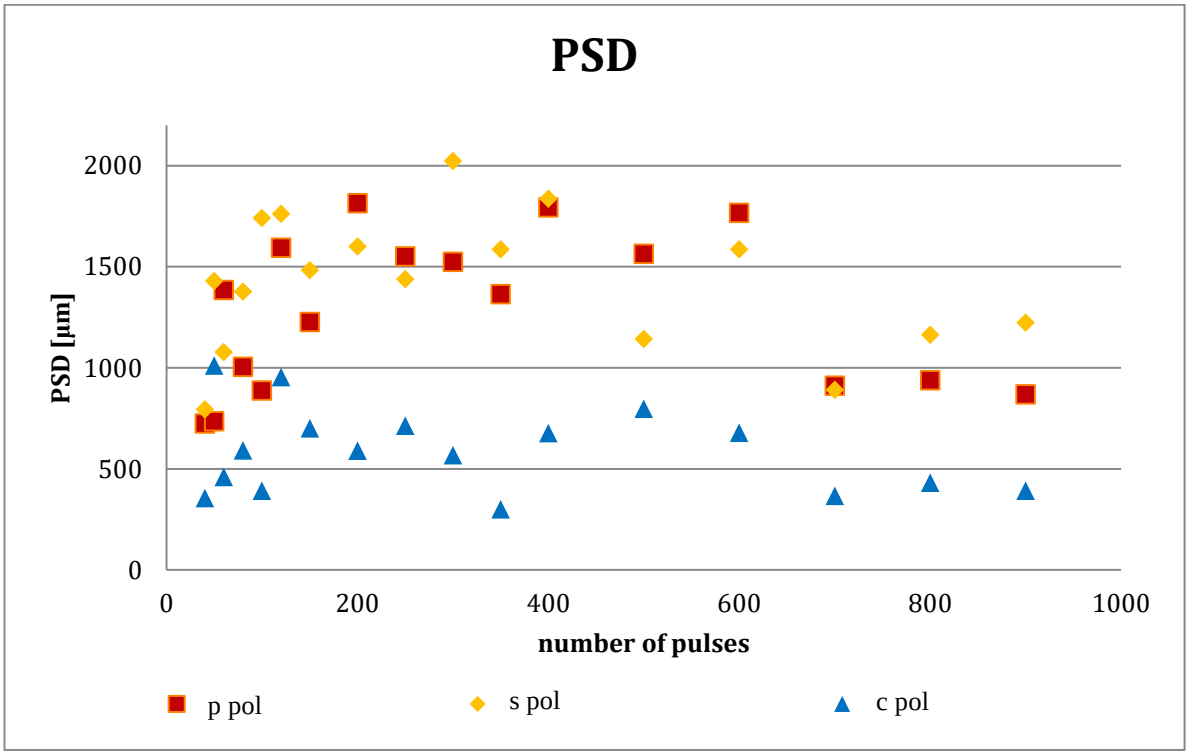

Figure 6-11 LIPSS PSD generated at 0.069 J/cm^2 on Si <100> sample in a range between 40 and 900 pulses

6.3.3 Polarisation effects using a different crystal structure

In the previous sections, the contribution of the crystal structure to enhance the ionisation effect along the directions of certain axes were highlighted. These effects can modulate LIPSS periodicity and the total amount of LIPSS generated over a certain region, thus relating them with the polarisation state. However, based on the periodicity study, it is suggested that the higher number of electrons was promoted by parallel polarisation, followed by circular and then by perpendicular. In the study related to the LIPSS amount, it is found a dependence on LIPSS formation based on the polarisation and it was assumed that it was due to coupling effects with the crystalline structure. The polarisation enhancement effect was not associated with the polarisation state in the same manner.

For this reason, the study of the polarisation effect on LIPSS was extended also to Si(111). Figure 6-12 shows the different crystal direction of Si(100) compare to Si(111).

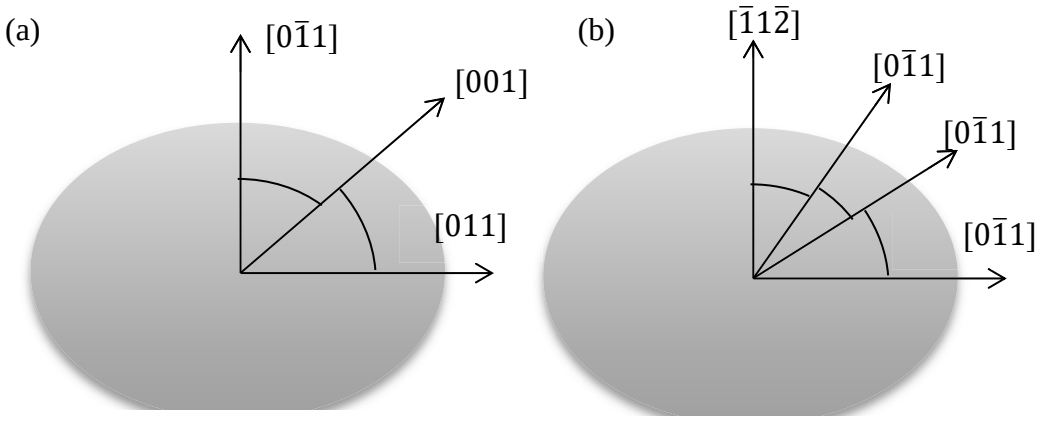

Figure 6-12 Crystal axes directions in the same direction of LIPSS for a) Si(100) and b) Si (111), respectively

The same set of experiments tested for Si(100) was run on Si(111) to better understand any relation between crystal orientation and LIPSS enhancement. Despite the different folding structure and the different crystal directions associated with LIPSS direction, the periodicity did not show any difference. Comparison of the Si(100) with the Si(111) periodicity values showed that they almost overlapped for each polarisation and for both fluence regimes (above and below the single pulse ablation threshold).

As reported in Figure 6-13(a, c, e) using 0.56J/cm^2, the periodicity values obtained in Si(100) and in Si(111) are closer to each other for linear polarisations, Figure 6-13(a, e), than for the circular polarisation, Figure 6-13(c). However, the difference between Si(100) and Si(111) in circular polarisation is not large enough to suppose a different behaviour between the two polarisations.

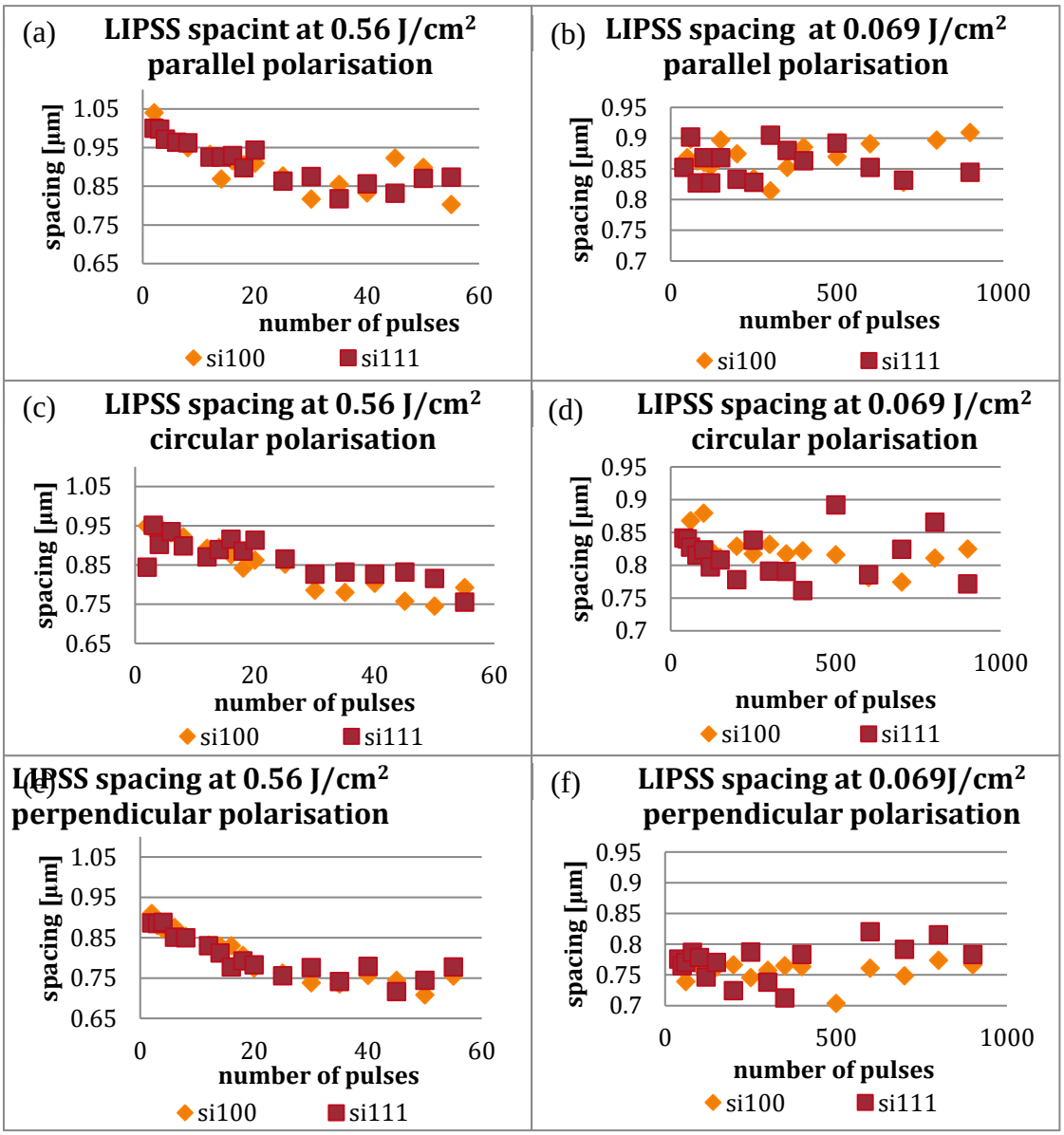

Figure 6-13 Comparison of LIPSS periodicity between Si (100) and Si (111) using parallel (a, b), circular (c, d), and perpendicular polarisation (e, f) at 0.56 J/cm^2 (a, c, e) and 0.069 J/cm^2 (b,d,f)

Figure 6-13(b, d, f) report the results using 0.069 J/cm^2. Again, in this case, there was not a significant difference between the two silicon samples with a different crystal structure. In particular, for the number of pulses less than 500, the results obtained with

the two crystal orientations are similar. As the number of pulses was increased, the difference between the Si(100) and Si(111) was higher, but this was due to high variation of the values obtained. Indeed, assuming the LIPSS period is constant varying the number of pulses, as it was demonstrated for pulse beneath the ablation threshold in Section 6.3.1, and calculating the standard deviation (Table 6-3), it was seen that there was not significant difference between the values. However, it is interesting to note that even LIPSS periodicity on the Si(111) sample depended on the polarisation state in the following way: parallel had the higher period values, perpendicular the smaller, while circular stayed in between, as it was highlighted for Si (100).

Table 6-3 Average and standard deviation of LIPSS spacing generated at 0.069 J/cm^2 in Si(100) and Si(111)

	Si (100)		Si(111)	
	Average	S.D.	Average	S.D.
Parallel	0.868	0.025	0.871	0.041
Circular	0.824	0.024	0.815	0.033
Perpendicular	0.759	0.010	0.768	0.032

6.3.4 Polarisation effects on the crater depth

Because of the difference in LIPSS periodicity amount and periodicity identified in Section 6.3.1 and Section 6.3.2, an investigation on the depth of the crater was conducted. In fact, it is well known that the surface due to LIPSS formation can increase the material linear absorption, principally because of anti-reflection effect induced by the nanostructures [153]. In particular, the structure periodicity variation in the vicinity of the laser wavelength can change the reflection percentage [154]. Thus, if a variation of reflection occurs, it should correspond to a variation of absorption and then of crater depth.

Here, the effect of the three polarisations on the crater depth only for fluence "above the single pulse ablation threshold" was investigated. It is because LIPSS obtained with a fluence "beneath the single ablation threshold" showed a periodic peak to peak value comparable with the maximum crater depth, making the definition of a crater depth difficult.

Figure 6-14 shows the crater depth obtained by varying the fluence between 0.4 and 1.81 J/cm^2 and the number of pulses between 10 and 30. Using 10 pulses (Figure 6-14a), the crater depth decreased almost linearly up to -2 μm. The crater depth values obtained with the perpendicular polarisation were greater than the values obtained with circular polarisation; the circular values were greater than the values obtained with parallel polarisation. This effect is more visible for fluence higher than 1.5 J/cm^2. While the difference between perpendicular and circular polarisation state can be considered relevant because it is greater than the corresponding standard deviation, the difference between circular and parallel cannot for the opposite reason. Similar behaviour was obtained using 20 pulses, but in this case, there was no difference between circular and parallel, and the difference between circular and perpendicular was almost included in their standard deviations. The depth values varied from -2 μm to -6 μm (Figure 6-14b). The behaviours of the three polarisation states were congruent with the periodicity behaviour identified in Section 6.3.1: perpendicular polarisation was the deepest followed by circular and parallel. Indeed, a variation of the reflectance and consequently of the absorption was expected by variating the periodicity [154]. In particular, decreasing the periodicity value in the vicinity of the wavelength could increase the antireflection properties and consequently the absorption of silicon [155]. Then, the inverse relation between the LIPSS periodicity and the crater depth could be due to the increasing of the antireflection property induced by LIPSS.

Using 25 pulses and 30 pulses (Figure 6-14c and Figure 6-14d, respectively), no differences between the three polarisation states were highlighted. Using 25 pulses, the depth values varied from – 2 μm to -8 μm, while using 30 pulses, they varied from -2 μm to -11 μm.

A strong increment of the standard deviation was highlighted for pulses with high fluence (> 1.5 J/cm^2). This effect was more visible for the crater obtained with 30 pulses and those deeper than 10 μm. This is principally due to the limitation in the measurement system: the Alicona microscope was limited to measuring craters that had a ratio diameter/depth close to 2. When the ratio value was close to 2, or even smaller, the microscope was not reliable because several points were not associated to any depth values or the measured values were more than twice the depth of the ones in the same area, revealing an error in the measurement. Using the GT Countour would be difficult for the issues related to the interference generated from the periodic structures; while a contact profilometer would not be able to measure some features because of the angle

and the AFM analysis is not compatible with that crater depth. However, the number of the sample measured are enough to describe the behaviour even for the higher fluence tested.

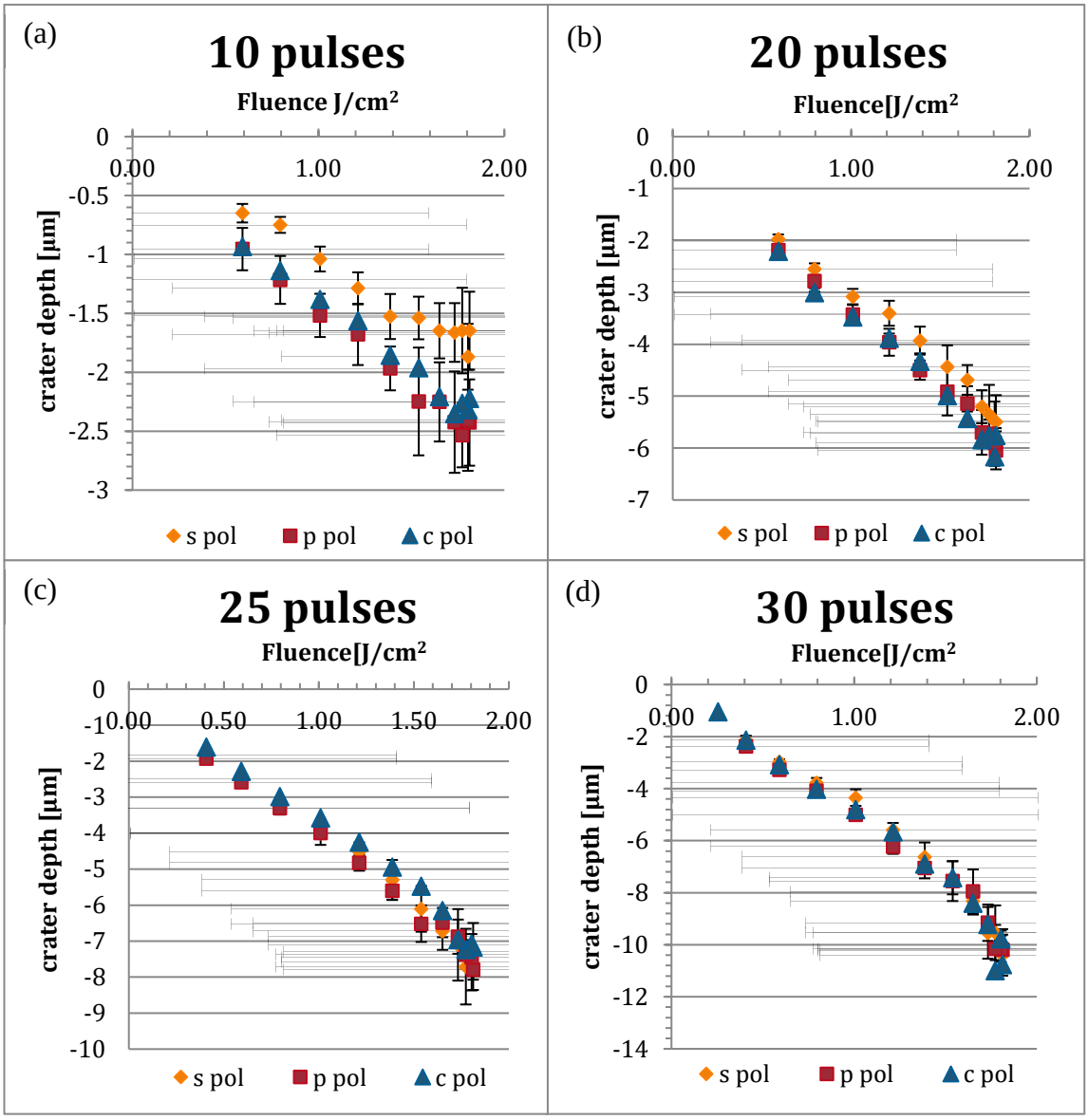

Figure 6-14 Crater depth for perpendicular (s), parallel (p), and circular (c) polarisation for (a) 10, (b) 20, (c) 25, and (d) 30 pulses, respectively.

The study was extended to craters generated with a number of pulses up to 60 (Figure 6-15). As discussed previously, the data reported are limited to craters not deeper than 12 µm because of the low value of the diameter/depth ratio.

For all the cases studied, there were no significant differences between the crater depth values obtained by the craters produced using the three polarisation states.

While the difference in crater depth for a number of pulses lower than 20 could be

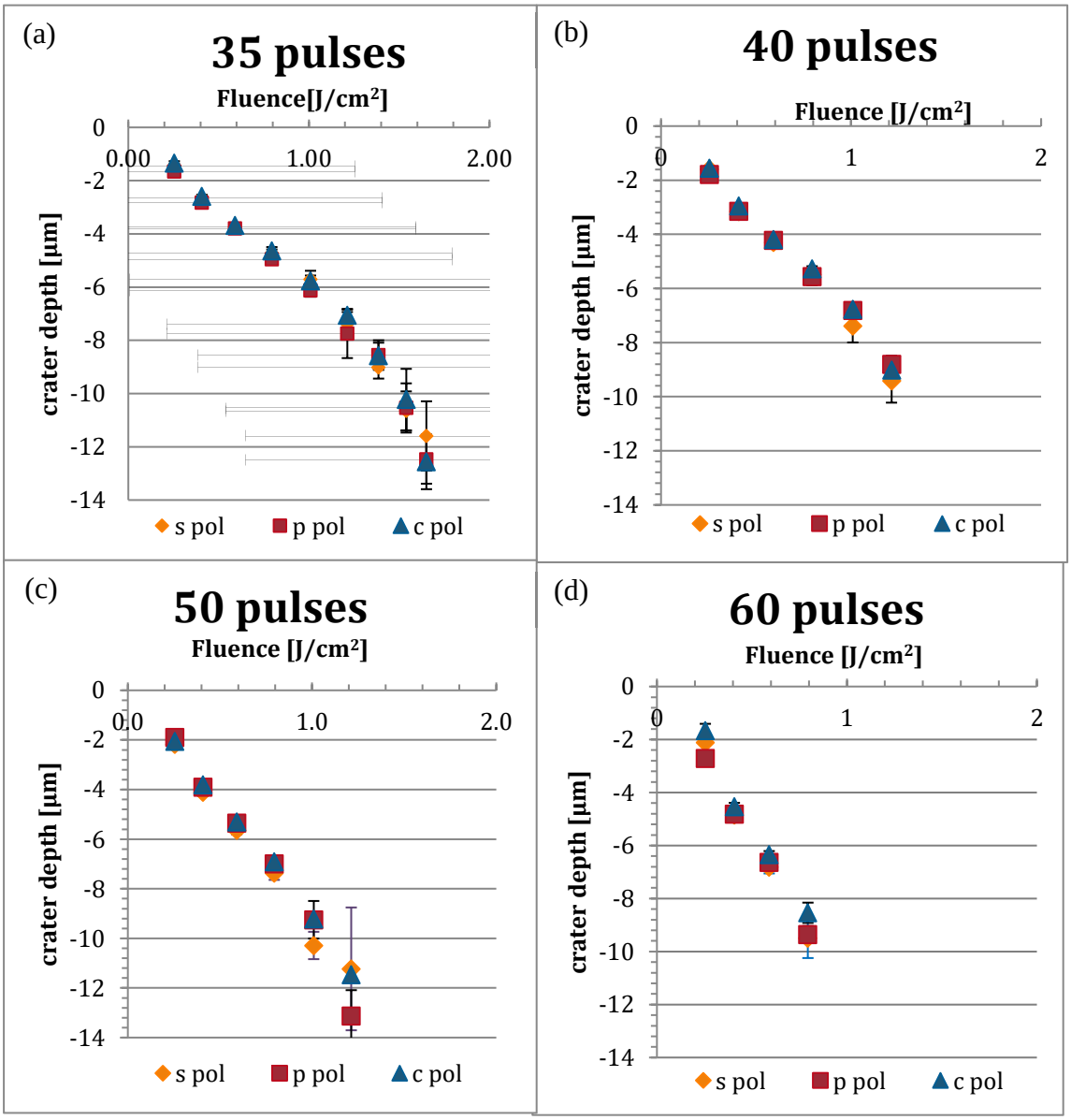

Figure 6-15 Crater depth for perpendicular (s), parallel (p), and circular (c) polarisation for 35 (a), 40 (b), 50 (c), and 60 (d) pulses, respectively.

explained by the periodicity relation obtained in Section 6.3.1, the absence of difference between polarisations for a number of higher pulses could be explained by the results obtained in Section 6.3.2. In fact, it was identified that the LIPSS amount increased up to 20 pulses per crater and then was nearly stable or was decreasing (Figure 6-9). This was due to the formation in the centre of the crater of structures with the shape of cylinder / pillars caused by the nucleation of the ablated particles. From the SEM images, these structure were bigger than the wavelength; however, it was demonstrated

that, structures bigger than 2λ do not influence the reflectance [155]. Moreover, these structures were generated in the crater centre where the majority of the energy was delivered and where the depth was usually measured because it reached the maximum value. LIPSS were distributed only around the edge where a small part of the energy was delivered, and this energy did not contribute to the final crater depth. Then, the generation of pillars instead of LIPSS could be the major cause for the similar depth obtained between different polarisation after 20 pulses.

6.4 Conclusion

This chapter provided an exploration of the effects of varying the polarisation (parallel, perpendicular, and circular) states on a silicon sample. A study on the LIPSS periodicity and formation was conducted by varying the number of pulses for two fluence regimes: beneath and above the single pulse ablation threshold. Moreover, the crater depth for fluence above the single pulse ablation threshold was evaluated by varying the number of pulses for the three polarisation states.

The main findings of this work are summarised as follows:

1. A method based on the PSD was developed to evaluate the periodicity and the amount of LIPSS. Starting from the ESEM images, the PSD of the image profile was evaluated. By the image shifting, several parallel PSD were collected to obtain an average PSD over a certain area of a profile, tilted at a certain angle. Repeating this process from 0 to π, it was possible to have a complete set of PSD values of the entire area analysed. This method allowed identification of LIPSS characteristics such as the periodicity or the LIPSS amount over a certain area. The identification of these characteristics was essential for further findings. Moreover, the method gives some additional information (such as the LIPSS direction) that can be applied to further investigations.
2. In addition to the classical relation between LIPSS direction and laser polarisation, it was identified that the polarisation state can also affect the LIPSS periodicity. Indeed, parallel polarisation LIPSS showed a higher period, followed by the period using circular polarisation; the period produced using perpendicular polarisation showed the smallest value. This behaviour was confirmed on both fluence regimes investigated beneath and above the single pulse ablation threshold: i) beneath the single pulse ablation threshold, the periodicity was almost constant when varying the number of pulses; ii) above

the single ablation threshold, the periodicity decreased by increasing the number of pulses. The LIPSS periodicity variation caused by different polarisation states was believed to be correlated to different ionisation levels which occurred depending on the polarisation coupling with the crystal direction. Because of the ionisation dependency on polarisation; also, the electron number was a factor of polarisation and consequently the refractive index. Because the periodicity is based on the refractive index, it was possible to assume that the polarisation state could contribute to the final LIPSS periodicity.

3. It was demonstrated that the amount of LIPSS over a certain area depends on the polarisation state. By applying the method developed based on the PSD, it was possible to evaluate the amount of the periodic structure based on the periodicity and the orientation angle. It was identified that linear polarisation states drive a higher amount of LIPSS compared to the circular ones in both the regimes investigated, above and beneath the single pulse ablation threshold. For both regimes, with a low and high number of pulses, the amount of LIPSS of circular polarisation was lower than the linear polarisation states. This behaviour was in accord with the polarisation dependence and can be explained by the effective electron mass and the coupling between the polarisation state and the crystal orientation.
4. From the crater shape point of view, it was noticed that for fluence above the single pulse ablation threshold and for a number of pulses lower than 20, the crater depth was dependent on the polarisation state. Indeed, the crater depth produced by using circular polarisation was deeper than the one produced via perpendicular polarisation; the one made by parallel polarisation was the deepest. The LIPSS amount obtained in the study could explain the fact that crater depth produced with more 20 pulses was not affected by polarisation dependence. Indeed, it was highlighted that, when using more than 20 pulses, the LIPSS amount did not increase and later decreased because of an erasing effect caused by nucleation. The new structure generated instead of LIPSS had a higher periodicity. Structures with higher periods than the laser wavelength do not affect the reflectance. Then, if the reflectance did not change, neither the energy absorbed, nor the crater depth obtained were affected by the polarisation state.

7 OVERALL DISCUSSION, CONTRIBUTIONS, CONCLUSIONS, AND FUTURE WORK

This chapter highlights the contributions achieved by the work conducted in each chapter. Moreover, overall conclusions are reported as well as future work suggested that can begin from the achievements of this thesis.

7.1 Overall discussion and contributions

The contributions of this research are presented in the following subsections, representing the chapter from 4 to 6 .

7.1.1 Effects of pulse duration on 3D crater shape

A systematic study on the 3D crater shape was performed to define the relation between the pulse duration and 3D crater shape. The proposed study did not only consider the usual characteristics that are involved in the laser material ablation analysis, but also focused on the 3D crater shape. Because of the high relevance of the thermal effects on laser ablation, to quantify the thermal effects present in the laser ablation for each pulse

regime studied, the 3D crater shape was compared with two functions. The main outcomes and contributions of this study were:

- The results suggested that the paraboloid function could be applied for pulse durations that were shorter than the photon-phonon coupling time, while the ellipsoid function could be applied for pulse durations that were longer. From the modelling point of view, the knowledge of which of the two functions better approximates the experimental crater shape contributes on a better prediction of the final crater. Indeed, the application of the thermal function or the non-thermal function considering the pulse regime can reduce the error on crater shape prediction.
- The thermal effects are typically evaluated by examining crater characteristics such as re-deposition, HAZ, and debris inside and around the crater. Using the two functions developed and comparing them with the 3D shape of the experimental craters, a method capable of quantifying the amount of the thermal effects by using a single parameter (PD) has been developed for the first time. From the analysis technique point of view the method provides the opportunity to identify and quantify the amount of thermal effect providing a powerful alternative to the conventional analysis techniques, such as SEM or AFM, that are usually used but are more expensive and slower.
- The systematic study, in addition to dependence on the pulse duration, highlighted a strong dependence on fluence, particularly for ps and ns pulses. Combining all the dependences a whole picture about the quantification of the thermal effects on the 3D crater shape in a wide range of pulse durations (from femtosecond to microsecond regime) together with the fluence is provided extending the information on the ablated crater morphology.

7.1.2 Extension of the thermal and non-thermal function to a round and a flat-top energy beam distribution

It is commonly accepted that by using an energy beam shaper, the corresponding generated crater shape matches the energy beam distribution applied. However, in Section 4, it was highlighted that, starting from a Gaussian energy beam distribution, for pulses over 220 ns, the crater shape could be better approximated using an ellipsoid function rather than a paraboloid one. Then, the study was extended using a round and a square flat-top energy beam distributions to understand if a different energy beam

distribution could reduce the impact of thermal effects on the final crater shape. The main outcomes and contributions of this study are:

- By the method developed it was verified whether the crater shape was keeping the original energy beam distribution shape or if it was better approximated by the ellipsoid function. It was highlighted how the crater shape can be modified by the heat diffusion despite using a DOE to change the energy beam distribution. The benefit of this method is that by its application it possible to identify when the integration of a DOE in a laser system has a real effect on the final crater morphology or when despite DOE integration the thermal effects drive the crater ablated morphology.
- The experiments demonstrated that the craters generated via the square flat-top energy beam distribution were less modified by the thermal diffusion compare to the craters obtained using the round flat-top energy beam distribution. From the modelling point of view, this relation can be used to improve the prediction of the crater shape introducing an ellipsoid function for round flat top energy beam distribution over a certain fluence and pulse duration while keeping the square flat top crater shape even in a strong thermal regime as the one tested.

7.1.3 Effect of polarisation on ultrafast laser ablation: LIPSS threshold formation, LIPSS periodicity, and crater depth

Laser polarisation is not generally considered during laser material processing, if the laser beam hits the sample surface orthogonally. But the polarisation can affect the linear absorption, as well defined by Snell's law, when the beam is not orthogonal to the surface. In addition, the polarisation can strongly affect the morphology of the laser crater in the ultrafast ablation regime by inducing surface structures called LIPSS. Moreover, the presence of surface structures can change the final 3D crater shape. In Section 6.3, various novel relations between polarisation and LIPSS and consequently on the crater depth were identified. The main contributions and outcomes of this chapter are:

- A method based on PSD to analyse the LIPSS periodicity and the LIPSS amount over a certain area starting from the ESEM image of LIPSS was developed. The method offers the capability to distinguish between structures with different periodicity and surface with different amount of LIPSS. In addition to periodicity and amount, the method could reveal even the LIPSS orientation.

Differently from the methods previously developed from other groups it allows a wide LIPSS analysis that does not depend on the human interaction (e.g. profile selection, affected area identification).

- A new relation between LIPSS periodicity and polarisation was found. This increases the knowledge on LIPSS formation describing the role of polarisation on LIPSS periodicity. Indeed, in addition to fluence and wavelength, LIPSS periodicity depends on the polarisation and different periodicity values for parallel, perpendicular and circular polarisation were demonstrated. It was identified that LIPSS produced with parallel polarisation had the higher period value, followed by the ones produced with circular polarisation, while the LIPSS with the smallest period was the one produced using perpendicular polarisation.
- By application of the new method developed, the polarisation role on the total amount of LIPSS that affected the crater surface was clarified. This relation gives an additional information about the effect of polarisation on crater morphology when LIPSS are generated and described another way how polarisation can drive the crater morphology.
- The indirect contribution of the polarisation states on the crater depth was revealed. It was identified the opportunity to modulate the crater depth indirectly by acting directly on the polarisation which drives the LIPSS amount. Indeed, it was noticed that, using a regime above the ablation threshold, for a number of pulses lower than 20, the deepest craters were produced with parallel polarisation, shallowest with perpendicular polarisation.

7.2 Overall conclusions

The overall objectives identified in Section 1.2 were to bridge the gap between the laser beam parameter and the ablated crater morphology providing suitable outcome for an engineering environment. By studying three laser parameters (pulse duration, energy beam distribution, and polarisation state), simplified functions and relations were defined that can be implemented in the engineering model, even if they incorporate laser beam characteristics strongly related to physics. To accomplish this aim, the following research tasks and findings were achieved:

1) Two functions to approximate the crater shape that were based on the pulse duration were developed. It was experimentally confirmed that the two equations can be used for two different pulse regimes, one for non-thermal

ablation and one for thermal ablation. It was demonstrated that the two functions can be applied to identify thermal or non-thermal processes by the analysis of the crater shape using the PD based method (Section 4).

2) It was experimentally demonstrated that the capability to reduce the thermal effect on the crater shape depends on the energy beam distribution. In fact, measuring the thermal effects on the experimental crater shape by applying the PD based method revealed that the crater shapes generated by a square flat-top energy beam distribution were less thermally affected (around the 30%) than the ones generated with a round flat-top energy beam distribution (Section 5).
3) The effect of polarisation was studied in the nonlinear absorption regime. To better evaluate the effects of polarisation on LIPSS, a new method was developed based on the PSD. Using the method, the dependence on polarisation state of LIPSS periodicity and total amount over the affected area were established. Moreover, the creation of structures of different periodicity was related to the different crater depths experimentally measured, highlighting the effect of enhancing absorption of polarisation state because of LIPSS (Section 6).

The results provide sufficient evidence that the gap between the laser beam parameter and the ablated crater morphology was bridged by studying three laser beam characteristics and providing suitable outcomes for the engineering environment. Specifically, the effects of the pulse duration, the energy beam shape, and the polarisation state were exploited, providing new functions, relations and methods that can be directly or indirectly applied.

7.3 Further work

The gap between the physics and the engineering approach was reduced by the results of this study. However, some topics for future work were identified.

7.3.1 Implementation of functions and relations on STEEP platform

As described at the beginning of this work, this thesis was developed in the STEEP context. STEEP is a Marie Curie project with the final objective to implement a platform capable of modelling three different energy beams (waterjet, laser, and focused ion beam). To reach the objective, the three energy beams were studied independently, but with a focus on obtaining results that could be implemented in the final common

platform. Indeed, the second stage of the STEEP project is to complete the platform by implementing the functions and the relations for the three energy beams investigated from the groups involved in the project.

The function and relations investigated and identified in this thesis can be implemented as follows. The two functions developed in Section 4, one for non-thermal and one for thermal regime, can be implemented in the platform for pulses shorter than the photon-phonon coupling time and for longer pulses, respectively. Moreover, in the case of the implementation of a non-Gaussian energy beam, the capability to maintain the original crater shape identified in Section 5 can be implemented to improve the prediction of the resulting crater shape and the resulting modification due to thermal effects. The effects of polarisation state on crater depth generated on multi-pulse ablation for ultrafast absorption can be implemented in the final platform when generating structures that require more than a single pulse.

7.3.2 Multi-pulse effects on crater shape

In this thesis, only part of a chapter related to a multi-pulse ablation process, while the major investigation was focused on single laser pulse ablation. It was highlighted that for a better understanding and modelling, it is fundamental to understand single-pulse ablation. Moreover, because of the increasing laser applications on thin films and small ablation size required, single laser pulse ablation will play a fundamental role in new laser ablation processes. Consequently, the research focused more on this specific application. In addition to decreasing the process time, the obvious solution is to reduce as much as possible the pulses required for the ablation, up to the single pulse. Thus, single-pulse ablation is becoming increasingly relevant in new applications.

However, multi-process ablation is still used in more classical industry applications, such as cutting and soldering, because of the high material volume involved in these processes. In this process, hundreds or thousands of pulses can be delivered in the same point to achieve the cutting or soldering. In these cases, the equations developed in this thesis could not be applied. The equations developed should be extended to cover multi-pulse processes as well. It is known that multi-pulse processes increase the degree of thermal effect on the material, suggesting that the relation identified for the single laser pulse will evolve in a different way, with different pulse duration thresholds that will be able to distinguish non-thermal from thermal processes. Even the capability to match the original energy beam distribution identified for non-Gaussian energy beam shapes

should be evaluated for a multi-pulse process. In fact, the high thermal impact of a multi-pulse process could change the capability to match the original energy beam distribution identified for the single laser pulse for the square flat-top energy beam distribution.

8 REFERENCES

[1] P. Schaaf, “Introduction,” 2010, 1.

[2] I. W. Boyd and J. I. B. Wilson, *Nature*, 303, 5917, 481, (1983).

[3] K. Kim, J.-Y. Choi, T. Kim, S.-H. Cho, and H.-J. Chung, *Nature*, 479, 7373, 338, (2011).

[4] T. Saga, *NPG Asia Mater.*, 2, 3, 96, (2010).

[5] M. Malinauskas *et al.*, *Light Sci. Appl.*, 5, 8, e16133, (2016).

[6] B. N. Chichkov, C. Momma, S. Nolte, F. Alvensleben, and A. Tünnermann, *Appl. Phys. A Mater. Sci. Process.*, 63, 2, 109, (1996).

[7] G. Račiukatis, *J. Laser Micro/Nanoengineering*, 6, 1, 37, (2011).

[8] J. JJ Nivas *et al.*, *Sci. Rep.*, 5, 17929, (2015).

[9] T. H. R. Crawford, G. A. Botton, and H. K. Haugen, *Appl. Surf. Sci.*, 256, 6, 1749, (2010).

[10] STEEP, “STEEP:A Synergetic Training network on Energy Beam Processing: from modelling to industrial applications,” 2013. [Online]. Available: http://www.steep-itn.eu/.

[11] T. H. MAIMAN, *Nature*, 187, 4736, 493, (1960).

[12] M. S. Brown and C. B. Arnold, “Fundamentals of Laser-Material Interaction and Application to Multiscale Surface Modification,” in *Laser Precision Microfabrication*, K. Sugioka, M. Meunier, and A. Piqué, Eds. Berlin, Heidelberg: Springer Berlin Heidelberg, 2010, 91.

[13] O. Svelto, “Ray and Wave Propagation Through Optical Media,” in *Principles of Lasers*, Boston, MA: Springer US, 2010, 131.

[14] V. S. Letokhov, *Appl. Phys. B Photophysics Laser Chem.*, 46, 3, 237, (1988).

[15] D. von der Linde, K. Sokolowski-Tinten, and J. Bialkowski, *Appl. Surf. Sci.*, 109, 1, (1997).

[16] O. Svelto, “Introductory Concepts,” in *Principles of Lasers*, Boston, MA: Springer US, 2010, 1.

[17] B. E. a. Saleh and M. C. Teich, “Wave Optics,” in *Fundamentals of Photonics*, New York, USA: John Wiley & Sons, Inc., 2007, 38.

[18] B. E. A. Saleh and M. C. Teich, “Statistical Optics,” in *Fundamentals of Photonics*, New York, USA: John Wiley & Sons, Inc., 2007, 403.

[19] A. Sennaroglu, “Lasers,” in *Photonics and laser engineering : principles, devices, and applications*, New York : McGraw-Hill, 2010, 313.

[20] O. Svelto, “Properties of Laser Beams,” in *Principles of Lasers*, Boston, MA: Springer US, 2010, 475.

[21] O. Svelto, “Introductory Concepts,” in *Principles of Lasers*, Boston, MA: Springer US, 2010, 1.

[22] B. E. A. Saleh and M. C. Teich, “Ultrafast optics,” in *Fundamentals of photonics*, Wiley-Interscience, 2007, 936.

[23] B. E. A. Saleh and M. C. Teich, “Semiconductor optics,” in *Fundamental of photonics*, 2007, 627.

[24] B. E. A. Saleh and M. C. Teich, “Semiconductor photon sources,” in *Fundamental of photonics*, 2007, 680.

[25] B. E. A. Saleh and M. C. Teich, “Lasers,” in *Fundamental of photonics*, 2007, 567.

[26] A. Gat *et al.*, *Appl. Phys. Lett.*, 32, 5, 276, (1978).

[27] G. Mannino *et al.*, *Appl. Phys. Lett.*, 97, 2, 22107, (2010).

[28] X. Wang *et al.*, *Appl. Opt.*, 50, 21, 3725, (2011).

[29] A. Gillner *et al.*, *J. Mater. Process. Technol.*, 167, 2, 494, (2005).

[30] X. Cao, M. Jahazi, J. P. Immarigeon, and W. Wallace, *J. Mater. Process. Technol.*, 171, 2, 188, (2006).

[31] E. Akman, A. Demir, T. Canel, and T. Sınmazçelik, *J. Mater. Process. Technol.*, 209, 8, 3705, (2009).

[32] V. T. Swamy, S. Ranganathan, and K. Chattopadhyay, *J. Cryst. Growth*, 96, 3, 628, (1989).

[33] J. H. Yoo, S. H. Jeong, X. L. Mao, R. Greif, and R. E. Russo, *Appl. Phys. Lett.*, 76, 6, 783, (2000).

[34] V. Craciun, N. Bassim, R. K. Singh, D. Craciun, J. Hermann, and C. Boulmer-Leborgne, *Appl. Surf. Sci.*, 186, 1, 288, (2002).

[35] S. T. Hendow and S. A. Shakir, *Opt. Express*, 18, 10, 10188, (2010).

[36] P. Li, D. Lim, and J. Mazumder, *J. Appl. Phys.*, 92, 2, 666, (2002).

[37] M. Milán and J. . Laserna, *Spectrochim. Acta Part B At. Spectrosc.*, 56, 3, 275, (2001).

[38] T. Y. Choi and C. P. Grigoropoulos, *J. Appl. Phys.*, 92, 9, 4918, (2002).

[39] M. S. Rogers, C. P. Grigoropoulos, A. M. Minor, and S. S. Mao, *Appl. Phys.*

Lett., 94, 1, 11111, (2009).

[40] C. G. Morgan, *Reports Prog. Phys.*, 38, 5, 621, (1975).

[41] P. P. Pronko *et al.*, *Phys. Rev. B*, 58, 5, 2387, (1998).

[42] K. Venkatakrishnan, N. Sudani, and B. Tan, *J. Micromechanics Microengineering*, 18, 7, 75032, (2008).

[43] Y. Dong and P. Molian, *Appl. Phys. A Mater. Sci. Process.*, 77, 6, 839, (2003).

[44] G. Miyaji and K. Miyazaki, *Opt. Express*, 16, 20, 16265, (2008).

[45] J. Jandeleit, A. Horn, R. Weichenhain, E. . Kreutz, and R. Poprawe, *Appl. Surf. Sci.*, 127, 885, (1998).

[46] M. Zhao *et al.*, *Sci. Rep.*, 5, 13202, (2015).

[47] D. Stern, R. W. Schoenlein, C. A. Puliafito, E. T. Dobi, R. Birngruber, and J. G. Fujimoto, *Arch. Ophthalmol.*, 107, 4, 710, (1989).

[48] X. Zeng, X. L. Mao, R. Greif, and R. E. Russo, *Appl. Phys. A*, 80, 2, 237, (2005).

[49] V. Zorba, N. Boukos, I. Zergioti, and C. Fotakis, *Appl. Opt.*, 47, 11, 1846, (2008).

[50] M. S. Amer, M. A. El-Ashry, L. R. Dosser, K. E. Hix, J. F. Maguire, and B. Irwin, *Appl. Surf. Sci.*, 242, 1, 162, (2005).

[51] A. Bogaerts, Z. Chen, R. Gijbels, and A. Vertes, *Spectrochim. Acta Part B*, 58, 1867, (2003).

[52] R. Codina, *Comput. Methods Appl. Mech. Eng.*, 156, 1–4, 185, (1998).

[53] S. H. Jeong, R. Greif, and R. E. Russo, *Appl. Surf. Sci.*, 127, 177, (1998).

[54] J. H. Yoo, S. H. Jeong, R. Greif, and R. E. Russo, *J. Appl. Phys.*, 88, 3, 1638, (2000).

[55] S. Buratin and P. Villoresi, *Opt. Mater. Express*, 3, 11, 1925, (2013).

[56] L. Balazs, H. R. Gijbels, and A. Vertes, *Anal. Chem. J.; Wiahtman. R. M. J. Nectroanal. Chem. Anal. Chem. J. Phys . Chem. J. Electroanal. Chem. Interfacial Electrochem. McClave. J. T.; Dietrich, F. H. Stat. J . Am. Chem. SOC*, 63, 112916, 314, (1991).

[57] J. F. READY and J. F. READY, "CHAPTER 5 – Gas Breakdown," in *Effects of High-Power Laser Radiation*, 1971, 213.

[58] S. Amoruso, *Appl. Phys. A Mater. Sci. Process.*, 69, 3, 323, (1999).

[59] J. K. Chen, D. Y. Tzou, and J. E. Beraun, *Int. J. Heat Mass Transf.*, 49, 1, 307, (2006).

[60] B. Wu and Y. C. Shin, *Appl. Surf. Sci.*, 253, 8, 4079, (2007).

[61] A. Gurizzan and P. Villoresi, *Eur. Phys. J. Plus*, 130, 1, 16, (2015).

[62] B. Wu and Y. C. Shin, *Appl. Surf. Sci.*, 255, 9, 4996, (2009).

[63] C. Cheng and X. Xu, *Phys. Rev. B*, 72, 16, 165415, (2005).

[64] J. P. Colombier, P. Combis, F. Bonneau, R. Le Harzic, and E. Audouard, *Phys. Rev. B*, 71, 16, 165406, (2005).

[65] S. E. Imamova, P. A. Atanasov, N. N. Nedialkov, F. Dausinger, and P. Berger, *Nucl. Instruments Methods Phys. Res. Sect. B Beam Interact. with Mater. Atoms*, 227, 4, 490, (2005).

[66] N. N. Nedialkov, S. E. Imamova, P. A. Atanasov, P. Berger, and F. Dausinger, *Appl. Surf. Sci.*, 247, 1, 243, (2005).

[67] P. Lorazo, L. J. Lewis, and M. Meunier, .

[68] N. Arnold, B. Luk'yanchuk, and N. Bityurin, *Appl. Surf. Sci.*, 127, 184, (1998).

[69] J. G. Lunney and R. Jordan, *Appl. Surf. Sci.*, 127, 941, (1998).

[70] X. Wang, Z. H. Shen, J. Lu, and X. W. Ni, *J. Appl. Phys.*, 108, 3, 33103, (2010).

[71] K. L. Choo, Y. Ogawa, G. Kanbargi, V. Otra, L. M. Raff, and R. Komanduri, *Mater. Sci. Eng. A*, 372, 1, 145, (2004).

[72] A. A. Ionin *et al.*, *J. Exp. Theor. Phys.*, 116, 3, 347, (2013).

[73] A. Borowiec, M. MacKenzie, G. C. Weatherly, and H. K. Haugen, *Appl. Phys. A Mater. Sci. Process.*, 76, 2, 201, (2003).

[74] J. Ren, M. Kelly, and L. Hesselink, *Opt. Lett.*, 30, 13, 1740, (2005).

[75] J. Bonse, K.-W. Brzezinka, and A. . Meixner, *Appl. Surf. Sci.*, 221, 1, 215, (2004).

[76] B. E. A. Saleh and M. C. Teich, "Baeam Optics," in *Fundamental of Photonics*, 2007, 74.

[77] Y. Kawamura, Y. Itagaki, K. Toyoda, and S. Namba, *Opt. Commun.*, 48, 1, 44, (1983).

[78] HOLO OR, "Beam Shaper: Polychromatic & Diffractive Beam Shaper." [Online]. Available: http://www.holoor.com/Diffractive_optics_Applications/Application_Notes_BeamShapers.htm. [Accessed: 19-Dec-2016].

[79] M. Pasienski and B. DeMarco, *Opt. Express*, 16, 3, 2176, (2008).

[80] J. E. Curtis, B. A. Koss, and D. G. Grier, "Dynamic holographic optical tweezers," (2002).

[81] J. S. Liu and M. R. Taghizadeh, *Opt. Lett.*, 27, 16, 1463, (2002).

[82] V. Boyer *et al.*, *Phys. Rev. A*, 73, 3, 31402, (2006).

[83] N. Sanner, N. Huot, E. Audouard, C. Larat, and J.-P. Huignard, *Opt. Lasers Eng.*, 45, 6, 737, (2007).

[84] H.-Y. Kim and S.-H. Cho, in *2015 11th Conference on Lasers and Electro-Optics Pacific Rim (CLEO-PR)*, 2015, 1.

[85] S. Hermann, T. Dezhdar, N.-P. Harder, R. Brendel, M. Seibt, and S. Stroj, *J. Appl. Phys.*, 108, 11, 114514, (2010).

[86] B. E. A. Saleh and M. C. Teich, "Polarization of Light," in *Fundamentals of Photonics*, 2007, 199.

[87] "Encyclopedia of Laser Physics and Technology - Brewster plates." [Online]. Available: https://www.rp-photonics.com/brewster_plates.html.

[88] Thorlabs, “Broadband Polarizing Beamsplitter Cubes.” [Online]. Available: https://www.thorlabs.de/newgrouppage9.cfm?objectgroup_id=739.

[89] Pp-photonics, “Waveplates, quarter-wave, half-wave plate, retarder plates, birefringence, zero-order, multiple-order,” *Encyclopedia of Laser Physics and Technology*, 2016. [Online]. Available: https://www.rp-photonics.com/waveplates.html.

[90] X. Ji *et al.*, *Appl. Opt.*, 53, 29, 6742, (2014).

[91] M. Birnbaum, *J. Appl. Phys.*, 36, 11, 3688, (1965).

[92] G. N. Maracas, G. L. Harris, C. A. Lee, and R. A. McFarlane, *Appl. Phys. Lett.*, 33, 5, 453, (1978).

[93] N. R. Isenor, *Appl. Phys. Lett.*, 31, 3, 148, (1977).

[94] H. M. van Driel, J. E. Sipe, and J. F. Young, *Phys. Rev. Lett.*, 49, 26, 1955, (1982).

[95] J. Sipe, J. Young, J. Preston, and H. van Driel, *Phys. Rev. B*, 27, 2, 1141, (1983).

[96] J. Young, J. Preston, H. van Driel, and J. Sipe, *Phys. Rev. B*, 27, 2, 1155, (1983).

[97] M. Huang, F. Zhao, Y. Cheng, N. Xu, and Z. Xu, *ACS Nano*, 3, 12, 4062, (2009).

[98] A. Borowiec and H. K. Haugen, *Appl. Phys. Lett.*, 82, 25, 4462, (2003).

[99] J. Bonse, J. Krüger, S. Höhm, and A. Rosenfeld, *J. Laser Appl.*, 24, 4, 42006, (2012).

[100] R. Le Harzic, F. Stracke, and H. Zimmermann, *J. Appl. Phys.*, 113, 18, 183503, (2013).

[101] T. Y. Hwang and C. Guo, *J. Appl. Phys.*, 108, 7, 73523, (2010).

[102] J. Bonse and J. Krüger, *J. Appl. Phys.*, 108, 3, (2010).

[103] J. Bonse, M. Munz, and H. Sturm, *J. Appl. Phys.*, 97, 1, 13538, (2005).

[104] P. Liu, L. Jiang, J. Hu, W. Han, and Y. Lu, *Opt. Lett.*, 38, 11, 1969, (2013).

[105] M. Yang *et al.*, *Opt. Lett.*, 39, 2, 343, (2014).

[106] W. Han, L. Jiang, X. Li, Q. Wang, H. Li, and Y. Lu, *Opt. Express*, 22, 13, 15820, (2014).

[107] M. Barberoglou, D. Gray, E. Magoulakis, C. Fotakis, P. A. Loukakos, and E. Stratakis, *Opt. Express*, 21, 15, 18501, (2013).

[108] G. F. B. Almeida, R. J. Martins, A. J. G. Otuka, J. P. Siqueira, and C. R. Mendonca, *Opt. Express*, 23, 21, 27597, (2015).

[109] R. D. Murphy, B. Torralva, D. P. Adams, and S. M. Yalisove, *Appl. Phys. Lett.*, 104, 23, 231117, (2014).

[110] X. Sedao *et al.*, *Appl. Phys. Lett.*, 104, 17, 171605, (2014).

[111] L. Jiang, W. Han, X. Li, Q. Wang, F. Meng, and Y. Lu, *Opt. Lett.*, 39, 11, 3114, (2014).

[112] E. Rebollar, J. R. Vázquez de Aldana, J. A. Pérez-Hernández, T. A. Ezquerra, P. Moreno, and M. Castillejo, *Appl. Phys. Lett.*, 100, 4, 41106, (2012).

[113] G. Deng, G. Feng, K. Liu, and S. Zhou, *Appl. Opt.*, 53, 14, 3004, (2014).

[114] B. Kumar *et al.*, *J. Phys. D. Appl. Phys.*, 41, 15, 155303, (2008).

[115] S. Höhm, A. Rosenfeld, J. Krüger, and J. Bonse, *J. Appl. Phys.*, 112, 1, 14901, (2012).

[116] SPI Lasers UK Ltd, "G4 Pulsed Fibre Laser Product Manual- Installation Guide and User Manual,SM-S00245 Rev E." 2012.

[117] Amplitude Systemes, "Satsuma user manual REf 246-A." 2013.

[118] Thorlabs, "NB1-K13 Nd:YAG Mirror, 532 nm and 1064 nm," 2016. [Online]. Available: https://www.thorlabs.de/thorproduct.cfm?partnumber=NB1-K13.

[119] Semrock, "Single-edge laser-flat dichroic beamsplitter," 2016. [Online]. Available: https://www.semrock.com/FilterDetails.aspx?id=Di02-R1064-25x36.

[120] Newson, "Elevathor smart axial lens shifter," 2016. [Online]. Available: http://www.newson.be/elevathor.htm.

[121] Newson, "Smart deflector data sheet," 2016. [Online]. Available: http://www.newson.be/rhothor_SmartDeflector.htm.

[122] QIOPTIQ Photonics GmbH & Co.KG, "Laser Material Processing." .

[123] Aerotech, "PRO165LM Series Stage User's Manual (Revision 1.06.00)." 2010.

[124] Aerotech, (2010).

[125] Aerotech, (2010).

[126] Aerotech, (2015).

[127] Coherent, "Super rapid He Datasheet." 2013.

[128] Aerotech, "PRO165LM Series Linear Stages | Aerotech, Inc." [Online]. Available: https://www.aerotech.co.uk/product-catalog/stages/linear-stage/pro165lm.aspx.

[129] SPI, "redPOWER R4 HS Series." 2016.

[130] Scanlab, "intelliSCAN datasheet." 2016.

[131] Thorlabs, "Mounted Zero-Order Quarter-Wave Plates," 2016. [Online]. Available: https://www.thorlabs.com/newgrouppage9.cfm?objectgroup_id=7234&pn=WPQ10M-1030#4267.

[132] Thorlabs, "Mounted Zero-Order Half-Wave Plates," 2016. [Online]. Available: https://www.thorlabs.com/newgrouppage9.cfm?objectgroup_id=711&pn=WPH10M-1030#4268.

[133] Thorlabs, "Manual Rotation Mounts, High Precision," 2016. [Online]. Available: https://www.thorlabs.com/newgrouppage9.cfm?objectgroup_id=990&pn=PRM1/M#2476.

[134] RP Photonics, "Polarizers, absorptive, polarizing beam splitters, birefringence, calcite, Glan-Taylor prism, Wollaston prism, thin-film polarizers," *Encyclopedia of Laser Physics and Technology*, 2016. [Online]. Available: https://www.rp-photonics.com/polarizers.html.

[135] Thorlabs, “Broadband Polarizing Beamsplitter Cubes in 30 mm Cage Cubes,” 2016. [Online]. Available: https://www.thorlabs.com/newgrouppage9.cfm?objectgroup_id=4137.

[136] Thorlabs, “Beam Blocks and Traps,” 2016. [Online]. Available: https://www.thorlabs.com/newgrouppage9.cfm?objectgroup_id=1449.

[137] gentec, “UP19-W Power detectors,” 2016. [Online]. Available: https://www.gentec-eo.com/products/power-detectors/UP19-W.

[138] gentec, “Uno data sheet.” 2016.

[139] Ophir Photonics Group, “The Truth about Laser Beam Profilers: Camera vs. Scanning Slit,” 2016. [Online]. Available: http://www.ophiropt.com/blog/laser-measurement/the-truth-about-laser-beam-profilers-camera-vs-scanning-slit/.

[140] DataRay Inc., “Beam’R2 - XY Scanning Slit Beam Profiler,” 2016. [Online]. Available: http://www.dataray.com/beamr2-xy-scanning-slit-beam-profiler.html.

[141] Alicona, “That’s metrology: Focus-Variation in Modern Manufacturing,” 2016. [Online]. Available: http://www.alicona.com/news-downloads/detail/focus-variation-in-modern-manufacturing/.

[142] Alicona, “Alicona Focus Variation magazine: Form and roughness in one system.” 2015.

[143] Bruker, “Contour GT datasheet.” .

[144] K. Watanabe and T. Iguchi, *Appl. Phys. A Mater. Sci. Process.*, 69, 7, S845, (1999).

[145] C. L. Liu *et al.*, *Mater. Sci. Eng. B*, 47, 1, 70, (1997).

[146] H. R. Shanks, P. D. Maycock, P. H. Sidles, and G. C. Danielson, *Phys. Rev.*, 130, 5, 1743, (1963).

[147] G. E. Jellison and D. H. Lowndes, *Appl. Phys. Lett.*, 41, 7, 594, (1982).

[148] J. M. Liu, *Opt. Lett.*, 7, 5, 196, (1982).

[149] D. Autrique, I. Gornushkin, V. Alexiades, Z. Chen, A. Bogaerts, and B. Rethfeld, *Appl. Phys. Lett.*, 103, 17, 174102, (2013).

[150] G. Galasso, M. Kaltenbacher, A. Tomaselli, and D. Scarpa, *J. Appl. Phys.*, 117, 12, 123101, (2015).

[151] J. H. Yoo, S. H. Jeong, R. Greif, and R. E. Russo, *J. Appl. Phys.*, 88, 3, 1638, (2000).

[152] J. Bonse, S. Baudach, J. Krüger, W. Kautek, and M. Lenzner, 25, 19, (2002).

[153] A. Y. Vorobyev and C. Guo, *Opt. Express*, 19, S5, A1031, (2011).

[154] M. Auslender, D. Levy, and S. Hava, *Appl. Opt.*, 37, 2, 369, (1998).

[155] A. A. Abouelsaood, S. A. El-Naggar, and M. Y. Ghannam, *Prog. Photovoltaics Res. Appl.*, 10, 8, 513, (2002).

[156] BYU Photonics, “Polarization and Polarimetric Testing.” [Online]. Available: http://www.photonics.byu.edu/polarization.phtml.